

See discussions, stats, and author profiles for this publication at: <https://www.researchgate.net/publication/263056563>

# Titanium Dioxide Nanomaterials for Sensor Applications

ARTICLE *in* CHEMICAL REVIEWS · JUNE 2014

Impact Factor: 46.57 · DOI: 10.1021/cr400625j · Source: PubMed

---

CITATIONS

38

---

READS

63

2 AUTHORS, INCLUDING:



Jing Bai

Shanghai Jiao Tong University

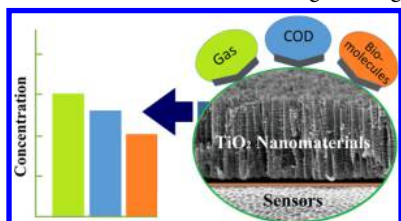
31 PUBLICATIONS 631 CITATIONS

SEE PROFILE

## Titanium Dioxide Nanomaterials for Sensor Applications

Jing Bai and Baoxue Zhou\*

School of Environmental Science and Engineering, Shanghai Jiao Tong University, Shanghai 200240, People's Republic of China



## CONTENTS

1. Introduction	10131
1.1. Sensing Properties of Titanium Oxide	10132
1.2. Sensing Electrode of TiO <sub>2</sub> Nanomaterials	10134
1.2.1. Synthesis of TiO <sub>2</sub> Nanomaterials	10134
1.2.2. TiO <sub>2</sub> Electrode	10135
1.3. Sensing Processes	10135
2. Typical TiO <sub>2</sub> Sensors	10136
2.1. Gas Sensor	10136
2.2. COD Sensor	10137
2.3. Biosensor	10137
3. Sensor Applications	10138
3.1. Gas Sensor	10138
3.1.1. Measurement Principle	10138
3.1.2. Hydrogen (H <sub>2</sub> ) Sensor	10138
3.1.3. Oxygen (O <sub>2</sub> ) Sensor	10142
3.1.4. Humidity (H <sub>2</sub> O) Sensor	10144
3.1.5. Carbon Monoxide (CO) Sensor	10145
3.1.6. Volatile Organic Compounds (VOCs) Sensor	10148
3.1.7. Sensor for Other Gases	10149
3.1.8. Brief Summary	10150
3.2. COD Sensor	10151
3.2.1. Measurement Principle	10151
3.2.2. TiO <sub>2</sub> -Based Photocatalytic COD Sensor	10153
3.2.3. Photoelectrocatalytic-Based TiO <sub>2</sub> COD Sensor	10153
3.2.4. Online TiO <sub>2</sub> COD Sensor	10154
3.2.5. Brief Summary	10156
3.3. Biosensor	10156
3.3.1. Measurement Principle	10156
3.3.2. Amperometric TiO <sub>2</sub> Biosensor	10158
3.3.3. TiO <sub>2</sub> Potentiometric Biosensor	10164
3.3.4. TiO <sub>2</sub> Optical Biosensor	10164
3.3.5. Other TiO <sub>2</sub> Biosensor	10168
3.3.6. Brief Summary	10168
4. Summary and Future Prospects	10169
Author Information	10169
Corresponding Author	10169
Notes	10169
Biographies	10169
Acknowledgments	10170
References	10170

## 1. INTRODUCTION

Sensors have currently become increasingly important in a world where technological advances demand precise information of numerous categories.<sup>1,2</sup> They have been widely applied in fields such as industrial manufacturing, aerospace, ocean exploring, environmental protection, resources investigation, medical diagnosis, and bioengineering.<sup>3–6</sup>

Sensors can be made from various materials depending on the purposes they serve. High sensitivity, fast response, and good selectivity are the general requirements for a good sensor. For large-scale application, low material cost and easy fabrication are also required. With dramatic advances in nanotechnology, great progress has been made in recent years thanks to the newly developed nanomaterials for sensor application.<sup>7–12</sup> Because of the inherent properties of nanomaterials, for example, super small size, and large surface–volume ratio, they can remarkably improve the sensitivity of the sensors as compared to traditional materials. By judiciously decorating the nanoparticle surface composition, unique target binding characters can be achieved to great selectivity. Furthermore, the robustness of nano semiconductor made it highly sustainable in various detection environments.

As one type of semiconductor, TiO<sub>2</sub> has received wide attention ever since 1972 when Fujishima and Honda<sup>13–15</sup> discovered photocatalytic splitting of water on a TiO<sub>2</sub> electrode under ultraviolet (UV) light. Over the past decades, TiO<sub>2</sub> has found applications in many promising areas ranging from photovoltaics, photocatalysis, to sensors.<sup>16–19</sup> Besides the aforementioned inherent advantages of nanomaterials, nano TiO<sub>2</sub> materials are also nontoxic, biocompatible, photo-corrosion free, and cost-effective.<sup>20</sup> In addition, the availability of a variety of nanostructures enables them to achieve extraordinary large surface area, as well as unique chemical, physical, and electronic properties.<sup>21–23</sup> TiO<sub>2</sub> nanomaterials can be prepared in large-scale at mild temperatures and condition, which facilitates low-cost fabrication. Therefore, tremendous interest has been shown in studies of TiO<sub>2</sub> nanomaterial structures, their transduction principle, and system simulation functions for sensor applications.

Recently, many novel TiO<sub>2</sub> nanomaterials with new composition and structure have been used for various sensors. On the basis of different sensing targets or measurement principle, the sensors can be referred to as gas sensor, optical sensor, electric sensor, environmental sensor, biosensor, etc. In this Article, three typical sensors will be reviewed: (1) TiO<sub>2</sub>-based gas sensor for detecting gas or volatile chemicals; (2) TiO<sub>2</sub>-based chemical oxygen demand (COD) sensor for

**Special Issue:** 2014 Titanium Dioxide Nanomaterials

**Received:** November 3, 2013

**Published:** June 12, 2014

detecting soluble organics in water environment; and (3)  $\text{TiO}_2$ -based biosensor for detecting biological substance, which were categorized according to the target substance on sensors, science these sensors showed, superior sensing performance, and good applied prospect. Other key developments about detecting mechanisms, material selection, and sensing performances will also be reviewed.

### 1.1. Sensing Properties of Titanium Oxide

$\text{TiO}_2$  belongs to the family of transition metal oxides. There are mainly three kinds of phase structure found in nature, commonly known as anatase (tetragonal), brookite (orthorhombic), and rutile (tetragonal),<sup>24</sup> whose bandgaps are 3.2, 3.02, and 2.96 eV, respectively.<sup>25</sup> Anatase and rutile have wider application because they are more stable than brookite. Rutile  $\text{TiO}_2$  has a tetragonal structure and contains 6 atoms per unit cell (Figure 1) in which the  $\text{TiO}_6$  octahedron is slightly

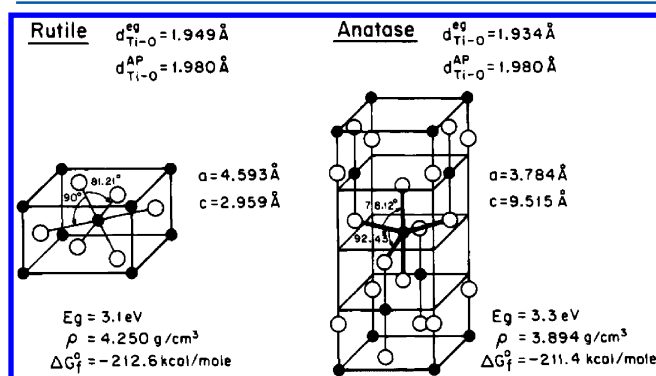


**Figure 1.** Structures of rutile and anatase  $\text{TiO}_2$ . Reprinted with permission from ref 24. Copyright 1995 American Chemical Society.

distorted.<sup>21,26,27</sup> Anatase  $\text{TiO}_2$  also has a tetragonal structure, but the distortion of the  $\text{TiO}_6$  octahedron is slightly larger for anatase.<sup>28,29</sup> Rutile is usually more stable than anatase at most temperatures and pressures.<sup>30</sup> Although single-crystal anatase and rutile can be directly prepared using a hydrothermal method, in many cases, the as-prepared  $\text{TiO}_2$  appears to be amorphous, and heat treatment has a vital role in the phase transformation; for example, by increasing the annealing temperature to 300–500 °C, amorphous structure can be changed into anatase, and when the temperature rises to 600–700 °C, anatase can be further transformed into rutile.<sup>31</sup>

The inherent oxygen vacancy in  $\text{TiO}_2$  crystal indicates that there is more plus charge from Ti as compared to minus charge from oxygen. As confirmed from the stoichiometry theory for semiconductor,<sup>32</sup> this kind of crystal is electron rich and belongs to n-type semiconductor. When gas absorbs onto the  $\text{TiO}_2$  surface, it could release electrons into  $\text{TiO}_2$ , leading to the increase or decrease of resistance of  $\text{TiO}_2$  materials, the typical sensing mechanism of  $\text{TiO}_2$ -based gas sensor. Furthermore, the conductivity property can be modified by doping other elements (especially metal elements) into  $\text{TiO}_2$  materials. By controlling the doping pattern, such as doping dosage and heating temperature, the n-type  $\text{TiO}_2$  materials can be transformed to p-type.<sup>33</sup> Different from n-type, the resistance of p-type  $\text{TiO}_2$  will increase when contacting gases.

On the other hand,  $\text{TiO}_2$  is an excellent photocatalyst for two structural properties: first, the valence band of  $\text{TiO}_2$  is quite deep; second, the photon generated holes tend to locate on the surface of materials, which makes it easy to be harvested by free electrons from outside, that is, working as an oxidant agent. Anatase structure is preferred over other polymorphs for photocatalysis thanks to its higher electron mobility, low dielectric constant, and low density.<sup>34</sup> Its increased photo-

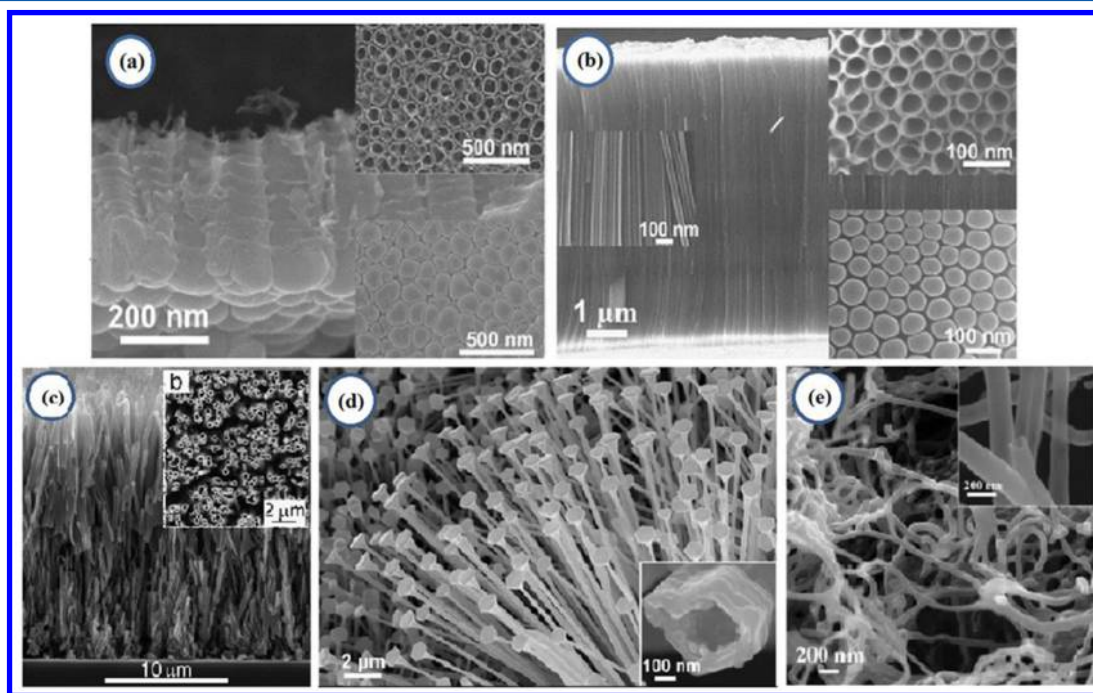


**Figure 2.**  $\text{TiO}_2$  tubular nanostructures: (a) Short  $\text{TiO}_2$  nanotube arrays from anodization of Ti. (b) Long  $\text{TiO}_2$  nanotube arrays from anodization of Ti. Reprinted with permission from ref 62. Copyright 2007 Elsevier. (c)  $\text{TiO}_2$  nanotubes from a ZnO template (LPD process). Reprinted with permission from ref 89. Copyright 2012 American Chemical Society. (d)  $\text{TiO}_2$  nanotubes from a ZnO template ( $\text{TiCl}_4$  vapor pulses). Reprinted with permission from ref 91. Copyright 2014 American Chemical Society. (e) Fibrous  $\text{TiO}_2$  nanotube network from a cellulose nanofiber template (ALD process). Reprinted with permission from ref 92. Copyright 2014 Wiley-VCH.



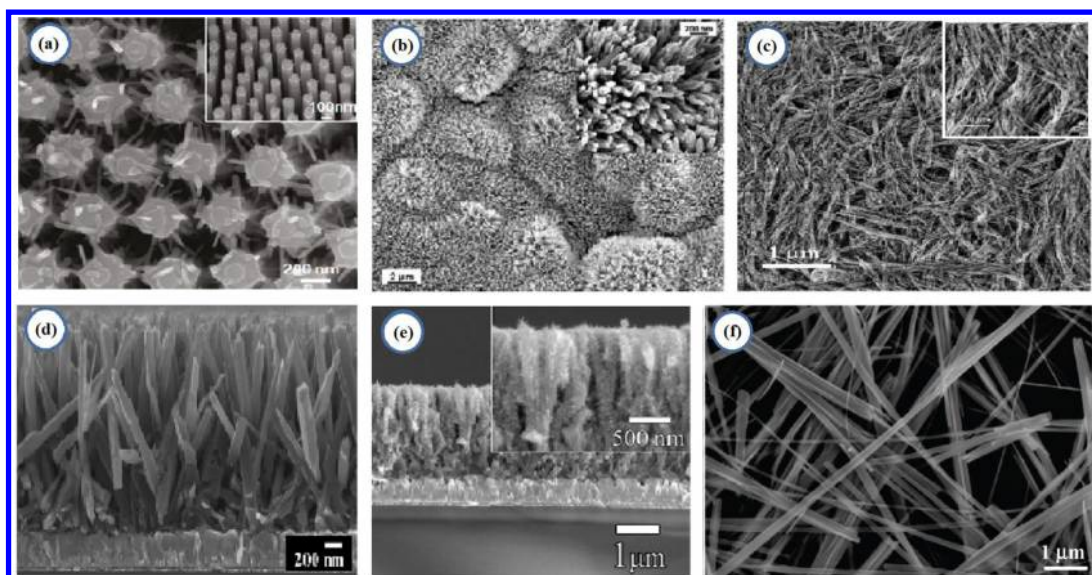


**Figure 3.** (a)  $\text{TiO}_2$  nanobelts. Reprinted with permission from ref 93. Copyright 2011 American Chemical Society. (b)  $\text{TiO}_2$  nanorods. Reprinted with permission from ref 55. Copyright 2004 RSC. (c)  $\text{TiO}_2$  nanowires. Reprinted with permission from ref 83. Copyright 2010 American Chemical Society. (d)  $\text{TiO}_2$  nanorods. Reprinted with permission from ref 84. Copyright 2009 American Chemical Society. (e) Branched  $\text{TiO}_2$  nanorods. Reprinted with permission from ref 85. Copyright 2011 American Chemical Society. (f) Hierarchical  $\text{TiO}_2$  Nanowires. Reprinted with permission from ref 86. Copyright 2010 American Chemical Society.

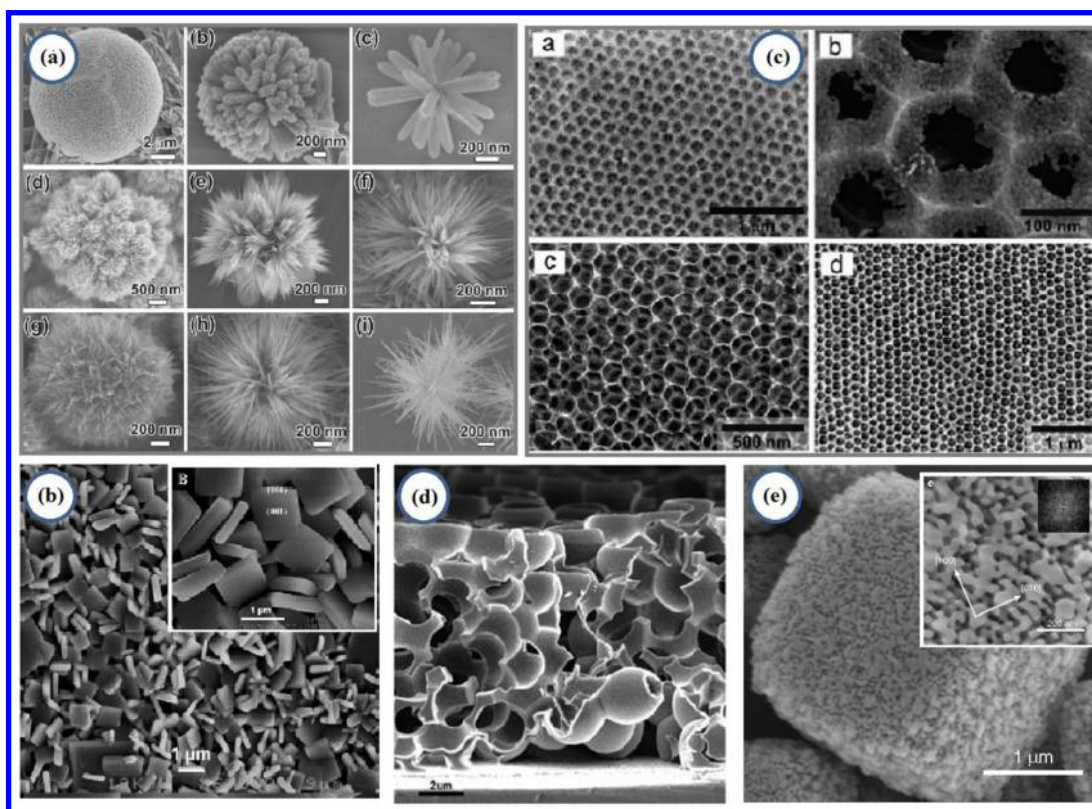


**Figure 4.** (a) 3D dendritic  $\text{TiO}_2$  nanostructures. Reprinted with permission from ref 87. Copyright 2011 American Chemical Society. (b)  $\text{TiO}_2$  nanosheets. Reprinted with permission from ref 88. Copyright 2009 American Chemical Society. (c)  $\text{TiO}_2$  opal. Reprinted with permission from ref 98. Copyright 2007 American Chemical Society. (d) 3D  $\text{TiO}_2$  opal. Reprinted with permission from ref 103. Copyright 2011 American Chemical Society. (e) Mesoporous  $\text{TiO}_2$  single crystals. Reprinted with permission from ref 104. Copyright 2013 American Chemical Society.

activity is facilitated by the slightly higher Fermi level, lower capacity to adsorb oxygen, and higher degree of hydroxylation in the anatase phase. Anatase  $\text{TiO}_2$  is considered to be photocatalytically active in light of its charge carrier dynamics, chemical properties, and the activity of photocatalytic

degradation of organic compounds. It has inherent surface band bending that forms spontaneously in a deep region with a steep potential.<sup>35</sup> Thus, its surface hole trapping dominates because spatial charge separation is achieved by the photo-generated holes transfer toward the surface of the particle via

the strong upward band bending. However, in the rutile phase, the bulk recombination of electrons and holes inevitably occurs, and only the holes close to the surface are trapped and transferred to the surface. These advantages make anatase phase the most competitive candidate for COD sensor because of its good electron transfer capability and chemical stability. Furthermore, the photovoltaic property of  $\text{TiO}_2$  under UV illumination makes the sensors self-clean the contamination, resulting in a long life span.

$\text{TiO}_2$  nanomaterials are basically biocompatible and environmentally friendly and have been frequently proposed as a prospective interface for the immobilization of biomolecules,<sup>36,37</sup> which is another important aspect for  $\text{TiO}_2$  materials. Moreover, titanium forms coordination bonds with the amine and carboxyl groups of enzymes and maintains the enzyme's biocatalytic activity.<sup>38,39</sup> In addition, due to the electron-accepting character of  $\text{TiO}_2$  as discussed above, the electrons produced by the reaction between biomolecules and analyte can be harvested by  $\text{TiO}_2$ . The injected electrons can be transferred to the outer circuit, which can be used to detect the reaction. With all aforementioned merits,  $\text{TiO}_2$  is one of the most competitive candidates for biosensor.

Because a particular sensing purpose can only be achieved with a specific  $\text{TiO}_2$  property, the types of  $\text{TiO}_2$  phase, composition, and nanostructural feature are decisive factors for sensor performance.

## 1.2. Sensing Electrode of $\text{TiO}_2$ Nanomaterials

**1.2.1. Synthesis of  $\text{TiO}_2$  Nanomaterials.**  $\text{TiO}_2$  nanomaterials could be prepared by various methods including sol-gel,<sup>40–42</sup> electrodeposition,<sup>43–45</sup> micelle and inverse micelle,<sup>46–48</sup> chemical vapor deposition,<sup>49–51</sup> physical vapor deposition,<sup>52–54</sup> direct oxidation,<sup>55–79</sup> hydrothermal,<sup>80–88</sup> and combined methods.<sup>89–104</sup> The crystal structures of the  $\text{TiO}_2$  materials prepared by these methods are usually rutile or anatase, and sometimes show amorphous state. Certain temperature and pressure are required to create the specific phase structures. On the other hand, the geometry of  $\text{TiO}_2$  nanomaterials could be greatly varied from nanosphere to one-dimensional (1D), or even three-dimensional (3D) nanostructures. It is commonly recognized that nanostructured  $\text{TiO}_2$  is more favorable for sensor applications due to their advantages of larger surface area and better electron transition. Figures 2–4 show some newly developed  $\text{TiO}_2$ -based nanostructure in recent years.

In the past decade,  $\text{TiO}_2$  nanotube arrays (NTs) obtained from electrochemical oxidation reaction of a metallic titanium substrate are the most popular nanostructure. In view of the history of  $\text{TiO}_2$  NTs, Grimes' group<sup>56–60</sup> and Schmuki's group<sup>61–66</sup> have made a great contribution to the development of new synthesis methods and their potential applications. In a typical process,  $\text{TiO}_2$  NTs can be prepared by anodization of titanium foil in the F-containing electrolyte at a constant anodization potential. Figure 2a,b shows two typical  $\text{TiO}_2$  NTs fabricated from acidic fluoride electrolytes and glycerol/fluoride electrolytes, respectively.<sup>52</sup> The geometry of  $\text{TiO}_2$  NTs could be varied according to the anodization voltage, duration, and electrolyte composition. So far, derived  $\text{TiO}_2$  NTs with the specific features such as "tube stacks",<sup>67</sup> "bamboo",<sup>68,69</sup> "double-walled tubes",<sup>70</sup> and "amphiphilic double-layer tubes"<sup>71</sup> have been developed. Various technical alloys can also be anodized to fabricate nanotube layers using the same approach as for Ti. Schmuki's group has demonstrated the

result by using binary alloys such as  $\text{TiAl}$ ,<sup>72,73</sup>  $\text{TiNb}$ ,<sup>74</sup>  $\text{TiZr}$ ,<sup>75,76</sup> or complex biomedical alloys such as  $\text{Ti}_6\text{Al}_7\text{Nb}$ <sup>90</sup> and  $\text{Ti}_{29}\text{Nb}_{13}\text{Ta}_{4.6}\text{Zr}$ .<sup>91,92</sup> The obtained NTs are quite similar to those from Ti foil, showing highly ordered and vertical structure.

In another scheme,  $\text{TiO}_2$  tubular nanostructures can be prepared from a template such as ZnO nanowires (NWs). To realize the conversion of ZnO to  $\text{TiO}_2$ , several different strategies have been developed. As shown in Figure 2c,  $\text{TiO}_2$  nanotubes can be prepared using a liquid-phase deposition (LPD) method,<sup>89</sup> which was conducted by placing ZnO NWs substrates in a solution of  $(\text{NH}_4)_2\text{TiF}_6$  and  $\text{H}_3\text{BO}_3$  for tens of minutes.  $\text{TiO}_2$  nanotubes can also be obtained by using a sol-gel process in which ZnO NWs template is coated by  $\text{TiO}_2$  sol, followed by a selective removal of ZnO in HF aqueous solution.<sup>90</sup> Another method for the conversion is to introduce  $\text{TiCl}_4$  vapor pulses to ZnO NWs where there is a cation exchange reaction between  $\text{TiCl}_4$  vapor and ZnO solid (see Figure 2d).<sup>91</sup> Besides ZnO NWs template, cellulose nanofiber has been used to fabricate a fibrous  $\text{TiO}_2$  nanotube network by applying an atomic layer deposition (ALD) process (see Figure 2f).<sup>92</sup>

Nanowires/nanorods (NWs/NRs) are also typical 1D nanostructure, which can be prepared by using various methods such as chemical vapor deposition (CVD), direct oxidation, and hydrothermal, etc. It is reported that the  $\text{TiO}_2$  NRs can be grown on the Si NWs array backbones through a surface-reaction-limited pulsed chemical vapor deposition (SPCVD) process.<sup>93</sup> As shown in Figure 3a, the resulted sample shows a 3D NWs network. This work also provides evidence that a very large quantity of uniform-sized  $\text{TiO}_2$  NRs can be grown on all possible surfaces despite the extremely narrow and deep spaces. Figure 3b shows the  $\text{TiO}_2$  NRs fabricated by thermal oxidation of Ti plate with acetone as oxygen source at 850 °C for 90 min.<sup>55</sup> The key to achieve the  $\text{TiO}_2$  NRs might be attributed to the diffusion of Ti cations to the oxide surface where there is a reaction with the adsorbed acetone species to form nanorods.

Hydrothermal method is very common in the preparation of various materials. Vertically aligned single-crystal  $\text{TiO}_2$  NWs grown directly on transparent conducting oxides (TCO) substrate can be obtained by a hydrothermal process as shown in Figure 3d.<sup>84</sup> On the basis of hydrothermal made  $\text{TiO}_2$  NRs, an additional hydrothermal growth of  $\text{TiO}_2$  can result in the branched  $\text{TiO}_2$  NRs (see Figure 3e).<sup>85</sup> The process starts with a further deposition of seed nanoparticles (NPs) on the NRs, followed by the second growth of new NRs. In addition, single-crystalline anatase  $\text{TiO}_2$  nanobelts can be prepared via an alkaline hydrothermal process by using commercial  $\text{TiO}_2$  powders, NaOH, HCl, and deionized water (see Figure 3f).<sup>86</sup>

In addition to the 1D nanostructure, researchers have developed many other types of  $\text{TiO}_2$  nanostructures. Figure 4a shows a serial of 3D  $\text{TiO}_2$  microspheres with nanorod building units (a–c), nanoribbon building units (d–f), and nanowire building units (g–i) fabricated from a hydrothermal method.<sup>87</sup> As reported, the geometry of  $\text{TiO}_2$  microspheres can be controlled by adding different chemicals into aqueous titanium(IV) tetra-isopropoxide (TTIP) solutions with a proper ratio. Another work involves the preparation of anatase  $\text{TiO}_2$  single-crystal nanosheets using a solvothermal method (see Figure 4b).<sup>88</sup> As compared to  $\text{TiO}_2$  nanoparticles (NPs) (Degussa P25) as a benchmarking material, the nanosheets having 64% large {001} facets show superior photoreactivity.



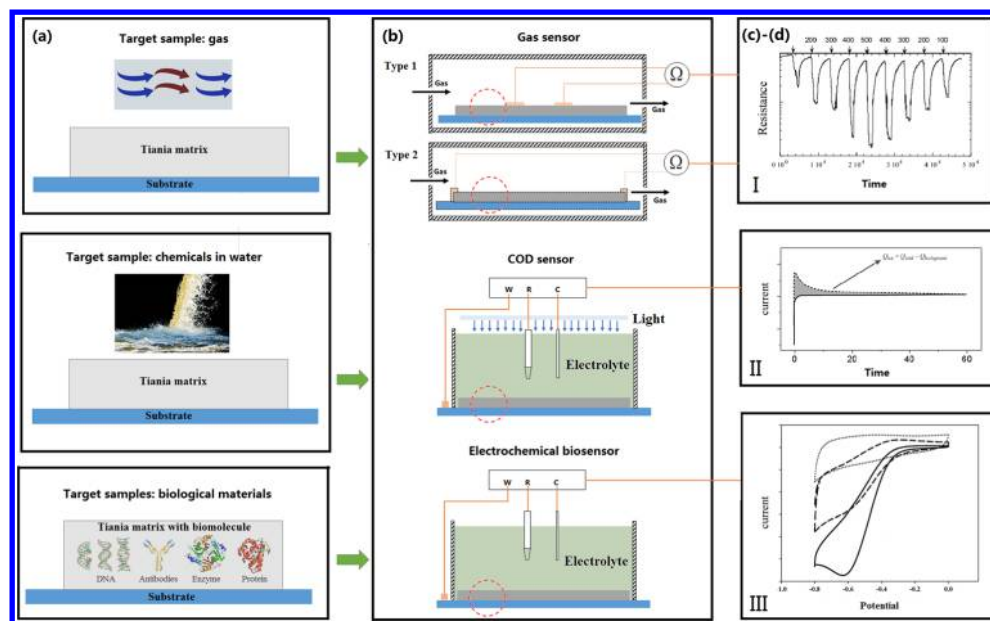


**Figure 5.** Elements and sensing processes of the typical  $\text{TiO}_2$ -based gas sensor, COD sensor, and biosensor. (a)-(b) Original drawing was done by us. (c)-(d) I. Reprinted with permission from ref 129. Copyright 2003 Elsevier. II. Reprinted with permission from ref 311. Copyright 2008 Wiley-VCH. III. Reprinted with permission from ref 373. Copyright 2008 Elsevier.

Ordered and periodic  $\text{TiO}_2$  inverse-opal structure is also a key concern because it favors photonic bandgaps (PBGs). To achieve  $\text{TiO}_2$  inverse-opal structures, it is currently primarily through sol-gel hydrolysis of metal alkoxide precursors such as TTIP or titanium (IV) *n*-butoxide<sup>95–99</sup> or atomic layer deposition (ALD)<sup>100–103</sup> using latex spheres as templates. In a typical process, latex spheres (polystyrene (PS), or  $\text{SiO}_2$ ) are first self-assembled on conductive support, and then their spaces are infiltrated by  $\text{TiO}_2$  materials. At last, a special treatment such as calcination for polystyrene beads, HF corrosion for  $\text{SiO}_2$  beads, or even ion-milling can produce  $\text{TiO}_2$  opal structures. On the basis of the layer numbers of spheres, single or multiple layered  $\text{TiO}_2$  opal structure could be achieved (see Figure 4c,d).<sup>99,103</sup>

Figure 4e shows a mesoporous single-crystal (MSC)  $\text{TiO}_2$  based on seeded nucleation and growth inside a mesoporous template immersed in a dilute reaction solution.<sup>104</sup> Briefly, the mesoporous silica template was seeded by immersion in aqueous  $\text{TiCl}_4$  at 70 °C for 60 min, and then as-made template was mixed with 1-methylimidazolium tetra-fluoroborate and titanium tetrafluoride aqueous solution in 50 mL of  $\text{TiF}_4$  solution following a Teflon-lined autoclave. Finally, the template is removed by selective etching in aqueous NaOH to recover the mesoporous  $\text{TiO}_2$ . The compact, anatase  $\text{TiO}_2$  crystal has a specific area of  $70 \text{ m}^2 \text{ g}^{-1}$  for 20 nm pores in  $2 \mu\text{m}^3$  crystals. It is evidenced that both isolated MSCs and ensembles incorporated into films have substantially higher conductivities and electron mobilities than that of nanocrystalline  $\text{TiO}_2$ .

**1.2.2.  $\text{TiO}_2$  Electrode.** To prepare  $\text{TiO}_2$  electrode for assembling a sensor, two or more steps are typically needed.  $\text{TiO}_2$  nanomaterials are first synthesized through previously mentioned methods and then assembled into a sensing electrode. The substrate types of electrode can be of TCO glass, alumina, metal, Si wafer, plastic, etc. The necessity of substrate conductivity depends on the measurement principle, but nonconductive substrate is not commonly used except in some gas sensors.<sup>105,106</sup> In most cases,  $\text{TiO}_2$  electrode could be directly fabricated by aforementioned facile methods, such as

anodization, hydrothermal, and physical/chemical vapor deposition.

In general, the as-prepared pure  $\text{TiO}_2$  nanomaterials electrode cannot meet the sensing requirements, for example, in sensitivity, detection range, response time, and operational temperature, especially for biosensing purpose. Therefore,  $\text{TiO}_2$  film modification, for example, with the introduction of other elements like noble metal, polymer, and biomolecule, is applied in most studies. For instance, pure  $\text{TiO}_2$  nanomaterials electrode can be modified with palladium nanoparticles to improve the sensing performance in a  $\text{H}_2$  sensor,<sup>107</sup> while in a biosensor, biomolecules such as DNA, antibodies, enzyme, or protein are usually indispensable parts.<sup>108–111</sup>

$\text{TiO}_2$  nanomaterial-based electrodes are the key units for sensors. Better sensing performance calls for optimization of  $\text{TiO}_2$  lattice structures and electrode preparations.

### 1.3. Sensing Processes

Figure 5 shows three typical  $\text{TiO}_2$ -based sensors for different applications, that is, gas sensor, COD sensor, and biosensor. The working principles could be quite different for sensors of different types and purposes. However, most of the sensing processes are similar and could be simplified into four steps: (a) receptors specifically binding to analyte; (b) a specific chemical or biochemical reaction taking place on interface and giving rise to a signal received by transducer; (c) signal being converted to electronic signal and amplified by detector circuit using appropriate reference; and (d) signal being sent to computers for data processing and resulting quantity presented through an interface to operator. To create an operation-friendly interface for different markets, some basic requirements are necessary:

- (1) The sensor must be highly specific to the intended target, stable under normal conditions, and comparable in performance between assays.
- (2) Impacts from physical parameters like stirring, pH, and temperature should be minimized, and minimal pretreatments are required.

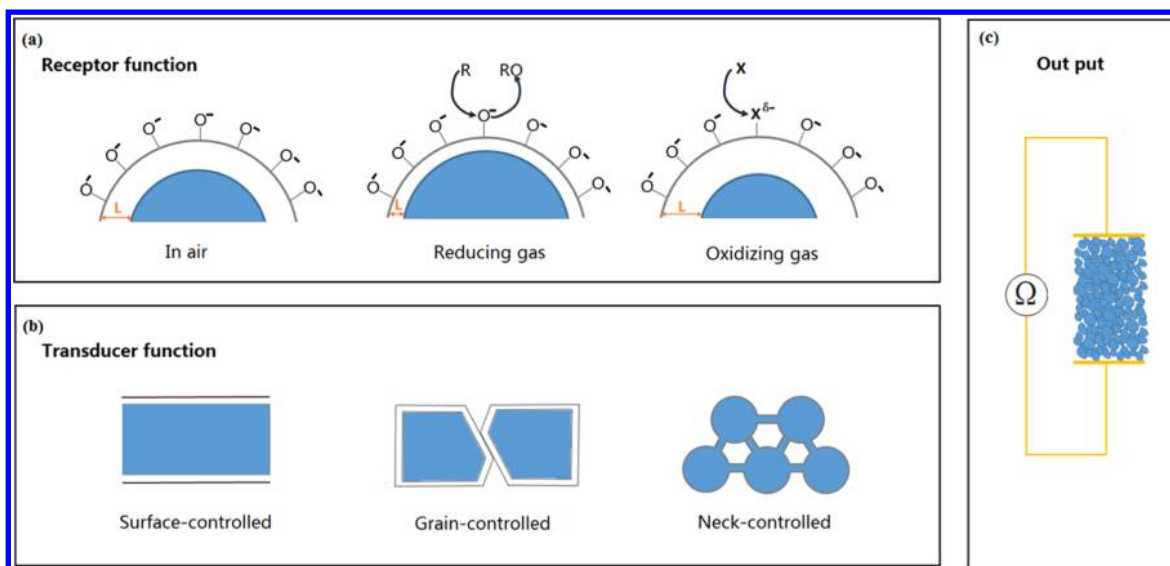


Figure 6. Schematic view of gas sensing at different mode. Original drawing was done by us.

- (3) The response should be accurate, reproducible, and linear over the concentration range of interest, without diluting or concentrating. It should also be free from electrical or other transducer-induced noises.
- (4) It is always desirable to provide real-time analysis.
- (5) It should be inexpensive, compact, portable, and user-friendly.

Therefore,  $\text{TiO}_2$  nanomaterial synthesis, sensor assembly, and operational methods are important and certainly attract researchers' interest.

## 2. TYPICAL $\text{TiO}_2$ SENSORS

$\text{TiO}_2$ -based sensors can be categorized from various perspectives. However, in view of recent research interest, we will mainly review gas sensors, COD sensors, and biosensors. This section mainly discusses the sensor applications and their sensing mechanisms.

### 2.1. Gas Sensor

A gas sensor is a device that detects the presence of various gases, including combustible, flammable, and toxic gases. A gas sensor is important because many gases are harmful to organic life. In all kinds of semiconductor sensors,  $\text{TiO}_2$  sensor is favored thanks to its high sensitivity, fast response, low cost, and long-term stability.

$\text{TiO}_2$  gas sensor can detect different gases including oxidative gas ( $\text{O}_2$ ,  $\text{NO}_2$ ) and reductive gas ( $\text{H}_2$ ,  $\text{CO}$ ,  $\text{NH}_3$ ,  $\text{H}_2\text{S}$ , VOCs), representing a resistance increase and decrease, respectively. Normally, the microscopic reactions between these gases and  $\text{TiO}_2$  surface are much different, the sensing mechanism is more complicated, and the sensor performance could be affected by many factors. However, the sensing mechanism can be recognized by the following two processes: receptor process and transducer process (see Figure 6).

The receptor process involves physisorption and chemisorption processes, which occur at  $\text{TiO}_2$  surface. First, a gas molecule is absorbed on  $\text{TiO}_2$  surface through physisorption, which was determined by van der Waals and dipole interactions; second, the gas molecule is further absorbed by chemisorption via a strong chemical bond formed between the gas and the surface atoms of  $\text{TiO}_2$ . During the process, the temperature tends to influence the physisorption in that the

increasing temperature leads to the decrease of physisorption. On the other hand, chemical bonding could influence the chemisorption for the activation energy may influence the rate of chemisorption process. Therefore, the receptor process is determined by the physisorption and chemisorption capability together.

The transducer process involves the transportation of electrons in the semiconductor materials and transformation of electrons to outer signals. This process is also affected by the electron transfer pattern including surface-controlled, grain-controlled, and neck-controlled modes as shown in Figure 6.<sup>112,113</sup> Surface-controlled mode is generally related to the compact layer structures. Gases only affect its geometric surface other than the bulk solution; thus the sensitivity of the compact layer is mainly determined by the thin film thickness. On the contrary, all parts of the porous layer will be in contact with gases, which results in more activated sites in the porous layer. Because of this nondense contact manner, each grain possesses a surface depleted area, and current has to pass through the intergranular contacts; therefore, the sensitivity of nano-structured  $\text{TiO}_2$  is affected not only by the layer thickness, but also by the pore size and the carrier's diffusion length.

In both the receptor and the transducer processes presented above, the vacancy on  $\text{TiO}_2$  surface plays an important role, as shown in Figure 6a. When the film was exposed in air, oxygen will be adsorbed on these surface vacancies and form anionic oxygen. Therefore, the n-type doping density of the  $\text{TiO}_2$  surface will be reduced or even it will change into p-type, which will cause the formation of depletion region and band bending on the surface. The band bending on  $\text{TiO}_2$  surface will bring a barrier for carrier transport between the particles, and then cause the decrease of film conductivity. When reducing gas such as  $\text{H}_2$ ,  $\text{CO}$ ,  $\text{NH}_3$ ,  $\text{H}_2\text{S}$ , and VOCs is adsorbed on the surface anionic oxygen, electrons will be injected into  $\text{TiO}_2$  surface, which will reduce the depletion region and release the band bending; hence, the film conductivity will be improved. On the contrary, when oxidative gases like  $\text{NO}_2$  are adsorbed on  $\text{TiO}_2$  surface, it will gain electrons from anionic adsorbed oxygen, which will increase the depletion region, leading to the decrease of conductivity.

The conductivity change can be easily transferred into resistance signal, which is the best-known sensor output signal. In most cases, the measurement is operated at constant temperature by direct current measurement. Considering that resistance is also related to temperature and microstructure, TiO<sub>2</sub> sensor properties depend strongly on operating temperature and the semiconductor microstructure.

## 2.2. COD Sensor

In addition to monitoring the concentration of a single chemical, another system is developed focusing mainly on water pollutants, in which the total concentrations of all chemicals are monitored as a whole. To evaluate water quality, the monitoring index is related to the amount of organics degraded, specified as chemical oxygen demand. COD is a metric indicating the oxygen needed to oxidize certain organic matters in water bodies, especially in surface water (e.g., lakes, rivers) or wastewater. This index is of great importance for water resources protection because the drinking water supply cannot always meet the quality requirements, especially in most developing countries. Thus, water environment protection and related monitoring have been of great concern to the whole world. For this purpose, COD sensor is a cutting-edge technology developed in recent years.

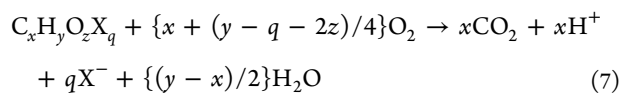
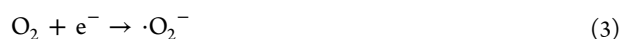
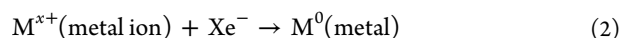
The principle for COD test is that nearly all organic compounds can be fully photocatalytic-oxidized to carbon dioxide with a strong oxidizing agent under acidic conditions. TiO<sub>2</sub> holds a strong capability in oxidizing organic matters under appropriate illumination, which makes TiO<sub>2</sub>-based photocatalytic/photoelectrocatalytic sensing techniques highly attractive in recent years in the field of environmental monitoring and environmental protection.<sup>87</sup> Among various COD test methods, TiO<sub>2</sub> COD sensor is superior to other methods<sup>114–119</sup> because of its superb oxidative abilities under illumination and its nontoxic, inexpensive, photostable, and environmentally friendly merits. Because of the promising application in the field of water quality analysis, it has quickly become a research focus.<sup>120</sup>

It is well-known that TiO<sub>2</sub> can generate electron/hole pairs under UV light, resulting in free photoelectrons in the conduction band ( $e_{cb}^-$ ) and photoholes in the valence band ( $h_{vb}^+$ ) as shown in eq 1. In an aqueous system, photoholes and photoelectrons play an important role in redox reactions of organic and inorganic compounds, which is the foundation of the TiO<sub>2</sub> COD sensor.



Photoholes possess powerful oxidation capability ( $E_g = +3.2$  eV) to mineralize most organic compounds as shown in Figure 7.<sup>120–123</sup> There are two pathways to achieve mineralization. In the first pathway, photoholes can directly oxidize species

adsorbed to the TiO<sub>2</sub> surface. The other pathway is through the oxidating function of hydroxyl radical,  $\cdot\text{OH}$ , a well-known strong oxidant that can be efficiently generated via water oxidation by the photoholes. In virtue of the strong oxidating power of the photogenerated holes, organics can be degraded by TiO<sub>2</sub> under UV illumination. In an aqueous system, the electrons at the surface of TiO<sub>2</sub> can reduce dissolved metal ion  $M^{x+}$  to  $M^0$  and also react with O<sub>2</sub> absorbed on TiO<sub>2</sub> to form singlet oxygen and hydroxyl radical (see eqs 2–6). The overall mineralization reaction can be represented by eq 7. These reactions are recognized as the foundation of TiO<sub>2</sub> COD sensor. Because of the superb photocatalytic oxidative capability of TiO<sub>2</sub> over traditional COD methods (e.g., potassium dichromate method), the TiO<sub>2</sub>-based COD method mentioned above better reflects the real organic pollutant concentrations in water bodies, which are represented as PcCOD (based on photocatalysis) or PeCOD (based on photoelectrocatalysis).



## 2.3. Biosensor

A biosensor is an analytical device, which converts a biological response into readable or quantified signal. Biosensors can be applied to analyze a variety of samples including body fluids, food samples, and cell cultures.<sup>124</sup> The immobilized biological recognition elements on the sensor substrates that have specific binding affinity to the target compounds interact with the targets in such a way that gives the biosensor high selectivity and sensitivity.<sup>125</sup> TiO<sub>2</sub> nanomaterials are excellent candidates for the immobilization of the biological components<sup>126,127</sup> due to these merits (e.g., low cost, high stability, and biocompatibility).

The applications of biosensing are commonly supported by the functions of electrochemical transducer, which are carried out by electrochemical techniques (e.g., amperometric and potentiometric process). In biosensing, especially electrochemical biosensing, the fundamental mechanism for extracting information is based on biochemical reactions.<sup>128</sup> Typically in (bio)electrochemistry, a measurable current (amperometric), a measurable potential, or charge accumulation (potentiometric) will be generated upon the alteration of the conductive properties of a medium between electrodes when the reaction takes place as shown in Figure 8. For this purpose, TiO<sub>2</sub> electrode is usually modified with enzyme, hemoglobin, antibody, antigen, cells, DNA, and bacteria corresponding to a specific target. In addition to collecting electrochemical signals, light transducer is another feasible media that makes an optical biosensor work. Surface plasmon resonance (SPR), electrochemiluminescence (ECL), and fluorescence are three main mechanisms in which the binding of biomolecules with targets would change the optical properties of electrode surface

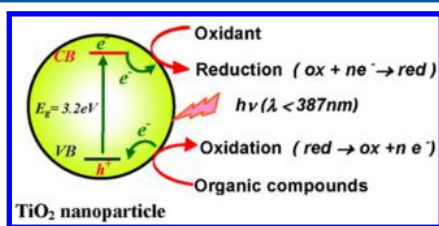


**Figure 7.** Typical photocatalytic oxidation and reduction processes at a TiO<sub>2</sub> nanoparticle. Reprinted with permission from ref 120. Copyright 2012 Elsevier.



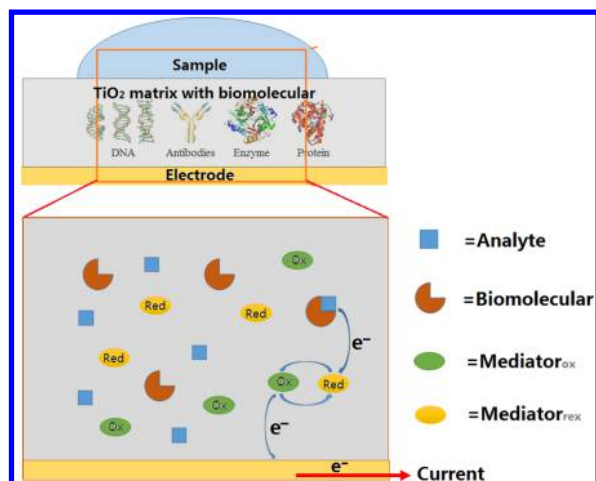


**Figure 8.** Schematic drawing of an amperometric sensor. Original drawing was done by us.

so that the variation of reflected or emitted light could be in proportion to the target concentration.

### 3. SENSOR APPLICATIONS

#### 3.1. Gas Sensor

**3.1.1. Measurement Principle.** For a gas sensor, the  $\text{TiO}_2$  electrode is fixed in a sealed chamber where the resistance of  $\text{TiO}_2$  film could greatly change when a gas stream passes through (see Figure 6). According to the sensing mechanism (section 2.1), the concentration of a specific gas could be detected by measuring resistance change in the  $\text{TiO}_2$  film. A simple method is to deposit two conductive pads on the  $\text{TiO}_2$  film for resistance measurement. There are two types of contacts: top contact and side contact. Top contact could be found in aligned 1D  $\text{TiO}_2$  nanostructure where two spring-loaded parallel metal pads are in electrical contact with the  $\text{TiO}_2$  film. For example, Grimes' group<sup>129</sup> developed a sensor device including a  $\text{TiO}_2$  NTs adopted for exploring gas sensing properties. In their work, the sensor consisted of a base

titanium metal foil and a nanotube array grown on the top. An insulating barrier layer separated the nanotubes from the conducting titanium foil. A pressure contact was used to electrically contact the nanotubes, with two spring-loaded parallel 10 mm by 2 mm platinum contact pads (100 mm thickness) (see Figure 9, type 1). Different from top contact, side contact is used for random  $\text{TiO}_2$  nanostructure. As reported by Zuruzi et al.,<sup>130</sup> nanosponge titania (NST) consisting of interconnected nanowalls and nanowires belongs to random 1D nanostructure. In this case, side contact was realized by depositing Ti/Pt on NST edges (see Figure 9, type 2). It is also commonly found in other  $\text{TiO}_2$  structures, such as dense film, mesoporous film, and opal film.

The performance of sensors can be characterized by some parameters including sensitivity, response time, recovery time, optimum working temperature, and detection limit. The detection sensitivity (response  $S$ ) in the presence of gases is usually defined in several different forms including  $S = R_a/R_g$ ,  $S = R_g/R_a$ ,  $S = \Delta R/R_g$ , and  $S = \Delta R/R_a$ , where  $R_a$  is the sensor resistance in ambient air,  $R_g$  is the sensor resistance in the target gas, and  $\Delta R = |R_a - R_g|$ . Response time is defined as the time required for a sensor to reach 90% of the total response upon exposure to the target gas. Recovery time is defined as the time required for a sensor to return to 90% of the original baseline signal upon removal of the target gas. Overall, a good gas sensor is characterized by high sensitivity, short response/recovery time, and high tolerance to temperature.

**3.1.2. Hydrogen ( $\text{H}_2$ ) Sensor.**  $\text{H}_2$  gas is an inflammable and explosive gas widely used in facilities, such as hydrogen fuel cells, semiconductor, food processing, and in petroleum industries. However, it is also colorless and odorless. This makes the rapid and accurate hydrogen detection highly important during its production, storage, and usage. Table 1 summarizes the different  $\text{TiO}_2$  nanomaterials and their performance in the detection of  $\text{H}_2$ .

The anatase is the most common crystal phase for  $\text{TiO}_2$  sensing material, and rutile is less favorable than anatase in terms of electron transportation and less sensitive due to its large grain size. The composition and nanostructure of  $\text{TiO}_2$

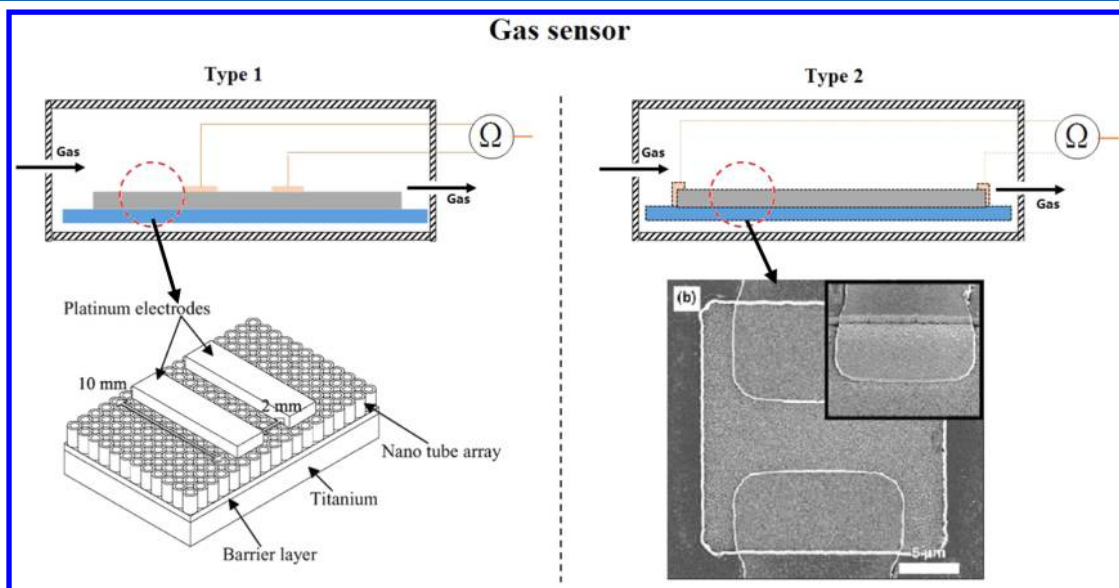


**Figure 9.** Schematic representation of the electrode geometry for gas sensing. Type 1: Reprinted with permission from ref 129 Copyright 2003 Elsevier. Type 2: Reprinted with permission from ref 130. Copyright 2007 Wiley-VCH.

Table 1. Summary of the Sensing Properties of TiO<sub>2</sub> Nanomaterial-Based H<sub>2</sub> Sensor

TiO <sub>2</sub> nanostructure	substrates	fabrication method	size	crystal structure	detection range	detection temp (°C)	response				ref
							temp (°C)	sensitivity <sup>a</sup>	response time	recovery time	
TiO <sub>2</sub> NTs	Ti foil	anodization	D: 46 nm; L: 400 nm	anatase/rutile	100 ppm–4%	180–400	290	~10 <sup>3</sup> (C)	150 s		129, 2003
TiO <sub>2</sub> (NST)	Si	wet oxidation				275		~10 <sup>4.7</sup>	814 s		130, 2007
porous TiO <sub>2</sub>	Ti plate	thermal oxidation			50–10000 ppm	150–300	300	1.2 × 10 <sup>6</sup> (A)	2 s		135, 2005
mesoporous Nb <sub>2</sub> O <sub>5</sub> /TiO <sub>2</sub>	gold paste	sol–gel	D: 4.1 nm	anatase		300–550	450	~5.5 (A)	~1 min	~1 min	136, 2002
Pd/TiO <sub>2</sub> nanopores	Ti foil	anodization	D: 50–130 nm	anatase	0.01–1%	250–500	250	10 (A)	10 s	1 min	137, 2002
TiO <sub>2</sub> NTs	Ti foil	anodization	D: 22 nm; L: 200 nm	anatase/rutile	0–500 ppm	290	290	~100 (D)			141, 2003
TiO <sub>2</sub> NTs	Ti foil	anodization	D: <100 nm; L: 430 nm	anatase		RT	RT	~10 <sup>4</sup> (A)			142, 2012
Pt/TiO <sub>2</sub> NTs	Ti foil	anodization	D: 100 nm; L: 2 μm	anatase/rutile	10–3000 ppm	RT	RT	~10 <sup>7</sup> (C)	13 s	120 s	143, 2012
TiO <sub>2</sub> NTs	Ti foil	anodization	D: 20–150 nm; L: 20 μm	anatase		RT	RT	~10 <sup>3</sup> (D)	2 h		144, 2006
Pd/TiO <sub>2</sub> NTs	Ti foil	anodization	D: 76 nm; L: 400 nm	anatase/rutile		RT	RT	~10 <sup>4</sup> (D)			107, 2004
Pd/TiO <sub>2</sub> NTs	Ti/glass	anodization	D: ~20 nm; L: ~600 nm	anatase		25–250	RT	~10 <sup>4</sup> (S)	30 s		158, 2006
Au/TiO <sub>2</sub> NTs	Ti foil	anodization	D: 100 nm; L: 430 nm	anatase/rutile		RT	RT	~10 <sup>4</sup> (A)	1500 s	1000 s	162, 2010
Nb/TiO <sub>2</sub> NTs	Ti foil	anodization	D: 65 nm; L: 1 μm	anatase	50 ppm–2%	RT	RT	~40% (F)	12 s		142, 2012
Al/V/TiO <sub>2</sub> NTs	Ti6Al4V alloy	anodization	D: 65 nm; L: 800 nm	anatase		25–300	RT	0.6 (F)			164, 2013
Pd/TiO <sub>2</sub> nanofibers		electrospun	D: 117.2 nm; L: 5–10 nm	anatase	0.3–2%	RT	RT	~5.43% (F)			145, 2009
TiO <sub>2</sub> nanofiber			D: 5–10 nm; L: 0.2–1 μm	rutile	0.5–2%	300–600	400	1.25 (B)	1–2 min	5–7 min	146, 2005
TiO <sub>2</sub> (NST)	Si	wet oxidation	D: 20–80 nm; L: 100–800 nm	rutile	100–1000 ppm	50–300	250	10 (A)	7 s		147, 2008
TiO <sub>2</sub> NWs						RT		8 (A)			148, 2007
Pt/TiO <sub>2</sub> /MWCNTs	alumina	sol–gel		anatase	5–100%	RT–100	50	30% (F)			149, 2012
CNTs/ Pt-TiO <sub>2</sub> NTs	Ti foil	anodization	D: 100 nm; L: 14 μm	anatase	0.5–3%	100–150	100	2% (F)			150, 2012
Pd/TiO <sub>2</sub> nanopores	gold	anodization/UV	D: 300–330 nm	rutile	500–1000 ppm	200–400	300	99% (F)	6 s	119	151, 2006
TiO <sub>2</sub> /NiO	NiO	sputtering			200 ppm–0.5%	250–350	300	15 (B)	2 min	2.3 min	152, 2000
PtO/Pt/TiO <sub>2</sub>	glass	sol–gel			1–10%	180–200	180	40% (F)	~10 min	~10 min	153, 2008
TiO <sub>2</sub> NTs	Ti foil	anodization	D: 90 nm; L: 1 μm	anatase/rutile	100–5000 ppm	25–150	RT	17 (D)	65 min		166, 2010
Au/TiO <sub>2</sub>	silica glass	sol–gel		anatase	8.5–510 ppm		300	~30 (A)	0.06 min	1.3 min	167, 2002

<sup>a</sup>A, S = R<sub>g</sub>/R<sub>g</sub>; B, S = R<sub>g</sub>/R<sub>g</sub>; C, S = ΔR/R<sub>g</sub>; D, S = ΔR/R<sub>g</sub>; E, S = (ΔR/R<sub>g</sub>) × 100%; and F, S = (ΔR/R<sub>g</sub>) × 100%. Diameter, D; length, L; room temperature, RT.

film have a dramatic influence on the sensor performance in the detection of hydrogen. Earlier research<sup>131–134</sup> reported compact TiO<sub>2</sub> film for H<sub>2</sub> sensing, in which the performances were limited in detection range and sensitivity. A similar result was found by Jun et al.<sup>135</sup> who fabricated the TiO<sub>2</sub> sensor by thermal oxidation of Ti plate. In their work, dense film showed poor performance as compared to porous film obtained by removing the outer dense layer. Under operation temperature of 300 °C, the porous inner layer showed a rapid decrease in the resistance after exposure to H<sub>2</sub> gas, and the response time was significantly reduced from 500 to 2 s. Moreover, the signal was also quite stable, and the sensitivity (10<sup>4</sup>) was much higher than that (~10) of the specimen obtained by thermal oxidation only. This suggested that a larger sensor surface area could help improve sensor performance because it enhances the absorption of H<sub>2</sub> molecules, thus increasing the sensitivity to the resistance change. In addition to porous TiO<sub>2</sub> film, Devi et al.<sup>136</sup> reported a mesoporous TiO<sub>2</sub> sensor by employing a modified sol–gel method. A large surface area of 66.3 m<sup>2</sup> g<sup>−1</sup> advantages this sensor with a high sensitivity of 10 when exposed to 500 ppm H<sub>2</sub> gas. TiO<sub>2</sub> nanopore electrode was fabricated by Shimizu et al.<sup>137–139</sup> using an anodization method to oxidize Ti foil in H<sub>2</sub>SO<sub>4</sub> electrolyte. With TiO<sub>2</sub> nanopore electrode,<sup>137</sup> a sensitivity of 10 with a response time of 10 s and recovery time of 1 min was achieved at 250 °C when exposed to 1% H<sub>2</sub> gas. Porous TiO<sub>2</sub> layer showed better performance than compact layer, and the variation trends were in accordance with the analysis in section 2.1. Therefore, nano structured TiO<sub>2</sub> (i.e., TiO<sub>2</sub> NTs) that provides a larger surface area and favors electron transfer is the target material for gas sensor development.

The tubular-structured TiO<sub>2</sub> NTs show excellent performance for H<sub>2</sub> detection. TiO<sub>2</sub>NTs prepared on anodic oxidation using HF electrolyte in place of H<sub>2</sub>SO<sub>4</sub> showed superior performance over other TiO<sub>2</sub> matrix,<sup>140</sup> thereby attracting much attention in recent years. The geometry of TiO<sub>2</sub> NTs could be varied in a large scope using different electrolytes and voltages as discussed in section 1.2.1. Therefore, it is an area of research emphasis to investigate the relationship between sensing performance and geometry. A series of TiO<sub>2</sub> NTs with 200–400 nm length and 20–40 nm pore size were prepared,<sup>141</sup> and it is found that the shorter TiO<sub>2</sub> NTs with 200 nm length and 20 nm pore size delivered better performance, which can be attributed to the larger surface area. The best result was obtained with a detection range of 0–500 ppm (see Figure 10) and a sensitivity of 10<sup>−4</sup> at 290 °C for 1000 ppm H<sub>2</sub>. A similar result was confirmed by Asl et al.<sup>142</sup> who investigated the effect of TiO<sub>2</sub> NTs structures on sensing performance. In addition, some research revealed that 1–2 μm TiO<sub>2</sub> NTs also showed a comparable performance in H<sub>2</sub> sensing. Chen et al.<sup>143</sup> fabricated 2 μm TiO<sub>2</sub> NTs for H<sub>2</sub> sensing. In their work, the sensors exhibited 7 orders of magnitude change in resistance with a response time of 13 s at room temperature on exposure to 2000 ppm H<sub>2</sub>. However, much longer TiO<sub>2</sub> NTs (e.g., over 10 μm) showed considerably decreased performance in all aspects, such as sensitivity, response time, and recovery time. Yoriya et al.<sup>144</sup> investigated over 10 μm TiO<sub>2</sub> NTs fabricated in organic electrolyte for H<sub>2</sub> sensing. They found that the recovery time was up to several hours, which imposed a great limitation on their real application. Overall, it implies that more H<sub>2</sub> molecules can be absorbed due to the larger surface area, but their desorption from long nanotubes becomes more difficult than that from short nanotubes. Therefore, a tradeoff between

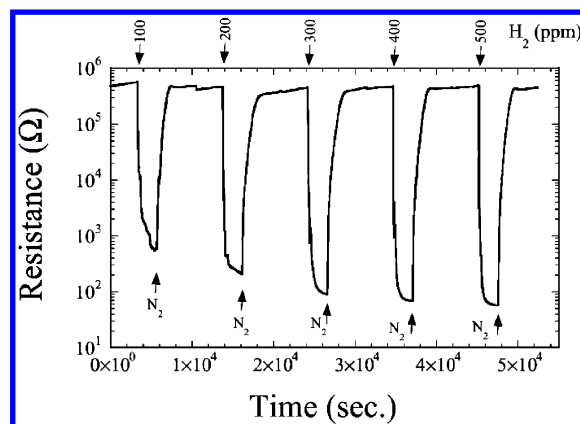


**Figure 10.** Electrical resistance of 22 nm diameter, 360 nm long TiO<sub>2</sub> nanotube arrays when exposed to different hydrogen concentrations at 290 °C. Reprinted with permission from ref 141. Copyright 2003 Wiley-VCH.

the surface area and response time needs to be considered. So far, the optimal length is considered to be in the range of approximately 200 nm to 2 μm. The dramatic structural variation in the pore size, diffusion depth, or the film thickness of nano-TiO<sub>2</sub> layer could make a difference in the approachability of the target gas to the inner grains and, in turn, in sensing performances.

In addition to the sensors with TiO<sub>2</sub> NTs, other nanostructured/composite TiO<sub>2</sub> sensors were also developed.<sup>130,145–153</sup> Zuruzi et al.<sup>130</sup> developed a patterned 3D interconnected NST for H<sub>2</sub> detection. The NST was sponge-like and consisted of interconnected nanowalls and nanowires, which, for the first time, experimentally achieved 1 ppm, the lowest detectability limit for H<sub>2</sub> using undoped nanostructured titania (see Figure 11). Jia et al.<sup>145</sup> developed TiO<sub>2</sub> nanofibrous membrane with a continuous Pd layer for H<sub>2</sub> detection at room temperature. The sensor exhibited tunable resistance change behavior when exposed to different H<sub>2</sub> concentrations.

Generally, in terms of film geometry, nanostructured TiO<sub>2</sub> exhibits higher sensitivity and stability due to increased surface area as well as increased electron transport through percolating nanoscopic “necks”. This is different from processes on nanoparticle agglomerates, where electron transport occurs at contact points across nanoparticles. In a nanotubular structure, however, there are no contact spots. Consequently, electron transport experiences much less hindrance, thus higher sensor sensitivity and stability. Apparently, the structure with biggest resistance variation is most favorable for H<sub>2</sub> gas detection. Reviewing the H<sub>2</sub> sensor based on different TiO<sub>2</sub> nanomaterials, TiO<sub>2</sub> NTs-based H<sub>2</sub> sensor is taking prominence for its remarkable performance; for example, TiO<sub>2</sub> NTs<sup>142</sup> showed a sensitivity of ~10<sup>4</sup> as compared to 30 obtained by TiO<sub>2</sub> nanoparticles.<sup>167</sup>

Operating temperature is another important factor in H<sub>2</sub> sensing. Operating temperature of TiO<sub>2</sub> sensor increase could accelerate the diffusivity of the hydrogen atoms into the surface of TiO<sub>2</sub> matrix and thus lead to a higher sensitivity.<sup>154</sup> However, too high of a temperature is not acceptable in view of energy cost or environment safety. Therefore, trying to decrease the working temperature for H<sub>2</sub> sensing is another important focus. Noble metals (e.g., Pt, Pd, Au, or Ag) are highly valued because they could effectively improve the interaction between TiO<sub>2</sub> surface and gas molecules, thereby



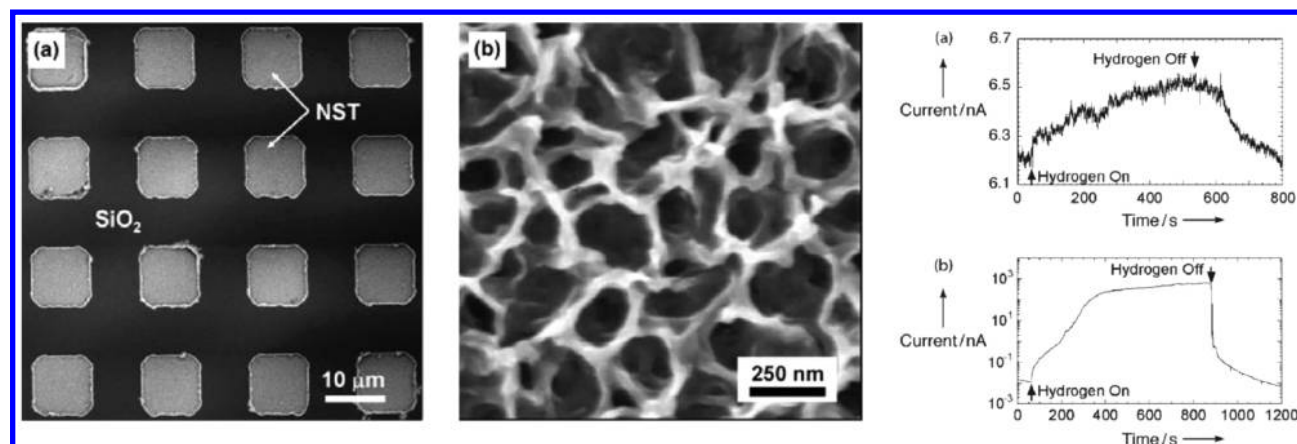


**Figure 11.** (Left and middle) SEM images of NST. (Right) Variation of current with time in the presence of (a) 1 ppm of H<sub>2</sub> gas in vacuum (25 °C) and (b) 4000 ppm of H<sub>2</sub> in synthetic air (275 °C). Reprinted with permission from ref 139. Copyright 2007 Wiley-VCH.

**Table 2.** Summary of the Sensing Properties of TiO<sub>2</sub> Nanomaterial-Based O<sub>2</sub> Sensor

TiO <sub>2</sub> nanostructure	fabrication method	substrates	size	crystal structure	detectionrange	response					ref
						temp (°C)	sensitivity <sup>a</sup>	response time	recovery time	concentration	
macroporous TiO <sub>2</sub>	AAO/RIE	P-Si	D: 100–750 nm	anatase		RT	10% (F)			1500 ppm	180, 2010
TiO <sub>2</sub> nanosponge	wet oxidation	Ti/SiO <sub>2</sub> /Si			0.3–0.8 mTorr	250	60 (B)	16 s		0.8 mTorr	181, 2006
TiO <sub>2</sub> NTs	anodization	Ti	D: 150 nm L: 2.3 μm	amorphous	>200 ppm	100	160 (D)	~500 s	~1000 s	4%	183, 2008
Pt//TiO <sub>2</sub>	sol–gel	alumina		anatase	O <sub>2</sub> in engine	630		~2 s			190, 2007
Pd/TiO <sub>2</sub>	ultrasonic spray pyrolysis	alumina		anatase	100–1000 ppm	300	1.18 (D)	70 s		100 ppm	191, 2007
Nb/TiO <sub>2</sub>	TiO <sub>2</sub> powder	alumina		rutile		400	221 (B)	2 s		1200 ppm	198, 1999
Nb/TiO <sub>2</sub>	sol–gel	alumina		rutile	10–20 ppm	500	1.6 (D)			10 ppm	200, 2007
V <sub>2</sub> O <sub>5</sub> /TiO <sub>2</sub>	sol–gel		3–5 nm		1 ppm–20.9%	250	3.5 (B)	5 min	30 min	120 ppm	201, 2001
CeO <sub>2</sub> /TiO <sub>2</sub>	sol–gel	alumina			5–10 000 ppm	420	~3 (B)	40–60 s	80 s	1000 ppm	203, 2003
SnO <sub>2</sub> /TiO <sub>2</sub>	sputtering	SiO <sub>2</sub> /Si/glass	44–67 nm	anatase	100–2000 ppm		2 (B)			1000 ppm	205, 2006
carbon NT/TiO <sub>2</sub>	sol–gel	alumina		anatase/rutile	10 ppm	350	6.5 (D)	8 s		10 ppm in CO <sub>2</sub>	206, 2008

<sup>a</sup>A,  $S = R_a/R_g$ ; B,  $S = R_g/R_a$ ; C,  $S = \Delta R/R_g$ ; D,  $S = \Delta R/R_a$ ; E,  $S = (\Delta R/R_g) \times 100\%$ ; and F,  $S = (\Delta R/R_a) \times 100\%$ . Diameter, D; length, L; room temperature, RT.

reducing the operation temperature.<sup>107,155–158</sup> An enhanced performance is achieved by a catalytic boost via the so-called spill-over effect<sup>159–161</sup> as noble metal particles favor gas molecule adsorption and desorption, achieving higher concentration of adsorbed ionic oxygen at lower temperature. In the work of Varghese,<sup>129</sup> 10 nm layer of palladium was coated on TiO<sub>2</sub> NTs by evaporation. These sensors exhibit a resistance variation of the order of 10<sup>4</sup> in the presence of 100 ppm hydrogen at 25 °C. On the contrary, in lack of Pd, the sensing performance could be dramatically reduced. For example, at room temperature, the response time of TiO<sub>2</sub> NTs sensor increased to 90 min. Moreover, Au doped TiO<sub>2</sub> matrix was also studied to make sensor work at room temperature.<sup>142,162</sup> Asl et al.<sup>142</sup> fabricated Au doped TiO<sub>2</sub> NTs and successfully got a sensitivity of ~10<sup>4</sup> on exposure to 1% H<sub>2</sub> at room temperature.

However, the response time and recovery time are about 1500 s longer than that of Pb decorated TiO<sub>2</sub> NTs.

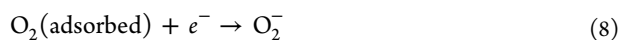
Liu et al.<sup>163</sup> reported that Nb doped TiO<sub>2</sub> NTs had good performance in H<sub>2</sub> sensing at room temperature and achieved a wide detection range at both diluted and high-concentrated hydrogen atmospheres ranging from 50 ppm to 2% H<sub>2</sub>. When exposed to 2% H<sub>2</sub>, a sensitivity of 40% with a response time of 12 s was achieved. They also found that anatase-TiO<sub>2</sub> had short response time. However, rutile phase at higher annealing temperature may be unfavorable for room-temperature hydrogen sensing with the Nb-doped nanotubes. Li et al.<sup>164</sup> investigated Al- and V-doped TiO<sub>2</sub> NTs by the anodization of Ti<sub>6</sub>Al<sub>4</sub>V alloy. Different from most n-type sensors, the doped nanofilms presented a p-type hydrogen sensing behavior by showing increased resistance upon exposure to the hydrogen-containing atmosphere and exhibited a distinct resistance

change at room temperature with 1000 ppm H<sub>2</sub>. Luca et al.<sup>149</sup> developed a sensor suitable for room temperature using Pt/TiO<sub>2</sub>/MWCNTs (multiwall carbon nanotubes) composites. The increased resistance in response to H<sub>2</sub> possibly indicates a p-type conduction mechanism of the composite sensing material.

External factors should be considered that could directly influence the performance of the sensors. For example, in humid condition physisorption of water molecules takes place on a layer of initially chemisorbed OH radicals at the TiO<sub>2</sub> surface and reduces the base resistance of the TiO<sub>2</sub>. The adsorbed water molecules block the active sites where hydrogen chemisorption occurs, thus reducing its sensitivity. Oxygen in air may be chemisorbed in the form of O<sub>2</sub> on the nanotube surface by trapping electrons from its conduction band, creating an enhanced base resistance.<sup>165</sup> Hydrogen can remove this chemisorbed oxygen, thus reducing the resistance. The high sensitivity in the absence of oxygen indicates that direct chemisorption of hydrogen on the TiO<sub>2</sub> is the dominant mechanism leading to tremendous reduction of TiO<sub>2</sub> resistance, while the presence of oxygen facilitates removal of the chemisorbed hydrogen.

**3.1.3. Oxygen (O<sub>2</sub>) Sensor.** Undisputedly, highly sensitive and fast responding O<sub>2</sub> gas detector is in high demand and of great interest. Various semiconductor oxides have been proposed<sup>168–172</sup> for their sensitivity toward oxygen at different operating temperatures. Among them, TiO<sub>2</sub> is a good potential candidate. Table 2 summarizes the TiO<sub>2</sub> nanomaterials and their performance in the detection of oxygen.

The basic principle behind O<sub>2</sub> detection is tracing the resistance increase in TiO<sub>2</sub> material as described in section 2.1 when exposed to oxygen gas. This change is mainly due to oxygen vacancies and interstitial oxygen ions working at electron donating states. These states permit the adsorption of oxygen ion monolayer or the formation of additional donors near the surface. The reoxidation of oxide lattice is represented in eqs 8 and 9, which show that the oxygen ion-sorption results in a general resistance increase.<sup>27</sup>



The most significant application for O<sub>2</sub> sensor is monitoring O<sub>2</sub> concentration change in engine. TiO<sub>2</sub>-based O<sub>2</sub> sensor is among the earliest sensors studied. Ford Motor Co. made the first attempt to develop such sensors in industry,<sup>173</sup> in which ceramic titania pellets were used. A small addition of donors extended the monotonically region to 0.2 bar (air). A few years later, titania thick-film sensors were developed by several companies<sup>174,175</sup> and constantly improved.<sup>176–179</sup> Among these sensors, the company (NGK-NTK) developed a series of sensors for hybrid system using screen-printed thick-films on ceramic, cofired tapes.

Similarly, like H<sub>2</sub> sensor, the O<sub>2</sub> sensor's performance is also affected by the microstructure of the film.<sup>180–186</sup> Porous TiO<sub>2</sub> film shows superior advantage over compact due to large surface area, delivering a better performance in oxygen sensing. Lu et al.<sup>180</sup> developed a macroporous TiO<sub>2</sub> oxygen sensor, using anodic aluminum oxide as an etching mask, in which TiO<sub>2</sub> nanofilms was deposited on the macroporous Si wafer surface. In this work, it was revealed that macroporous geometry of the TiO<sub>2</sub> chemo-resistive gas sensor demonstrated

2-fold higher (~33%) improved sensitivity than a nonporous sensor at different levels of oxygen exposure.

Zuruzi et al.<sup>181</sup> proposed an approach in which micrometer-scale patterned sponge-like TiO<sub>2</sub> arrays were used as elements for O<sub>2</sub> sensing. The sensing devices were fabricated first by depositing Ti film on SiO<sub>2</sub> and subsequently another layer of SiO<sub>2</sub> substrate and then etching the outer layer of SiO<sub>2</sub> to expose Ti patterns, which were then oxidized and annealed. At oxygen pressures ranging from 0.3 to 0.8 mTorr and operation temperature of 250 °C, conductance of the material was approximately 1 order of magnitude less than that in vacuum with a response time of 48 s. Because this sensor showed minimal drift of electrical properties over time, it gave the sensor the ability to detect low oxygen partial pressures, for instance, the in situ detection of oxygen content during high-vacuum deposition of complex oxides.

TiO<sub>2</sub> NTs-based oxygen sensors, which were growing from Ti substrate via anodization, were reported by Lu et al.<sup>183</sup> TiO<sub>2</sub> NTs have highly ordered open tubes and large specific surface area, which can provide abundant sites and channels for gas adsorption, diffusion, and chemical reaction. In this work, TiO<sub>2</sub> NTs-based sensors were tested at different temperatures (50, 100, 150, 200, 250, and 300 °C) when exposed to various oxygen concentrations. The amorphous TiO<sub>2</sub> NTs showed high sensitivity, excellent recovery property, and linear relationship regarding its resistance and oxygen concentration at 100 °C with a distinct variation of electrical resistance up to 2 orders of magnitude. However, the resistance responses above 180 °C show poor recovery property. Interestingly, the sensitivity of anatase TiO<sub>2</sub> NTs had no linear relationship with oxygen concentrations and was much lower than that of the amorphous sensor. This result is attributed to the change of charge carrier concentration on the nanotube surface. The amorphous nanotube structure is more disordered than that of anatase nanotubes, thereby showing more defects, which provide abundant local donor energy levels. The donor energy levels could provide abundant local donor energy levels and enhance conductivity, that is, the concentration of charge carriers.

In addition to nanostructure of TiO<sub>2</sub> film, catalytical activation is favored for the enhancement of oxygen surface reaction. Because of the positive effect of noble metals, many studies<sup>187–192</sup> focused on coupling them with anatase TiO<sub>2</sub> as a catalyst to improve sensor sensitivity and shorten response time. Francioso et al.<sup>190</sup> evaluated a Pt-doped TiO<sub>2</sub> sensor in a real gasoline engine in comparison with a commercial probe (Bosch). In their results, comparable performance was achieved despite a little longer response time. Castañeda et al.<sup>191</sup> proposed a Pd/TiO<sub>2</sub> thin film for detecting oxygen, by which they achieved sensitivity of stationary value of 1.18 to over 2.0 for O<sub>2</sub> concentration in the range of 100–1000 ppm at 300 °C.

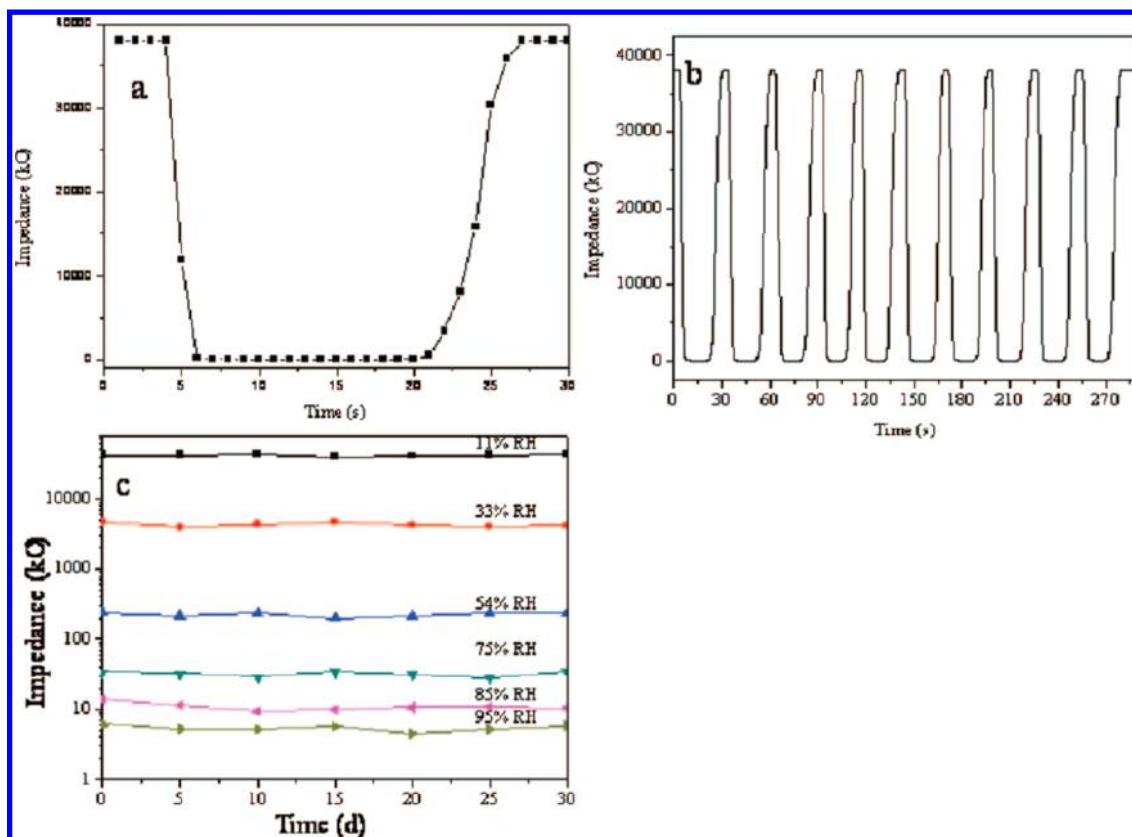
On the other hand, O<sub>2</sub> sensor might require relatively high working temperature, in which rutile is commonly used as the sensing material. However, because the grain size of rutile is larger than the space charge layer, it will decrease the electron transfer efficiency and thus sensitivity. To control the grain size of rutile, doping TiO<sub>2</sub> with metal ions such as Ta, La, Nb, and Cr is feasible.<sup>193–197</sup> Cr and Nb doped TiO<sub>2</sub> was investigated by Sharma et al.<sup>193,198,199</sup> who acquired an improvement in sensitivity and response time based on doped TiO<sub>2</sub>. The doped material also shows lower impedance at low operating temperatures; hence the design of the associated electronic circuitry is simplified. Sotter et al.<sup>200</sup> optimized the atomic ratio of Nb to Ti in the composite film to 3% and the calcination

Table 3. Summary of the Sensing Properties of TiO<sub>2</sub> Nanomaterial-Based Humidity Sensor<sup>a</sup>

TiO <sub>2</sub> nanostructure	fabrication method	substrates	size	crystal structure	detection range	detection temp	response				reproducibility	ref
							sensitivity <sup>a</sup>	response time (s)	recovery time (s)	concentration		
TiO <sub>2</sub> NWs/Nafion		alumina	D: 40–50 nm L: 5–10 μm	anatase/rutile	12–97% (RH)	RT	10 (A)	<90	<90	40%	stable in 250 da	213, 2006
TiO <sub>2</sub> NTs	anodization	Ti foil	D: 100 nm L: 270 nm	anatase/rutile	11–95% (RH)	RT		100	190			214, 2008
LiCl/TiO <sub>2</sub> NFs			D: 150–260 nm	anatase/rutile	11–95% (RH)	RT	10 <sup>3</sup> (A)	3	7	11–95%	stable in 30 da	215, 2008
porous TiO <sub>2</sub>	sol-gel	prism		anatase	5–95% (RH)	RT	~187.79 (H)					216, 2007
porous TiO <sub>2</sub>	sol-gel	ceramic		anatase	11–95% (RH)	RT	10 <sup>4</sup> (A)	5	8	11–95%	stable in 30 da	217, 2011
porous TiO <sub>2</sub>		alumina	0.99–18.8 μm	anatase	10–100% (RH)	RT	10 <sup>4</sup> (A)			10–100%		218, 2004
Ce <sub>2</sub> O <sub>3</sub> /TiO <sub>2</sub> /SnO <sub>2</sub>	sol-gel	alumina		anatase/rutile	15–95% (RH)	RT	100 (A)			40%		225, 2010
potassium tantalate/TiO <sub>2</sub>			13.9–16.2 nm		20–90% (RH)	RT	10 <sup>3</sup> (A)					226, 2005
NaPSS/TiO <sub>2</sub> opal	sol	alumina	D: 1000nm	anatase	11–95% (RH)	RT	10 (A)	2	20	45%		227, 2009
PPy/Ag/TiO <sub>2</sub> NPs		QCM	13.5 nm		173.9–9711 ppm <sub>v</sub>	RT	0.0246 Hz/ppm <sub>v</sub>	12		55.0 ppm <sub>v</sub>		228, 2008
TiO <sub>2</sub> /PPy/PMAPTAC		PET			13–90% (RH)	RT	~6 (G)	30	45	60%	stable in 43 da	229, 2008
TiO <sub>2</sub> /PPy		alumina			30–84% (RH)	RT	~5.5 (G)	40	20	30%		230, 2007

<sup>a</sup>A, S = R<sub>a</sub>/R<sub>g</sub>; B, S = ΔR/R<sub>g</sub>; C, S = R<sub>g</sub>/R<sub>g</sub>; D, S = ΔR/R<sub>g</sub>; E, S = (ΔR/R<sub>g</sub>) × 100%; F, S = (ΔR/R<sub>g</sub>) × 100%; G, S = log Z<sub>i</sub> and H, S = ΔI<sub>r</sub>/ΔRH. Diameter, D; length, L; room temperature, RT.





**Figure 12.** Response and recovery characteristic curves based on the product containing 30.0% LiCl-doped  $\text{TiO}_2$  nanofibers for 1 cycle (a) and 10 cycles (b). (c) Stability of the sensor after exposing in air for 30 days. Reprinted with permission from ref 215. Copyright 2008 American Chemical Society.

temperature to 700 °C, respectively. When sensors operated at 500 °C, its highest sensitivity was achieved toward a low concentration of oxygen (10 ppm). The sensitivity improvement of Nb doped  $\text{TiO}_2$  sensor can simply be explained by the catalytic effect of Nb that provides more active sites to absorb more oxygen molecules.

Apart from  $\text{TiO}_2$ , many other semiconductors are also sensitive to oxygen. Thus, combining these semiconductors with  $\text{TiO}_2$  to form composite semiconductor would have a synergetic effect, which might improve sensor performance.<sup>201–207</sup> Zhuiykov<sup>201</sup> developed a  $\text{V}_2\text{O}_5$ – $\text{TiO}_2$  thin film using sol–gel method for oxygen sensor. The film thus combined showed a tremendously reduced resistance, and in real application the sensor can accurately measure oxygen concentrations from about 1 ppm to 20.9% at the temperature of 200–250 °C. However, longer response and recovery time manifested themselves. Trinchi et al.<sup>203</sup> proposed  $\text{CeO}_2$ – $\text{TiO}_2$  thin film, which exhibited shorter response and recovery time across all operating temperatures. Furthermore, the response and recovery time both decrease with higher oxygen concentrations for all of the sensors. The response time at 420 °C was typically between 40 and 60 s, whereas the recovery time was approximately 80 s. To achieve more miniaturized oxygen sensors, and to address the problem of thermal expansion mismatching between yttria-stabilized-zirconia (YSZ) and  $\text{CeO}_2$ – $\text{TiO}_2$ , the ternary  $\text{CeO}_2$ – $\text{ZrO}_2$ – $\text{TiO}_2$  electrode was developed to replace  $\text{CeO}_2$ – $\text{TiO}_2$ .<sup>204</sup>

Llobet et al.<sup>206</sup> proposed carbon nanotube– $\text{TiO}_2$  hybrid films for detecting traces of  $\text{O}_2$ . The good potential of carbon nanotubes (CNTs) for detecting gases arises from their very

large surface area because of their central hollow cores and outside walls. Researchers compared the hybrid layers based on titania and carbon nanotubes with Nb doped  $\text{TiO}_2$  films, which shows that the former gives 4 times higher sensitivity than the latter. Furthermore, hybrid sensors containing carbon nanotubes respond at significantly lower operating temperatures than their nonhybrid counterparts. These new hybrid sensors show a great potential for monitoring traces of oxygen (i.e., 10 ppm) in  $\text{CO}_2$  gas flow, which is of interest for the carbonated beverage industry.

Wang et al.<sup>207</sup> synthesized  $\text{TiO}_2$ /graphene composite film for  $\text{O}_2$  sensing upon exposure to UV light. They found that the presence of photoactive  $\text{TiO}_2$  thin films promoted the reactions of oxygen ions absorbed on the surface, thereby improving the performance. In their work, the detection range was 5–100% with a detection limit of 0.01% at room temperature. The response time and recovery time were 130 and 260 s, respectively. They suggested that the photoexcitation of  $\text{TiO}_2$  thin film activates  $\text{TiO}_2$  ground-state electrons into an excited state, which subsequently produces scattering sites for hole carriers that flow through graphenes. These active scattering sites can quench hole carriers and therefore lower its mobility in p-type semiconductor devices. However, the introduction of oxygen gas leads to the formation of negatively charged oxygen anions by the reaction between the activated electron and oxygen. This decreases the scattering sites, releases hole carriers back into the conducting channel, and therefore reverses the high conductance state of graphenes.

**3.1.4. Humidity ( $\text{H}_2\text{O}$ ) Sensor.** Humidity sensors have been increasingly applied in industry and environmental

control. During the manufacture of integrated circuits in semiconductor industry, humidity level is constantly monitored in wafer processing. They are also applied in many other fields, such as environment intelligent control systems in buildings, rear-window defoggers, pharmaceutical processing, greenhouse air-conditioning, and chemical gas purification. Table 3 summarizes the  $\text{TiO}_2$  nanomaterials and their performance in the detection of humidity.

Different from detection of other gases,  $\text{TiO}_2$  for  $\text{H}_2\text{O}$  monitoring should be considered as ceramic sensing material rather than semiconductor in terms of sensing mechanism.<sup>165,208</sup>  $\text{H}_2\text{O}$  condensed on the surface of the materials will be conducted when formed as water layers. For ionic sensing materials, if the humidity increases, the conductivity will decrease and the dielectric constant will increase. In bulk water, proton is the dominant carrier responsible for electrical conductivity. The conduction is ascribed to the Grotthuss mechanism, through which protons tunnel from one water molecule to the next via hydrogen bond that universally exists in liquid-phase water.<sup>209,210</sup> Because humidity sensing is usually realized by the adsorbed proton-conducting water layers on the porous structure at room temperature,<sup>211,212</sup> both anatase and rutile phases should behave approximately the same in resistance or capacitance changes.

It has been reported that nanostructured  $\text{TiO}_2$  facilitates the adsorption process of water vapors due to larger surface area. Some typical  $\text{TiO}_2$  nanostructures such as  $\text{TiO}_2$  nanowires,<sup>213</sup>  $\text{TiO}_2$  NTs,<sup>214</sup>  $\text{TiO}_2$  nanofibers,<sup>215</sup> and porous  $\text{TiO}_2$ <sup>216–218</sup> are much favored. Li et al.<sup>215</sup> fabricated LiCl-doped  $\text{TiO}_2$  nanofibers using electron spun method for humidity sensing. As shown in Figure 12, the sensor showed fast response and short recovery time (3 and 7 s, respectively) as well as good sensitivity of 3 orders of magnitude ( $10^7$ – $10^4$   $\Omega$ ) in the range of 11–95% RH.

On the other hand, doping with alkali ions may improve the conductivity of  $\text{TiO}_2$ .<sup>219–221</sup> Adding  $\text{SnO}_2$  resulted in porosity increase of  $\text{TiO}_2$  and thus enhanced sensitivity when environment relative humidity (RH) is higher than 70%.<sup>222</sup> What is more, bilayered combinations such as  $\text{TiO}_2/\text{Al}$ -doped  $\text{ZnO}$ <sup>223</sup> and  $\text{ZrO}_2/\text{SnO}_2$ <sup>224</sup> were proved to show less hysteresis effects than pure  $\text{TiO}_2$ , Al-doped  $\text{ZnO}$ , or  $\text{ZrO}_2$ . The reason is that one component material in these paired combinations works for fast-adsorption and the other one works for fast-desorption. Similarly, other composites such as  $\text{Ce}_2\text{O}_3/\text{TiO}_2$ ,<sup>225</sup>  $\text{KT}/\text{TiO}_2$ ,<sup>226</sup>  $\text{NaPSS}/\text{TiO}_2$ ,<sup>227</sup> and  $\text{PPy}/\text{TiO}_2$ <sup>228–230</sup> also showed improved performance. Furthermore, doping electrolytes or ions, for example,  $\text{P}_2\text{O}_5$ <sup>231</sup> or potassium,<sup>232</sup> may lead to considerable sensitivity improvement.

It is noteworthy that regular method for monitoring resistance change cannot detect humidity below 10% RH. To overcome this obstacle, Yadav et al.<sup>216</sup> proposed an optical method in which porous  $\text{TiO}_2$  was deposited on an isosceles glass prism to configure an optical humidity sensor. During the operation, a He–Ne laser entered the prism from one of the isosceles faces of the prism and was reflected from the glass–film interface before emerging from the other isosceles face. The emerged beam was collected through an optical fiber that connected to an optical power meter for measurement. Because of  $\text{H}_2\text{O}$  absorption by  $\text{TiO}_2$  film, light intensity was significantly influenced, indirectly reflecting the change of humidity. Obviously, film thickness was a key factor dominating the humidity detection. In their work, the detection range was expanded to 5–95%. In addition to resistive/capacitive sensors,

sensors based on magneto-elastic method were found sensitive to a humidity level of 2% RH,<sup>233</sup> whereby the change of  $\text{TiO}_2$  film (pore size 80 nm) due to water adsorption was measured.

**3.1.5. Carbon Monoxide (CO) Sensor.** CO is notoriously toxic to humans when reaching above a certain concentration as it preferentially combines with hemoglobin in human blood.<sup>234</sup> In view of this, continuous monitoring and quantification at the subppm level of CO is of vital importance.<sup>235</sup> Similar to other gases, the absorbance of CO on  $\text{TiO}_2$  would lead to resistance change in a certain range, resulting in  $\text{TiO}_2$ -based CO sensor. Table 4<sup>238–247</sup> summarizes the  $\text{TiO}_2$  nanomaterials and their performance in the detection of CO.

Seeley et al.<sup>236</sup> found that crystallinity of the  $\text{TiO}_2$  powder significantly affected CO sensing response time. Anatase phase  $\text{TiO}_2$  thick film was stable up to 900 °C. However, as calcination temperature increased from 700 to 900 °C, surface area and amorphous phase content decreased. Films calcined and sintered at 700 °C showed a lower response to CO than those calcined at 800 °C. Upon further increasing the calcination temperature, particle growth and reduced surface area slowed the sensing response. A calcination temperature of 800 °C was necessary to achieve sufficient order in the crystal structure for more efficient adsorption and desorption of oxygen ions on the surface of  $\text{TiO}_2$ .

As aforementioned, more attention was focused on nanostructured and composite  $\text{TiO}_2$  material for the sake of their better CO sensing performance.<sup>237–250</sup> Lee et al.<sup>238</sup> proposed  $\text{TiO}_2$  xerogel films for CO sensing. The film had a large porosity up to 62% and offered large surface area, thereby absorbing more CO molecules. In their work, the sensor was evaluated at 50 ppm CO and 350 °C, which gave a response time shorter than 10 s and 90 s recovery time with a sensitivity of 6.8. By adding multiwall carbon nanotubes (MWCNTs) into  $\text{TiO}_2$  xerogel films and forming a composite film,<sup>239</sup> they achieved better performance. As compared to pure  $\text{TiO}_2$  xerogel, the composite improved the sensitivity, response time, and recovery time of the sensor to 15.8, 4, and 16 s, respectively. This can be attributed to the increase of the specific surface area and the better electrical conductivity due to the n–p junction structure of  $\text{TiO}_2$  xerogel coated on MWCNTs. This result was also confirmed by Kim et al.<sup>240</sup> who reported direct-patternable  $\text{TiO}_2$  thin films containing MWCNTs. They found that there was an increase in the surface morphology and roughness of the film with MWCNTs incorporated. The sensitivity for 100 ppm CO is 89.2 with response time of 5.16 s and recovery time of 2.72 s. Park et al.<sup>242</sup> fabricated multilayered random network structure of  $\text{TiO}_2$  nanofiber by electrospinning. A response to trace CO (concentration as low as 1 ppm) at 200 °C was achieved.

Using inverse opal template method with  $\text{O}_2$  plasma treatment technology and a radio frequency sputtering process, Moon et al.<sup>243</sup> fabricated a highly sensitive gas sensor based on a network of nanostructured  $\text{TiO}_2$  hollow hemispheres (NTHH). To investigate the sensing properties, they compared response curves of three types of  $\text{TiO}_2$  gas sensors, plain  $\text{TiO}_2$  film-based,  $\text{TiO}_2$  hollow hemispheres (THH)-based (without  $\text{O}_2$  plasma treatment), and NTHH-based, with CO gas of 1–500 ppm at 250 °C as shown in Figure 13. It can be seen that the NTHH sensor exhibited much higher response than that of the other sensors. For example, it showed ~15 times higher response than the plain-film sensor. The narrow-necked morphology of NTHH facilitates the electron transport and gives CO molecules an easy access to the nanobridges in the

Table 4. Summary of the Sensing Properties of TiO<sub>2</sub> Nanomaterial-Based Gas Sensor

gas	TiO <sub>2</sub> nanostruct	fabricatn method	substrates	size (nm)	cryst struct	detectn range	opt temp (°C)	response			ref
								sensitivity <sup>a</sup>	response time	recovery time	
CO	TiO <sub>2</sub> xerogel	sol-gel	silicon wafer	G: 20–40	anatase		350	6.8 (A)	<10 s	90 s	238, 2013
	MWCNTs/TiO <sub>2</sub>	sol-gel	silicon wafer	G: 20–40	anatase		350	15.8 (A)	4 s	16 s	239, 2013
	MWCNTs/TiO <sub>2</sub>	sol-gel	glass		anatase		400	89.2 (A)	5.16 s	2.72 s	240, 2013
	Cu/TiO <sub>2</sub> nanofiber	electrospinning	ceramic tube		anatase/ rutile		300	3 (A)	4 s	8 s	241, 2010
	TiO <sub>2</sub> nanofiber	electrospinning	Pt-IDEs	D: 400–500	anatase/ rutile	from 1 ppm	200	4.4 (A)	32 s	84 s	242, 2010
TiO <sub>2</sub> hollow hemispheres		Rf sputtering/inverse opal	SiO <sub>2</sub> /Si	D: 900	anatase	1–500 ppm	250	42.25 (A)	10 s		243, 2010
	porous TiO <sub>2</sub>	microarc oxidation	Ti plate		rutile	5–100 ppm	350	1.6 (A)	200–400 s		244, 2006
	TiO <sub>2</sub> /Fe <sub>2</sub> O <sub>3</sub>	Rf sputtering	alumina	G: 20–30	anatase		300	15 (D)	~50 s		245, 2001
	TiO <sub>2</sub>	commercial powder	YSZ		anatase	10–1000 ppm	500	–41.84 (H)	<2 min		246, 2010
	Co/TiO <sub>2</sub>	sol-gel		D: 11.4	anatase	50–1000 ppm	450	5.5 (A)	<1 min		184, 2009
VOCs	Cu/TiO <sub>2</sub>	supersonic beams	alumina	D: 10.3				3.6 (A)			253, 2003
	TiO <sub>2</sub> NPs	flame spray pyrolysis	alumina		anatase/ rutile	1–7.5 ppm	500	ethanol: 20 (A) methanol: 8 (A) propanol: 14 (A) acetone: 8 (C)	2–3 s	144 s	254, 2006
	TiO <sub>2</sub> NPs	matrix-assisted pulsed laser evaporation	alumina			20–200 ppm	350	ethanol: 11 (B) acetone: 6 (B) o-xylene: 25 (A)	4 min		255, 2007
	porous-CD/TiO <sub>2</sub>	sol	quartz crystals		anatase/ rutile	>0.1	400		<1 min		256, 2005
	TiO <sub>2</sub> nanofiber	hydrothermal	AT-cut 6,000 MHz crystal		anatase		200	acetonitrile: 22.5 Hz	8–10 s		257, 2011
TiO <sub>2</sub> nanotubes		hydrothermal	alumina	D: 200	H <sub>2</sub> Ti <sub>3</sub> O <sub>7</sub> / anatase		500	toluene: 50 (A)	110–130 s	800–1150 s	258, 2011
		anodization	Ti foil	D: 150 L: 1700	anatase	10–50 ppm	RT	formaldehyde: ~37 (A)	3 min		259, 2009
	SnO <sub>2</sub> /TiO <sub>2</sub>	sol-gel	alumina		anatase	50–400 ppm	360	methanol: 60 (A) ethanol: 35 (A) formaldehyde: 55 (A) acetone: 50 (A) formaldehyde: 32 (A) dormaldehyde: 3.7 (B)	10–15 s	14–20 s	263, 2009
	Cd/SnO <sub>2</sub> /TiO <sub>2</sub>	sol-gel	GCE		anatase	100–500 ppm	320		25 s	17 s	265, 2010
	Ag/TiO <sub>2</sub>	sol-gel	alumina	D: 28–33	anatase		360		30 s	45 s	266, 2010



Table 4. continued

gas	TiO <sub>2</sub> nanostruct	fabricatn method	substrates	size (nm)	cryst struct	detectn range	opt temp (°C)	response			ref
								sensitivity <sup>a</sup>	response time	recovery time	
NH <sub>3</sub>	TiO <sub>2</sub> /Y <sub>2</sub> O <sub>3</sub>				anatase	0.026–1.30 mg/m <sup>3</sup>	195	formaldehyde:			267, 2010
	TiO <sub>2</sub> nanotubes	anodization	gold electrode	D: 100 L: 400	anatase	10–50 ppm	19	formaldehyde: 2.4 (D)	~3 min	~13 min	268, 2012
	porous TiO <sub>2</sub>	Degussa P25	alumina	D: 80	anatase	30–100 ppm	RT	formaldehyde: 1700 (D)		100 ppm	269, 2012
	TiO <sub>2</sub> nanotubes	anodization	gold electrode	D: 100 L: 400	anatase	10–50 ppm	RT	formaldehyde: 1.2 ppm <sup>-1</sup>	3 min	2.5 min	270, 2013
	ZnO/TiO <sub>2</sub>	CVD	alumina		anatase		400	ethanol: 5 (A) acetone: 22 (A)	~1 min	~1 min	271, 2007
	TiO <sub>2</sub> /SnO <sub>2</sub>	commercial powder			rutile	100–5000 ppm	400	0.5 (D)		100 ppm	272, 2012
	CSA/PANI/TiO <sub>2</sub>	sol–gel	glass		anatase/ rutile	20–100 ppm	RT	0.75 (D)	49 s	413 s	278, 2011
	PANI/TiO <sub>2</sub>			D: 90	anatase	20–140 ppm	RT	0.3 (D)	2–3 s	~60 s	279, 2010
	PANI/TiO <sub>2</sub> nanofibers	electrospinning	aluminum	D: 600	rutile	>50 ppt	RT	0.018 (D)	<10 s	<10 s	280, 2010
	PPy/TiO <sub>2</sub>	in situ polymerization			anatase	20–500 ppm	RT	0.13 (D)		100 ppm	282, 2010
NO <sub>2</sub>	CNTs/TiO <sub>2</sub>	sol–gel			anatase		RT	93 (D)	9 min	2 min	284, 2009
	TiO <sub>2</sub> NPs	DC magnetron sputtering	Si		anatase	500–1000 ppm	250	7000 (D)	90 s	110 s	285, 2007
	TiO <sub>2</sub> NPs	DC magnetron sputtering	glass		anatase	5–100 ppm	RT	7857 (100 ppm)	~34–65 s	90–115 s	286, 2013
	SnO <sub>2</sub> /TiO <sub>2</sub> nanoneedles		glass	D: 40–80 L: 60–100	anatase/ rutile		150	300% (E)	3 min	5 min	287, 2013
	PPy/TiO <sub>2</sub> /ZnO nanofibers	electrospinning		D: 100	anatase	500 ppb–450 ppm	RT	30% (F)	~15 min	~30 min	288, 2009
	TiO <sub>2</sub> /SnO <sub>2</sub>	sol			rutile	100–1000 ppm	250	3 (A)		400 ppm	289, 2011
	TiO <sub>2</sub> -PANI/PA6 nanofibers	electrospinning/ sputtering	Au			50–250 ppm	RT	18.3 (D)	<50 s	250 ppm	290, 2012
	Pd/TiO <sub>2</sub> nanofiber	electrospinning		D: 450	anatase		180	38 (B)		2.1 ppm	274, 2009
	PEDOT/TiO <sub>2</sub> nanofiber	electrospinning		D: 78	anatase	100 ppb–85 ppm	RT	1% (F)		400 ppb	291, 2007
	TiO <sub>2</sub> /carbon black	sol–gel	Au		anatase	1–100 ppm	150	7% (D)		100 ppm	292, 1993
H <sub>2</sub> S	Cr/TiO <sub>2</sub>	sol–gel	alumina		rutile		500	~1.35 (A)	<1 min	<1 min	33, 2003
	TiO <sub>2</sub> /Al <sub>2</sub> O <sub>3</sub> /Pd	sol	alumina tube		anatase	200–1000 ppm	225	0.9 (G)		1000 ppm	293, 2006

Table 4. continued

gas	TiO <sub>2</sub> nanostruct	fabricatn method	substrates	size (nm)	cryst struct	detectn range	opt temp (°C)	sensitivity <sup>a</sup>	response			ref
									response time	recovery time	conc	
	TiO <sub>2</sub> NPs	microwave-assisted sol-gel			anatase		350				1.5 ppm	295, 2007
	CdO/ZnO/TiO <sub>2</sub>	pyrolyzation	alumina tube				225–250	0.8 (D)			10 000 ppm	296, 2008

<sup>a</sup>A,  $S = R_a/R_g$ ; B,  $S = R_g/R_a$ ; C,  $S = \Delta R/R_g$ ; D,  $S = \Delta R/R_a \times 100\%$ ; E,  $S = (\Delta R/R_g) \times 100\%$ ; F,  $S = (\Delta R/R_g) \times 100\%$ ; G,  $S = \log(R_a/R_g)$ ; and H,  $S = mV/\log[\text{CO, ppm}]$ . Diameter, D; length, L; room temperature, RT.

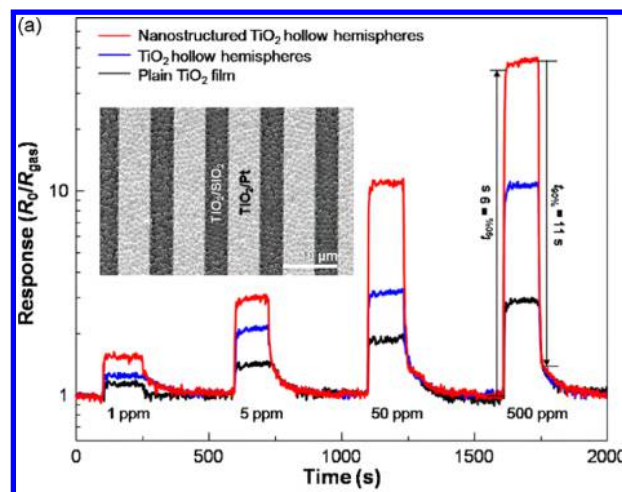


**Figure 13.** Typical response curves of gas sensors based on a plain TiO<sub>2</sub> film, TiO<sub>2</sub> hollow hemispheres (THH), and nanostructured TiO<sub>2</sub> hollow hemispheres (NTHH) to 1–500 ppm CO gases at 250 °C. The inset shows a SEM micrograph of NTHH on a Pt-IDE-patterned substrate. Reprinted with permission from ref 243. Copyright 2010 Elsevier.

NTHH sensor. However, the access of CO molecules to the short necks in the THH sensor is less favorable.

Combining TiO<sub>2</sub> with other material to form the composite is another way for enhancing the sensing performance. Comini et al.<sup>245</sup> proposed TiO<sub>2</sub>/Fe<sub>2</sub>O<sub>3</sub> composite film by reactive RF sputtering and investigated its CO sensing properties. The TiO<sub>2</sub>/Fe<sub>2</sub>O<sub>3</sub> composite film was dense and compacted with 20–30 nm TiO<sub>2</sub> grains, while the Fe<sub>2</sub>O<sub>3</sub> phase was present only at grain boundaries. The sensing response was affected by the number of Fe insets; the greater was the abundance of Fe, the higher was the response. The best results were obtained for the sample with eight insets at 300 °C, 310% for the film with eight insets of Fe, and 60% for the film with only two insets, toward 15 ppm of CO at a working temperature of 300 °C. The response and recovery time always lies between 30 and 90 s. The best sensitivity is 2.8–15 in the range of 10–1000 ppm.

### 3.1.6. Volatile Organic Compounds (VOCs) Sensor.

Volatile organic compounds (VOCs) have high vapor pressure at room temperature. Some of them are typically not acutely toxic. Instead, they have compounding chronic health effects.<sup>251</sup> Therefore, the on-site detection of VOCs becomes very important in certain environments. TiO<sub>2</sub>-based gas sensor has been developed to detect toxic VOCs including formaldehyde, methylene chloride, ethanol, hydrazine, methanol, propanol, benzene, and acetonitrile, etc. Table 4 summarizes the TiO<sub>2</sub> nanomaterials and their performance in the detection of VOCs.

The early study reported by Skubal et al.<sup>252</sup> confirmed the capability of TiO<sub>2</sub> sensor in gaseous organic detection (e.g., methylene chloride, ethanol, benzene, acetone, xylene, and isopropanol). It can be seen from Figure 14 that resistance curves clearly show a marked difference in output signal for each contaminant. Efforts have been made to fabricate TiO<sub>2</sub> matrix by various techniques, such as seeded supersonic beam,<sup>253</sup> flame spray pyrolysis,<sup>254</sup> and matrix assisted pulsed laser evaporation,<sup>255</sup> to enhance the VOCs sensors performance. The sensors made by means of these proposed techniques showed good response to ethanol, methanol, and propanol. For example, the sensor made by flame spray pyrolysis<sup>254</sup> has been used to detect acetone and ethanol at concentrations ranging

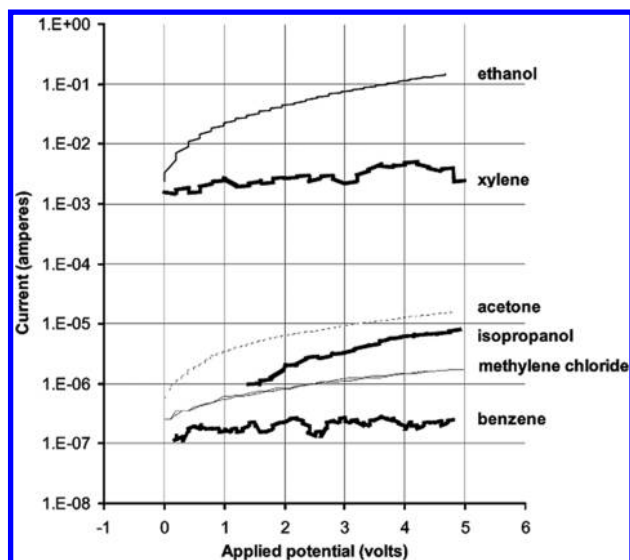


**Figure 14.** Linear sweep response of the  $\text{TiO}_2$  sensor to saturated concentrations of various compounds in an air atmosphere. Reprinted with permission from ref 252. Copyright 2002 Elsevier.

from 1 to 75 ppm at 500 °C. As reported, the response time was as short as 2–3 s for acetone and isoprene at the concentration range studied. The separated signals in Figure 14 also demonstrate a fact that specific-method-made  $\text{TiO}_2$  has a selectivity corresponding to different analyte.

Nanostructured  $\text{TiO}_2$  is widely employed thanks to its abundance of active sites for gas absorption that enhances the sensing properties.<sup>256–261</sup> For example, nanofiber-structured  $\text{TiO}_2$  was synthesized to construct gas sensor based on quartz resonators.<sup>257</sup> The sensor showed a fast response of 8–10 s and has distinct responses to different acetonitrile vapors. Seo et al.<sup>258,259</sup> proposed porous  $\text{TiO}_2$  nanotubular films-based sensor for toluene detection. As compared to commercial Degussa  $\text{TiO}_2$ , the diameter of as-prepared  $\text{TiO}_2$  nanotubes increased from 35 to 200 nm. After ball-milling treatment, the length of tubes was shortened to improve the contacts between the nanotubes. As a result, the sensor showed a sensitivity of 50 in response to 50 ppm toluene at 500 °C. In the same work, the response of ethanol and ammonia was weaker than that of toluene using the same  $\text{TiO}_2$  nanotubes, representing a certain selectivity.

Recently, most of the work focused on formaldehyde detection. Lin et al.<sup>260</sup> proposed  $\text{TiO}_2$  NTs for the formaldehyde gas sensing. In the range of 10–50 ppm, the  $\text{TiO}_2$  NTs sensor performed a remarkable sensitivity to formaldehyde gas over other reducing gas species such as ethanol and ammonia at room temperature. This is probably because of the selective property of  $\text{TiO}_2$  NTs in the detection of different VOCs gases. Similar findings were reported by Wu et al.<sup>261</sup> who used the hierarchical  $\text{TiO}_2$  nanotubes to detect formaldehyde gas under UV light illumination. In their work, the sensor's sensitivity can be enhanced by the use of UV light due to additional oxidation of formaldehyde by photogenerated holes. In addition to  $\text{TiO}_2$  nanotubes, nanoporous  $\text{TiO}_2$  nanofibers were synthesized and constructed for quartz crystal microbalance (QCM) sensors through analyses of the resonance frequency signal.<sup>262</sup> With high surface area of 68.72  $\text{m}^2/\text{g}$ , the developed formaldehyde-selective sensors exhibited rapid response and low detection limit (1 ppm) at room temperature.

In the light of the superb properties of composite materials, this kind of  $\text{TiO}_2$  sensor was introduced in VOCs detecting field and studied extensively. Zeng et al.<sup>263–265</sup> studied  $\text{SnO}_2/\text{TiO}_2$  composite-based sensor for detecting formaldehyde gas. Because of the strong electron affinity, the presence of  $\text{TiO}_2$  was favorable for the absorption of oxygen and greatly improved the electric conductivity. This kind of sensor showed sensitive responses to formaldehyde, and the response and recovery time was estimated as 10–15 and 14–20 s, respectively.<sup>263</sup> By adding Cd into  $\text{TiO}_2/\text{SnO}_2$  composite,<sup>266</sup> the maximum sensitivity of sensor was further increased to 32 with a formaldehyde gas concentration of 200 ppm at 320 °C. Meanwhile, the response and recovery time was still controlled at 25 and 17 s, respectively, because the presence of Cd also enhanced oxygen absorption by providing additional active sites. Other composites like  $\text{TiO}_2/\text{Y}_2\text{O}_3$  were also studied for the detection of formaldehyde gas.<sup>267</sup> Unlike the resistive-type sensor, the proposed sensor used chemiluminescence to detect the formaldehyde gas based on the catalytic oxidation reaction, which yields luminescent species (intermediates) and energy. As reported, the linear range was 0.026–1.30  $\text{mg}/\text{m}^3$ , and the detection limit was 0.01  $\text{mg}/\text{m}^3$ .  $\text{ZnO}/\text{TiO}_2$  composites were also made by chemical vapor deposition for the detection of VOCs.<sup>271</sup> The proposed method demonstrated that the adopted strategy was an amenable pathway to tailor the mutual  $\text{ZnO}/\text{TiO}_2$  content by simply adjusting titania deposition time. The sensor showed a good response to ethanol and acetone with a sensitivity of 5 and 22, respectively.

**3.1.7. Sensor for Other Gases.**  $\text{NH}_3$ ,  $\text{NO}_2$ , and  $\text{H}_2\text{S}$  are common gases produced in various industry processes, and their leakage will pose potential danger to working environment. Monitoring and controlling these gases is thus crucial to safety in laboratories and industrial areas. Similar to other gases mentioned previously, nanostructured and composite  $\text{TiO}_2$  materials have received increasing attention for gas detection in recent years as their performances are continuously improved. Metal oxide ( $\text{SnO}_2$ ,  $\text{WO}_3$ ,  $\text{MoO}_3$ ),<sup>272,273</sup> metal ions (Nb, Cr, Pd),<sup>274–277</sup> and other chemicals (CNTs, poly(3,4-ethylenedioxythiophene) (PEDOT), carbon black, polyaniline (PANI), polypyrrole (PPy))<sup>278–284</sup> have been incorporated with  $\text{TiO}_2$  for detecting these gases. Table 4 summarizes the  $\text{TiO}_2$  nanomaterials and their performance in the detection of  $\text{NH}_3$ ,  $\text{NO}_2$ , and  $\text{H}_2\text{S}$ , respectively.

Gong et al.<sup>280</sup> reported ultrasensitive  $\text{NH}_3$  gas sensor from PANi nanograins encased  $\text{TiO}_2$  fibers. Specifically, nanograins of a p-type conductive polymer, PANi, were encased on an electrospun n-type semiconductive  $\text{TiO}_2$  fiber surface. The resistance of the p–n heterojunctions combining with the bulk resistance of PANi nanograins functioned as electric current switches when  $\text{NH}_3$  gas was absorbed by PANi nanoparticles. The sensitivities were about 0.018, 0.009, and 0.004 for 200, 100, and 50 ppt of  $\text{NH}_3$  gas, respectively. Inversely using PANi fibers with  $\text{TiO}_2$  nanoparticles, Tai et al.<sup>281</sup> obtained a fast response of 2–3 s in the  $\text{NH}_3$  gas concentration range of 20–140 ppm and a detection limit as low as 1 ppm at room temperature. The PPy/ $\text{TiO}_2$  composite thin films also exhibited a low detection limit of 2 ppm of  $\text{NH}_3$  gas as reported by Wu et al.<sup>282</sup>

Moon et al.<sup>277</sup> loaded Pb into the  $\text{TiO}_2$  nanofibers and developed a highly sensitive  $\text{NO}_2$  sensor, which exhibited remarkably stable responses to  $\text{NO}_2$  gas of concentration as low as 0.16 ppm at 180 °C. Another valuable polymer material is PEDOT that possesses high conductivity and optical trans-



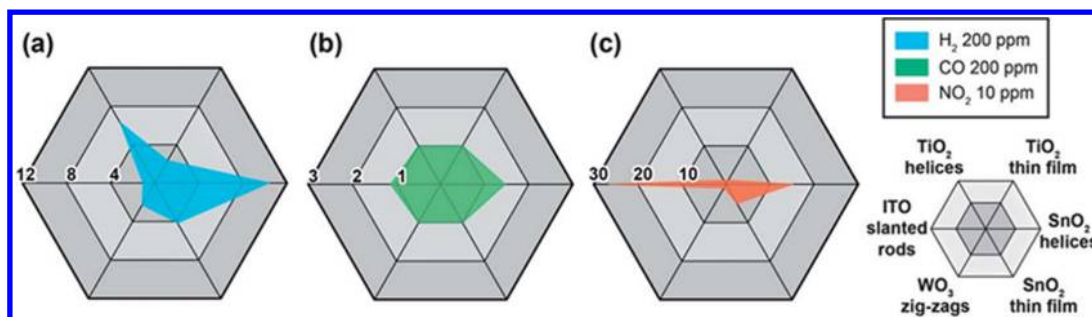


**Figure 15.** Radar chart patterns of the prototype e-nose chip for (a)  $\text{H}_2$  200 ppm, (b)  $\text{CO}$  200 ppm, and (c)  $\text{NO}_2$  10 ppm. Each vertex of the radar corresponds to each sensor of the array, where the devices were measured at  $150^\circ\text{C}$  with 0.2 V applied bias. Reprinted with permission from ref 298. Copyright 2013 Elsevier.

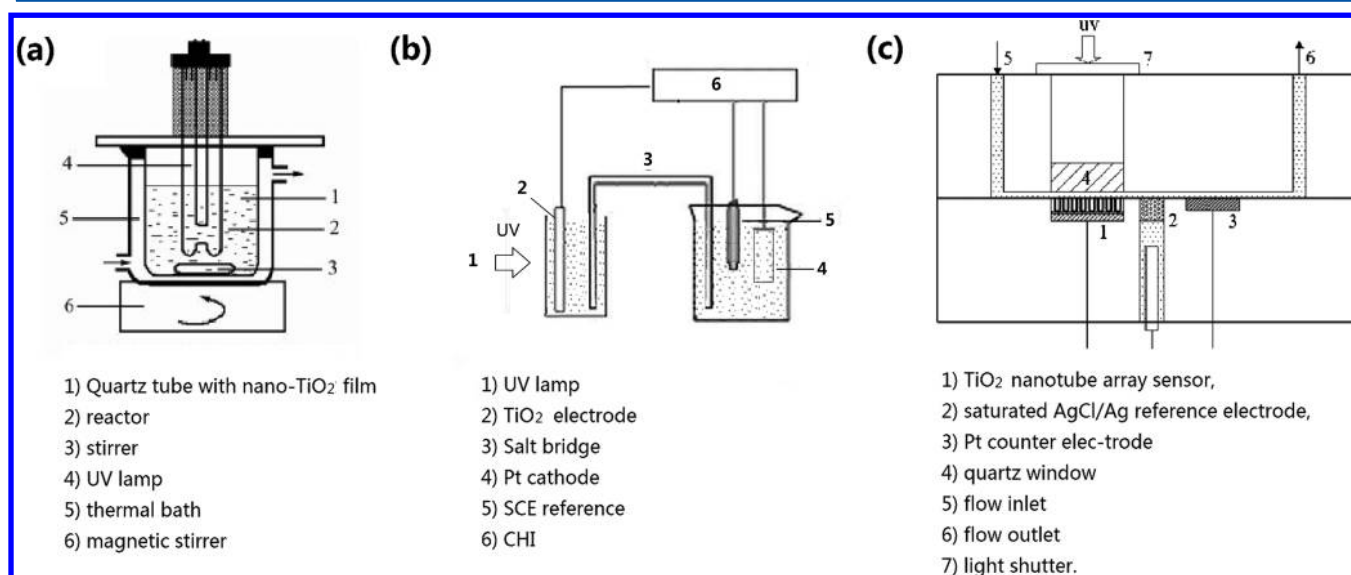


**Figure 16.** Schematic depiction of different COD sensors: (a) Photocatalytic bulk sensor. Reprinted with permission from ref 299. Copyright 2007 Elsevier. (b) Photoelectrocatalytic bulk sensor. Original drawing was done by us. (c) Photoelectrocatalytic thin-cell sensor. Reprinted with permission from ref 311. Copyright 2008 Wiley-VCH.

parency in its doped state, low band gap, and moderate redox potential. When coupling PEDOT with  $\text{TiO}_2$  nanofibers, Wang et al.<sup>274</sup> further lowered the detection limit to 7 ppb at a signal-to-noise ratio of 3. In addition to polymer, Cr doped  $\text{TiO}_2$  composite was studied by Ruiz<sup>275</sup> and Li,<sup>276</sup> and they found that the addition of Cr suggests a tendency for the electronic conduction to alter from n- to p-type. The result indicates that the 10% (atomic percentage) Cr-doped thin film calcined at  $600^\circ\text{C}$  exhibits a promising sensing capability to  $\text{NO}_2$ .<sup>275</sup>

So far, although research to explore  $\text{H}_2\text{S}$  sensors using  $\text{TiO}_2$  is relatively few, some efforts nevertheless have been made.<sup>293–297</sup> Chaudhari et al.<sup>293</sup> proposed  $\text{TiO}_2/\text{Al}_2\text{O}_3/\text{Pd}$  composite electrode for  $\text{H}_2\text{S}$  sensing. As compared to undoped  $\text{TiO}_2$ , the addition of aluminum enhanced the sensitivity possibly due to the introduction of electronic states at the surface or into the bulk that modifies base material. Further incorporation of palladium lowered the required operating temperature from  $250$  to  $225^\circ\text{C}$ , and increased the  $\text{H}_2\text{S}$  gas sensing performance in its concentration range of  $200$ – $1000$  ppm at  $225^\circ\text{C}$ . Another  $\text{TiO}_2$ -based material for  $\text{H}_2\text{S}$  sensing was introduced by Topalian et al.<sup>295</sup> who detected low concentrations of  $\text{H}_2\text{S}$  by noise spectroscopy when the gas sensor was irradiated by UV light. In their work, a prominent change in resistance noise level was achieved as the irradiated

film was exposed to  $1.5$  ppm of  $\text{H}_2\text{S}$ , while no change was observed in the absence of UV. This effect was possibly due to decomposition of the adsorbed gas via photocatalysis induced by  $\text{TiO}_2$ , or due to decreased potential barrier between the charged grains.

**3.1.8. Brief Summary.** As is known,  $\text{TiO}_2$  gas sensor responds to many types of gases based on the resistance change, ensuring a wide application range. However, most of the gas sensors have to face a low selectivity. The main problem results from the fact that a single sensor cannot distinguish different analyte and the response is easily influenced by the presence of other gases, although the response to a single gas could be much different. Because of this, most studies only investigated the target analyte in a simple matrix instead of complex matrixes and real samples. A feasible solution is to use an “electronic nose”, which combines several sensors and several transducers in multielement modular sensor systems. Upon exposure to a vapor, the sensors create a pattern across the array. The pattern of distributed response may be identified and quantified using a software analysis program such as pattern recognition and/or neural network or principal component analysis. For example, Hwang et al.<sup>298</sup> integrated six gas sensors made of various metal oxides ( $\text{TiO}_2$ , indium tin oxide (ITO),  $\text{SnO}_2$ , and  $\text{WO}_3$ ) into a single e-nose chip by

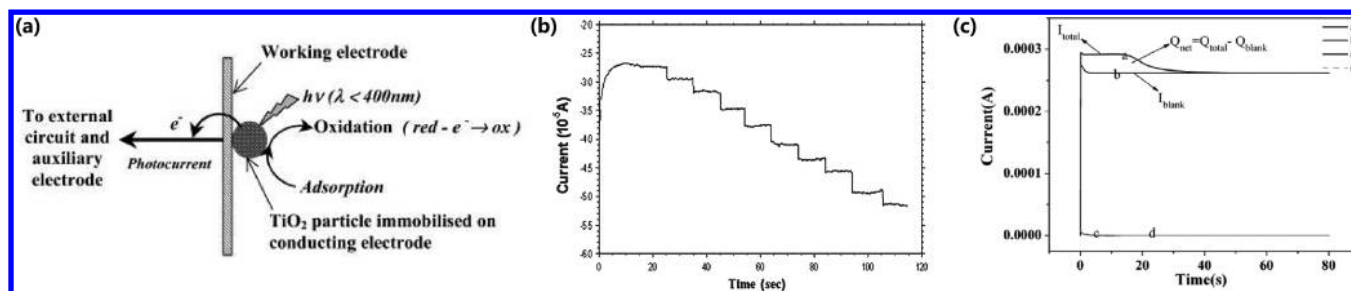


**Figure 17.** Photocurrent tracing-based COD measuring principle: (a) Schematic of the photoelectrocatalytic processes involved in the analytical signal generation. Reprinted with permission from ref 308. Copyright 2004 American Chemical Society. (b) Current responses to the successive addition of organics. Reprinted with permission from ref 310. Copyright 2006 Wiley-VCH. (c) Photocurrent response of electrolyte solution (solid line) in a thin-cell reactor along with the photocurrent response of the electrolyte containing organic compounds (dashed line). Reprinted with permission from ref 312. Copyright 2012 Royal Society of Chemistry.

using conventional microelectronic processes. As shown in Figure 15, each gas sensor in the e-nose has its specific sensitivity pattern for different gas molecules (H<sub>2</sub>, CO, NO<sub>2</sub>), thus empowered to discriminate various gas species. Using the similar strategy, Taurino et al.<sup>253</sup> realized the discrimination of complex VOCs (ethanol, methanol, and propanol) in a gas sensor array, which consists of a different TiO<sub>2</sub> gas sensor device, prepared by using different deposition parameters.

As compared to selectivity, the sensitivity of a gas sensor is the major concern in most research in this field. As previously discussed, the sensitivity as well as the range, the dynamic response of a gas sensor can be improved significantly when nanostructured TiO<sub>2</sub> is employed, which presents apparent advantages: a larger surface-to-volume ratio and a grain size (few nanometers) comparable to the depth of the space-charge layer that surrounds the nanograin. Therefore, the newly developed nanostructured TiO<sub>2</sub> could be the potential candidate for a highly sensitive gas sensor. In other ways, modification with noble metals (e.g., Pt, Pd, Au, or Ag) could effectively improve the interaction between TiO<sub>2</sub> surface and gas molecules, thereby reducing the operation temperature; introducing other chemicals (semiconductors, polymers) that could enhance gas absorption or electron transfer so as to improve the sensitivity.

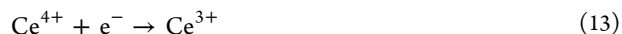
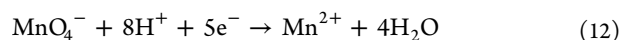
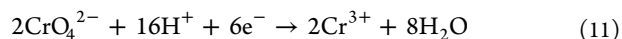
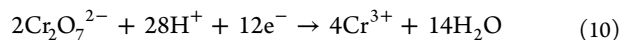
Therefore, a gas sensor with both high sensitivity and selectivity is the combination of all feasible technologies.

### 3.2. COD Sensor

**3.2.1. Measurement Principle.** **3.2.1.1. Chemical Tracing.** For a TiO<sub>2</sub>-based COD sensor, the amounts of organic compounds, dissolved oxygen, and metal ions changed during the oxidation and reduction by photoholes and photoelectrons. Thus, they can be traced and used for COD determination. The sensor is mainly composed of a bulk photocatalytic reactor shown in Figure 16a, in which TiO<sub>2</sub> photocatalyst is dispersed in the solution to degrade the organics when being accompanied by UV lamp illumination.<sup>299</sup>

**3.2.1.1.1. Dissolved Oxygen.** TiO<sub>2</sub> photocatalysis leads to stoichiometric photomineralization of organic compounds where oxygen acts as a photo-generated electron acceptor and plays an essential role in degrading organic compounds to CO<sub>2</sub> through the formation of a superoxide radical ion.<sup>300–302</sup> Accordingly, the concentration of dissolved oxygen before and after photo oxidation process is well in accordance with the change of organic compound and can be calculated to deduce the value of COD according to eq 7.

**3.2.1.1.2. Metal Ions.** In aqueous system, dissolved metal ions, such as dichromate ions (Cr<sub>2</sub>O<sub>7</sub><sup>2-</sup>),<sup>303–305</sup> cerium ions (Ce<sup>4+</sup>),<sup>306</sup> and permanganate (MnO<sub>4</sub><sup>-</sup>),<sup>307</sup> can be reduced, and their concentration changes can be detected. During the photocatalysis process, metal ions stoichiometrically accept the photoelectrons at the conduction band, which enhances the photocatalytic degradation of organic compounds. Meanwhile, metal ions could be reduced from high valence to low valence as shown by eqs 10–13. Therefore, when metal ions are present, the COD value of a given sample could be assessed by tracing the change of metal ions concentration through using a spectrophotometer.



**3.2.1.2. Photocurrent Tracing.** Although the substance change in the sample solution can be used to determine COD, some problems, such as low dissolved oxygen and toxic chemical reagent (e.g., Cr<sub>2</sub>O<sub>7</sub><sup>2-</sup>), could still hinder the application of the sensor. As a result, another COD sensing principle was introduced to indicate sample COD by measuring photocurrent rather than dissolved substances during photo oxidation of organics. This principle is built based on the fact that the photocurrent generated during photocatalytic degradation of organic matters is proportional to the substrate concentration. Recall that when TiO<sub>2</sub> photoelectrode, a component of the three-electrode system, was illuminated under UV light, the photoholes and photoelectrons will participate in redox reactions with the substances present in the solution, and that the decomposed substances will release electrons that were transferred to the TiO<sub>2</sub> photoelectrode (see Figure 17a).<sup>308</sup> Photocurrent will increase when concentrations of organic substances increase. On the basis of this principle, two types of sensing methodologies were developed for COD determination.

**3.2.1.2.1. Direct Photocurrent Measurement.** The sensing is conducted in a three-electrode system with an external light source as shown in Figure 16b. For measuring COD, an electrochemical workstation is used to capture the photocurrent. As is described above, photocurrent increases with the increase of substances concentration (see Figure 17b), and

Table 5. Summary of the Sensing Properties of TiO<sub>2</sub> Nanomaterial-Based COD Sensor<sup>a</sup>

TiO <sub>2</sub> nanostructure	fabrication method	substrates	size	crystal structure	device	tracing elements	detection range	detection limit	ref
TiO <sub>2</sub> NPs	commercial TiO <sub>2</sub>	PTFE		anatase	bulk reactor	dissolved O <sub>2</sub>	0–4.7 ppm	0.25 ppm	300, 2000
TiO <sub>2</sub> beads	commercial TiO <sub>2</sub>			anatase	bulk reactor (FIA)	dissolved O <sub>2</sub>	0.69–4.83 ppm	0.12 ppm	302, 2001
TiO <sub>2</sub> NPs	Degussa P25			anatase	bulk reactor	Cr <sup>6+</sup>	0.1–280 mg L <sup>-1</sup>	0.02 mg L <sup>-1</sup>	303, 2004
TiO <sub>2</sub> NPs	sol–gel	quartz tube		anatase	bulk reactor	Cr <sup>6+</sup>	20–500 mg L <sup>-1</sup>	20 mg L <sup>-1</sup>	304, 2006
TiO <sub>2</sub> /sieve 4A	Degussa P25		D: 20 nm	anatase	bulk reactor	Cr <sup>6+</sup>	3–15 mg L <sup>-1</sup>	0.24 mg L <sup>-1</sup>	305, 2011
TiO <sub>2</sub> NPs	sol–gel	quartz tube		anatase	bulk reactor	Ce <sup>4+</sup>	1–600 mg L <sup>-1</sup>	0.5 mg L <sup>-1</sup>	306, 2005
ZnO/TiO <sub>2</sub>	sol–gel	quartz tube		anatase	bulk reactor	Mn <sup>6+</sup>	0.3–10.0 mg L <sup>-1</sup>	0.1 mg L <sup>-1</sup>	307, 2007
TiO <sub>2</sub> /SnO <sub>2</sub> /sb	sol–gel	glass		anatase	bulk reactor (FIA)	photocurrent (A)	0.5–235 mg L <sup>-1</sup>	0.3 mg L <sup>-1</sup>	310, 2006
TiO <sub>2</sub> NTs	anodization	Ti foil	D, 100 nm; L, 350 nm	anatase	thin layer reactor (FIA)	photocurrent (B)	0–500 mg L <sup>-1</sup>	1 mg L <sup>-1</sup>	313, 2013
TiO <sub>2</sub> NTs	anodization	Ti foil	D: 30–70 nm	anatase	bulk reactor	photocurrent (A)	20–800 mg L <sup>-1</sup>	10 mg L <sup>-1</sup>	309, 2006
Ti/TiO <sub>2</sub>	sol–gel	Ti		anatase	bulk reactor	photocurrent (A)	50–2000 mg L <sup>-1</sup>	16 mg L <sup>-1</sup>	316, 2006
Ti/TiO <sub>2</sub> /PbO <sub>2</sub>	sol–gel	Ti rod		anatase	bulk reactor (FIA)	photocurrent (A)	30.0–2500.0 mg L <sup>-1</sup>	15 mg L <sup>-1</sup>	317, 2007
Ti/TiO <sub>2</sub>	sol–gel	Ti		anatase	bulk reactor (FIA)	photocurrent (A)	50.0–1000.0 mg L <sup>-1</sup>	15 mg L <sup>-1</sup>	318, 2007
Au/TiO <sub>2</sub> NTs	anodization	Ti foil		anatase	bulk reactor	photocurrent (A)	1–800 mg L <sup>-1</sup>	0.3 mg L <sup>-1</sup>	319, 2008
TiO <sub>2</sub> NPs	sol–gel	ITO	T: 1 μm	anatase	thin layer reactor	photocurrent (B)	0–200 mg L <sup>-1</sup>	0.2 mg L <sup>-1</sup>	320, 2004
TiO <sub>2</sub> NPs	sol–gel	ITO	T: 1 μm	anatase	thin layer reactor	photocurrent (B)	0–360 ppm	0.2 ppm	321, 2004
TiO <sub>2</sub> NPs	sol–gel	ITO		anatase	thin layer reactor	photocurrent (B)	1–100 mg L <sup>-1</sup>	0.1 ppm	322, 2006
TiO <sub>2</sub> NPs	sol–gel	ITO		anatase		photocurrent (B)	0–120 mg L <sup>-1</sup>	0.2 mg L <sup>-1</sup>	323, 2009
TiO <sub>2</sub> nanofiber	hydrothermal	Ti foil	D: 20 nm	anatase	thin layer reactor	photocurrent (B)	0–250 mg L <sup>-1</sup>	0.95 mg L <sup>-1</sup>	324, 2011
LBL TiO <sub>2</sub> NPs	sol	FTO	D: 4 nm	anatase	bulk reactor	photocurrent (B)	0–130 mg L <sup>-1</sup>	1 mg L <sup>-1</sup>	325, 2012
TiO <sub>2</sub> nanorods	hydrothermal	FTO	D: 50 nm	rutile	bulk reactor	photocurrent (B)	20–280 mg L <sup>-1</sup>	18.3 mg L <sup>-1</sup>	326, 2013
TiO <sub>2</sub> NTs	anodization	Ti foil	D, 100 nm; L, 350 nm	anatase	thin layer reactor	photocurrent (B)	0–850 mg L <sup>-1</sup>		327, 2009
TiO <sub>2</sub> NPs	sol–gel	BDD	D: 10–20 nm	anatase/rutile	bulk reactor	photocurrent (B)	0–300 mg L <sup>-1</sup>	0.12 mg L <sup>-1</sup>	328, 2011
Pt/TiO <sub>2</sub> NTs	anodization	Ti foil	D: 90 nm	anatase	bulk reactor	photocurrent (A)		9.5 mg L <sup>-1</sup>	329, 2011
Cu <sub>2</sub> O/TiO <sub>2</sub> NTs	anodization	Ti foil		anatase	bulk reactor	photocurrent (B)	20–300 mg L <sup>-1</sup>	15 mg L <sup>-1</sup>	330, 2013

<sup>a</sup>A, direct photocurrent model; B, exhaustive degradation model; flow injection analysis, FIA; thickness, T.

linear correlation between known COD values and the photocurrents generated was studied.<sup>310</sup>

**3.2.1.2.2. Exhaustive Degradation Model.** This method is established on the basis of a thin layer reactor shown in Figure 16c.<sup>311</sup> Besides a typical three-electrode system and an external light source, the reactor cell volume is designed to be very small, usually less than 8 μL.<sup>311</sup> A set of typical photocurrent–time profiles obtained from exhaustive degradation of organics is shown in Figure 17c.<sup>312</sup> The photocurrent ( $i_{\text{background}}$ ) observed for the blank solution (solid line) originated from the oxidation of water by the illuminated TiO<sub>2</sub> electrode. Photocurrent ( $i_{\text{total}}$ ) observed in the organic solution is the summation of two components (dash line), one from the oxidation of organics and the other from the oxidation of water.

The decay of  $i_{\text{total}}$  to the  $i_{\text{background}}$  level implies that all of the organics have been oxidized at that point. The net charge,  $Q_{\text{net}}$ , that originated from the photoelectrochemical oxidation of the organics can be used to quantify the COD value of the target sample according to Faraday's law. In this monitoring model, a thin layer reactor was employed in the photoelectrochemical oxidation so as to cut down the reaction time and make the exhaustive degradation of organics much easier.<sup>313</sup> This is feasible for the realization of fast monitoring of COD.

According to different photocatalytic oxidative methods, TiO<sub>2</sub> COD sensors can be further classified into two types in general: one is photocatalytic COD sensor based on chemical tracing, and the other is photoelectrocatalytic COD sensor based on photocurrent tracing. Table 5 summarizes the sensing



materials, technology, and performance of the TiO<sub>2</sub> COD sensors developed in recent years.

**3.2.2. TiO<sub>2</sub>-Based Photocatalytic COD Sensor.** The TiO<sub>2</sub>-based photocatalytic COD sensing method was first developed by Karube's group<sup>300</sup> in 2000. They used TiO<sub>2</sub> NPs to photocatalytically degrade organic compound and determine the COD value by measuring the change of dissolved oxygen in water. The sensing performance was evaluated through using both synthesized water samples and authentic water samples from lakes in Japan. The response time of the sensor was approximately 3 ± 4 min with a detection limit of 0.118 ppm. Later, they improved this concept by constructing a COD probe that was made by attaching TiO<sub>2</sub> fine particles that had adsorbed polytetrafluoroethylene (PTFE) membrane to the tip of an oxygen probe.<sup>302</sup> This method achieved a slight increase in the linear range of ca. 20 ppm and was considered to be reliable, in that the observed parameter was close to the theoretical COD value. In addition, the sensor also showed a long-term stability (RSD 5.7%, 30 days). However, its narrow linear range caused by the low oxidation percentage and inadequate sensitivity of the oxygen probe was its major drawback. The problem of low oxidation percentage was typically caused by insufficient photocatalytic activity, light intensity, and low O<sub>2</sub> solubility in water solution. This problem restricted its application in less contaminated water,<sup>295</sup> and made it inapplicable even when dealing with severely contaminated industrial wastewater.

To overcome the drawbacks mentioned above, other electron acceptors with higher oxidative capability were proposed, among which dichromate ions (Cr<sub>2</sub>O<sub>7</sub><sup>2-</sup>),<sup>303–305</sup> cerium ions (Ce<sup>4+</sup>),<sup>306</sup> and permanganate ions (K<sub>2</sub>MnO<sub>4</sub>)<sup>307,308</sup> drew much attention. Jin's group<sup>304</sup> reported a nano-TiO<sub>2</sub>-K<sub>2</sub>Cr<sub>2</sub>O<sub>7</sub> system in which TiO<sub>2</sub>-coated quartz tube was used as photocatalyst. The optimized operation conditions were studied by using glucose as a standard substance. The detecting range was 20–500 mg L<sup>-1</sup>, and the detection limit was 20 mg L<sup>-1</sup>. Ce<sup>4+</sup><sup>306</sup> was also proposed and used for determining the COD values of water samples. Accordingly, the determination was achieved by direct measurement of the change of Ce<sup>4+</sup> concentration. Under optimal conditions, a good calibration curve for COD values between 1.0 and 12 mg L<sup>-1</sup> was obtained, and the detection limit was as low as 0.4 mg L<sup>-1</sup>. When authentic water samples were tested, the results were in good agreement with those acquired from conventional methods. It showed that the fluorescence intensity change was linear with COD concentration in the range of 0–100.0 mg L<sup>-1</sup> with a detection limit of 0.9 mg L<sup>-1</sup>. Later, Jin's group further reported the application of a nano-ZnO/TiO<sub>2</sub> composite film coated on the quartz support as photocatalyst to improve the separate efficiency of the charges and extend the range of light absorption spectrum.<sup>307</sup> Photometric method was adopted for determination of the Mn(VII) concentration. Under the optimal operation conditions, the detection limit of 0.1 mg L<sup>-1</sup> and COD values with the linear range of 0.3–10.0 mg L<sup>-1</sup> were achieved.

The above studies were accomplished in TiO<sub>2</sub>-based photocatalytical systems, in which the target organics were degraded either by suspended TiO<sub>2</sub> nanoparticles in solution or by immobilized TiO<sub>2</sub> thin film attached on nonconductive substrate. However, in a photocatalytic system, the main drawback in practical applications is the easy recombination of the photogenerated electron/hole pairs, which seriously affects the photocatalytical efficiencies and reduces the range of the

COD values that can be detected. Although little work has involved nanostructured TiO<sub>2</sub> in a PC-based COD sensing, undoubtedly, using nanostructured TiO<sub>2</sub> can improve photocatalytical efficiencies. For instance, it was reported that TiO<sub>2</sub> NTs show higher efficiency than TiO<sub>2</sub> NPs during a PC process;<sup>314</sup> however, the efficiency is still far below that obtained in a PEC process.<sup>315</sup> Moreover, because the test relies on measurement of chemical concentrations in aqueous samples, it is hard to carry out a continuous test. Therefore, if either detection range or efficiency is taken into consideration, photocatalytic-based TiO<sub>2</sub> COD sensor cannot meet the requirement of authentic application.

**3.2.3. Photoelectrocatalytic-Based TiO<sub>2</sub> COD Sensor.** Because of the inadequate application of photocatalytic-based TiO<sub>2</sub> COD sensor in COD measurement, this type of sensor gradually earns widespread attention. Studies showed that the fixation of TiO<sub>2</sub> onto a conductive substrate and the application of electric field (i.e., potential bias) on the TiO<sub>2</sub> can be used to tackle the aforementioned problems of the traditional photocatalysis systems, that is, separation of TiO<sub>2</sub> nanomaterials from reaction media and recombination of photoelectrons and photoholes. Application of an electric field is an effective tool to separate the photoholes and photoelectrons, which improves the photocatalytic efficiency. Another advantage is that the electrons could appear in the form of current, which can be recorded by an electrochemical workstation. This workstation will provide a new way of measuring COD by means of current variation.

Using TiO<sub>2</sub> electrode, Jin et al.<sup>309,310,316–319</sup> established direct photocurrent measurement method by detecting the charge change in a circuit to measure the COD value. The main advantages of the method proposed were its ease to manipulate, short response time, lower cost, and low environmental impact. In the case of TiO<sub>2</sub>/Ti electrode, under the optimized conditions, the sensor responded linearly to the COD of D-glucose solution within the range of 50–2000 mg L<sup>-1</sup> with a detection limit of 16 mg L<sup>-1</sup>.<sup>310</sup> When using Au doped TiO<sub>2</sub> nanotube arrays electrode, a much lower detection limit of 0.3 mg L<sup>-1</sup> was achieved.<sup>319</sup>

Zhao's group<sup>320–323</sup> proposed another method, called "exhaustive degradation model", for the determination of COD. As introduced earlier, the COD value can be obtained by measuring the current variation in association with the organic concentrations during the photoelectrocatalytic process. They also developed a thin layer reactor that employs a three-electrode system to detect the current with an electrochemical analyzer. Under the optimized experimental conditions, the practical detection limit of 0.2 mg L<sup>-1</sup> COD with the linear range of 0–200 mg L<sup>-1</sup> was achieved.<sup>320</sup> The results demonstrated that the measured COD values were in excellent agreement with the results obtained by using standard methods. As compared to the previously used methods, this method is environmentally friendly, robust, rapid, and easily automated. For example, it only requires 1–5 min to complete an assay and consumes very limited reagent (electrolyte only). On the basis of its working mechanism (introduced in section 3.2.1.2), a thin layer reactor is its main characteristic. Because the catalytic efficiency of TiO<sub>2</sub> is low in practice, an extremely small reactor volume ensures that the reaction is completed within a relatively short period of time and organic compounds are completely oxidized. Meanwhile, complete oxidation guarantees precise determination of organic pollutants concentrations and thus outperforms other traditional methods. On the basis of the



above technique, thin-layer photocatalytic COD sensors could be quickly commercialized.

On the basis of the exhaustive oxidation model, one of the further modifications is to increase the electrode catalytic efficiency to shorten the detection time. Different from  $\text{TiO}_2$  nanoparticle-based thin films, other nanostructured  $\text{TiO}_2$  can provide larger surface area, better electron transfer efficiencies, and, ultimately, higher photoelectrocatalytic efficiencies.<sup>324–334</sup> Mu et al.<sup>324</sup> reported a  $\text{TiO}_2$  nanofiber film that when coated on ITO glass, integrated the  $\text{TiO}_2$  electrode into a thin-cell photoelectrocatalytic reactor for rapid determination of COD in wastewater samples. The  $\text{TiO}_2$  nanofiber film improved the charge separation, transport, and diffusion of organics into nanofiber films, thereby accelerating the photoelectrocatalytic degradation process. In their work, a determination limit of  $0.95 \text{ mg L}^{-1}$  COD with a working range of  $0\text{--}250 \text{ mg L}^{-1}$  was achieved. Similarly, other nanostructured  $\text{TiO}_2$  materials assembled on TCO substrate were also reported.<sup>325,326</sup>

Different from the  $\text{TiO}_2$ /TCO glass electrode, Zhou's group<sup>311–313,327</sup> fabricated highly ordered  $\text{TiO}_2$  NTs via direct anodization of Ti sheet. The  $\text{TiO}_2$  NTs electrode is highly ordered, of high aspect-ratio structures, with nanocrystalline walls perpendicular to electrically conductive Ti substrates; it is thereby well suited for the efficient separation of photo-generated holes so as to yield higher photocatalytic activity than coated  $\text{TiO}_2$  nanofilm electrode.<sup>320</sup> By applying the  $\text{TiO}_2$  electrode in a thin-cell reactor with an exhaustive oxidation model, a wider dynamic working range of  $0\text{--}850 \text{ mg L}^{-1}$  for the COD determination was achieved.<sup>311</sup> Moreover, the  $\text{TiO}_2$  NTs sensors exhibit good accuracy, stability, and reproducibility. Figure 18 shows the COD determination achieved by using a  $\text{TiO}_2$  NTs sensor for various chemicals.

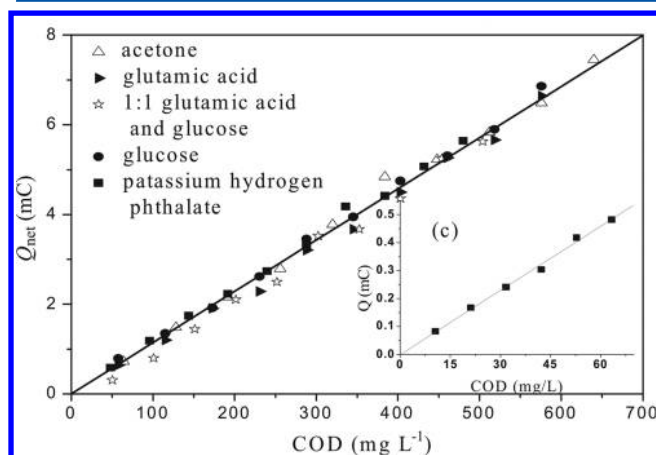


**Figure 18.** COD determination by using  $\text{TiO}_2$  NTs: (a) quantitative relationship between  $Q_{\text{net}}$  and the concentration of organic compounds; (b) quantitative relationship between  $Q_{\text{net}}$  and COD; and (c) correlation between  $Q_{\text{net}}$  and COD at low concentrations of organics. Reprinted with permission from ref 311. Copyright 2008 Wiley-VCH.

It should be noted that, although  $\text{TiO}_2$  possesses good oxidizing capacity, it fails to completely oxidize benzenoid and nitrogen containing organic compounds, which hinders precise determinations of organic pollutants. To analyze the degradation process on the part of different types of organic compounds, Chen et al.<sup>312</sup> using the Langmuir adsorption equation analyzed the adsorption and degradation process of

fructose, benzoic acid, glutamic acid, fumaric acid, and nicotinic acid on  $\text{TiO}_2$  nanotube array electrodes. The following equations were acquired:

$$I_{\text{oph}} = \frac{a \times KC_0}{1 + KC_0} + b \quad (14)$$

where  $I_{\text{oph}}$  is the initial instant photocurrent,  $a$  is constant,  $b$  is the photocurrent generated from substrates degradation, and  $K$  is the adsorption constant on  $\text{TiO}_2$  NTs surface.

The results showed that all five types of organics followed Langmuir isothermal adsorption equation. Put differently, the adsorptions were all monolayer adsorptions, and the  $b$  values were very close to each other. This proved that the thin-layer reactor possessed good stability and reproducibility. It was found that the adsorptive capacity of the five compounds on  $\text{TiO}_2$  NTs surface all directly affected the reaction rate, and their adsorptions were the rate-determining steps. In addition, for the refractory organics (niacin, glutamic acid, and benzoic acid), their resistances toward degradation also partly affected the reaction rates, resulting in significantly longer reaction time than that of easily degradable organic. One possible reason lies in the absence of extractable C–H bonds in the refractory organics, which makes  $\cdot\text{OH}$  attack focus on the  $\text{NH}_2$  moiety.<sup>32</sup> This attack, as the major reaction pathway, is very slow, and determines the slow degradation rate.

Apparently, the presence of refractory organics decreased the possibility of acquiring precise COD values. Therefore, in an attempt to enhance the oxidizing capability of refractory organics, Zhao et al.<sup>333</sup> proposed the synergetic photoelectrocatalytic oxidation effect in thin-layer system. The study focused on nitrogenous organic compounds (NOCs) that are persistent compounds that cannot be completely oxidized even in the most oxidative chemical environments. An inadequate oxidation of the chemical will lead to a lower COD value. In this study, glucose was added to the test sample prior to the COD measurement. Results showed the oxidation percentages of the NOCs were increased by up to 100% when a sufficient amount of glucose was added to the NOC samples, which led to precise COD value. The reaction mechanism was investigated by Zhao et al.<sup>333</sup> It proved that the glucose was oxidized to organic hydroxyl radicals ( $\text{R}\cdot\text{OH}$ ), reacted with NOCs adsorbed on  $\text{TiO}_2$  NTs surface, and easily formed degradable  $\text{HO}\cdot\text{R}\cdot\text{R}'\text{--COOH}$ . This process enhanced the oxidation of NOCs and ultimately achieved 100% degradation.

**3.2.4. Online  $\text{TiO}_2$  COD Sensor.** The growing needs for on-site, real-time monitoring and control of environmental and industrial processes have rose in the past decades. In fact, online analytical systems have several advantages over other monitoring systems, such as easy automation, low cost, short analysis time, high reproducibility, and unmanned operation. On the basis of these, online COD sensor catalyzed by  $\text{TiO}_2$  electrode is of great attraction. For the purpose, a proper technique is flow injection analysis, which was developed in 1975 by Ruzicka and Hansen.<sup>334</sup>

Kim et al.<sup>302,335</sup> proposed a flow injection system that involves the use of a  $\text{TiO}_2$  beads-based sensor. The sensor was developed in conjunction with  $\text{TiO}_2$  beads in the photochemical column and an oxygen electrode as the sensing part (see Figure 19). They investigated the operational conditions for the determination of COD in a flow injection analysis (FIA) system that includes the sample volume, flow rate, and the amount of  $\text{TiO}_2$ . It was found that, by increasing the reactor

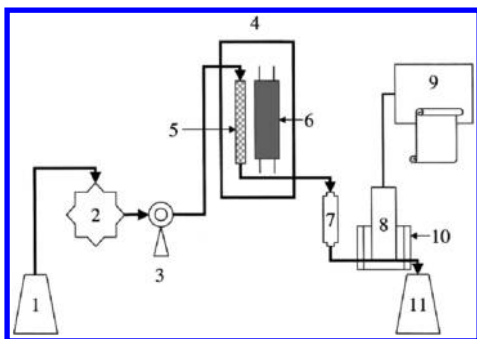


**Figure 19.** Schematic diagram of the apparatus: 1, deionized water supply; 2, pump; 3, injector; 4, reflector; 5, photochemical column consisting of  $\text{TiO}_2$  beads; 6, UV lamp; 7, air damper; 8, oxygen electrode; 9, integrator; 10, thermostatic water bath; 11, waste tank. Reprinted with permission from ref 302. Copyright 2001 Elsevier.

volume and flow rate, the sensitivity could be improved until it reached the maximum. Increasing the amount of  $\text{TiO}_2$  facilitated a better contact between  $\text{TiO}_2$  beads and substrates and increased the oxidation reaction. However, too many  $\text{TiO}_2$  beads could decrease the flow speed and lower the sensitivity. Besides, online system could easily suffer from insufficient photocatalytic activity and low  $\text{O}_2$  solubility in water solution and could lead to low precision and narrow detection range.

The proposal of exhaustive degradation model<sup>312</sup> and the design of thin-layer photoelectrocatalytic reactor provided the highly effective online COD analysis system with better theoretical and technical support. By applying the above methodology to the online technique, Li et al.<sup>313</sup> developed an online COD sensing system consisting of flow injection technology and online analysis system. In a flow injection process (see Figure 20a), the carrier (electrolyte) kept flowing

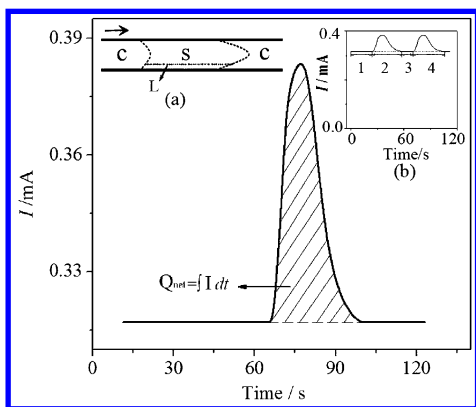


**Figure 20.** Schematic diagram of typical response photocurrent signals in flow injection analysis. The inserted Figure 16a shows the sample state under flow injection condition: S, injection sample; C, carrier; L, liquid layer contacted with  $\text{TiO}_2$  NTs. The inserted Figure 16b shows the photocurrent response signals in flow injection analysis: 1,3, response signal of carrier; 2,4, response signal of injected sample. Original drawing was done by us.

through the  $\text{TiO}_2$  NTs incorporated thin layer cell, and the sample (S) was injected into the carrier intermittently. The degradation of organic compounds only took place when they were carried through the quartz window and illuminated by the light source. Thus, according to the exhaustive oxidation model, a serial of signals (see Figure 20b) were captured by the injected organics flowing through the thin layer cell. The COD

was obtained by calculating the signal, a single peak area, according to the relationship between COD and  $Q_{\text{net}}$ . Within such a system, the sample could be automatically tested and analyzed online. In this work, each analysis only took about 1–3 min; the linear range was as wide as up to  $1\text{--}500\text{ mg L}^{-1}$  of the compound of interest with the detection limit being  $1\text{ mg L}^{-1}$ . This device is therefore very promising for practical application.

Another online analytical system, proposed by Zhang et al.,<sup>323</sup> was based on a probe-type  $\text{TiO}_2$  photoanode for COD determination. In this system, a UV-LED light source and a USB microelectrochemical station were powered and controlled by a laptop computer, making the probe portable for onsite COD analyses (see Figure 21a). It was built on the

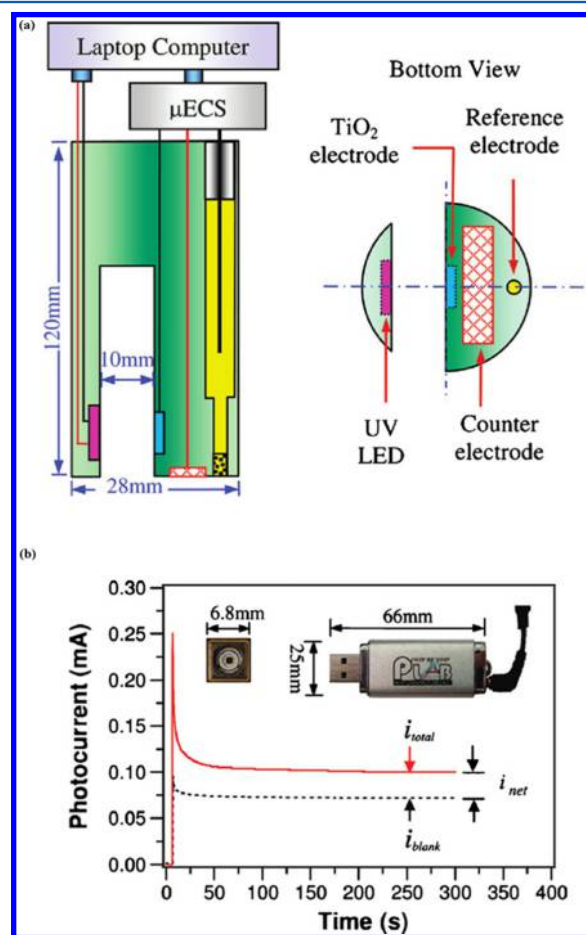


**Figure 21.** (a) Schematic diagram of the photoelectrochemical setup and PeCOD probe. (b) Typical photocurrent response of a 0.1 M  $\text{NaNO}_3$  blank solution ( $i_{\text{blank}}$ , dashed line) and a 0.1 M  $\text{NaNO}_3$  solution containing organic compounds ( $i_{\text{total}}$ , solid line).  $i_{\text{net}}$  is the difference between the two steady-state currents. The inset shows the images and dimensions of the UV-LED (left) and the  $\mu\text{ECS}$  microelectrochemical system (right). Reprinted with permission from ref 323. Copyright 2009 American Chemical Society.

typical photocurrent profiles generated by photocatalytic degradation of organics in water with  $\text{TiO}_2$ -based electrode, higher than the photocurrent generated (blank) without any organic compounds, as shown in Figure 21b. A net steady-state photocurrent can be calculated by subtracting the two photocurrents, which can be considered as eigenvalue for each organic substance. This value will change under different

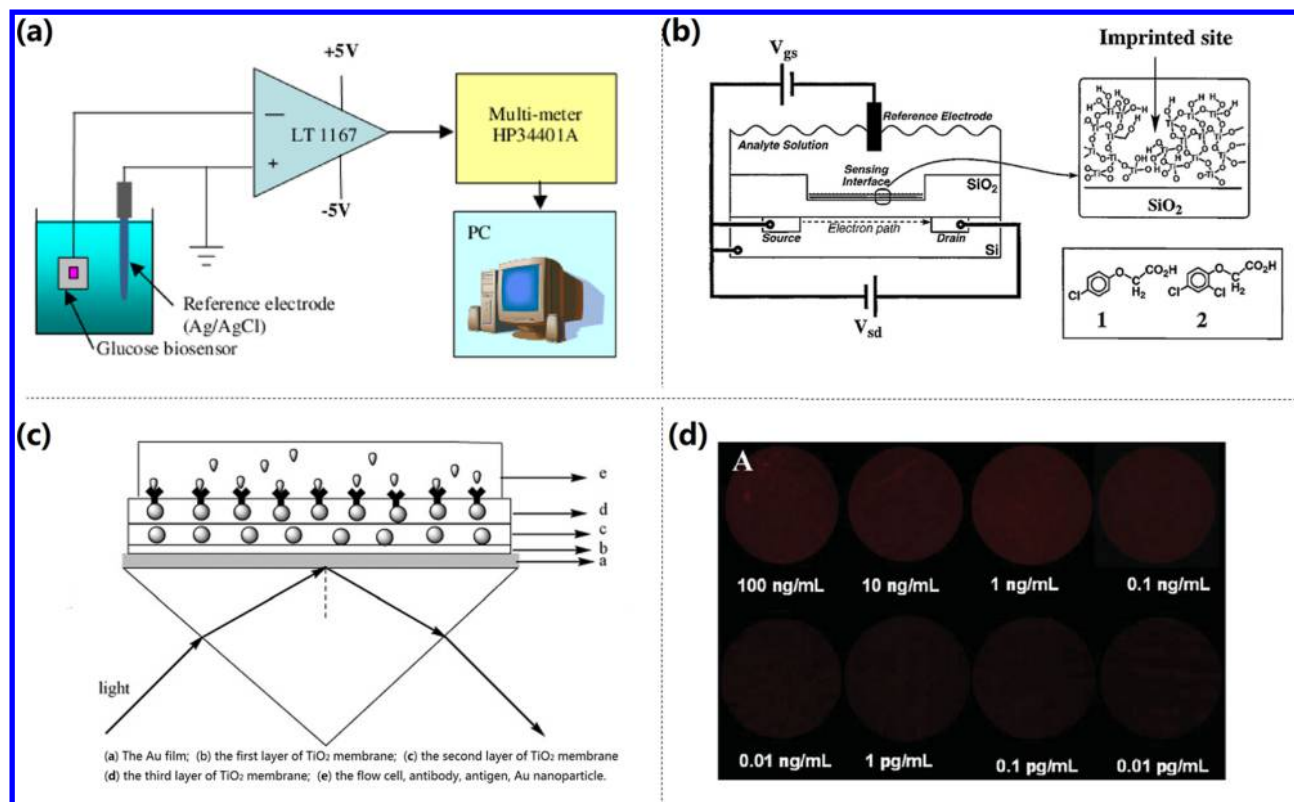


**Figure 22.** Schematic diagram of four typical biosensors: (a) Amperometric electrochemical biosensor. Reprinted with permission from ref 336. Copyright 2010 Elsevier. (b) Potentiometric electrochemical biosensor. Reprinted with permission from ref 337. Copyright 2001 American Chemical Society. (c) Optical biosensor based on SPR. Reprinted with permission from ref 338. Copyright 2010 Elsevier. (d) Optical biosensor based on fluorescence. Reprinted with permission from ref 339. Copyright 2010 Wiley-VCH.

organic substance concentrations. Under the optimized conditions, the net steady-state photocurrents that originated from the oxidation of organic compounds were directly proportional to COD concentrations. A practical detection limit of  $0.2 \text{ mg L}^{-1}$  and a linear range of  $0\text{--}120 \text{ mg L}^{-1}$  were achieved. This study did not use thin-layer cell but still realized the sensor micromation. The system, therefore, can be employed to detect COD in bulk reactor, which simplified the design and yet increased practicability.

Online analytical techniques have realized the automation of COD sensors. With respect to the preciseness and the efficiency,  $\text{TiO}_2$  nanomaterial-based photocatalytic techniques have started to show their advantages and are being quickly commercialized. As compared to traditional methods, these techniques are more precise, faster, and fit better with microminiaturization development.

**3.2.5. Brief Summary.** Among all kinds of photocatalytic-based COD sensors,  $\text{TiO}_2$  nanomaterials have attracted much attention thanks to their excellent stability and photocatalysis. In terms of sensing performance,  $\text{TiO}_2$  NPs based on COD sensor exhibit a performance not as good as that exhibited by COD sensor based on  $\text{TiO}_2$  NTs either in detection limit or detection range even when the impact of different measurement principles has been taken into consideration. For instance, the  $\text{TiO}_2$  NTs-based COD sensor<sup>311</sup> possesses a detection range of  $0\text{--}850 \text{ mg L}^{-1}$ , more desirable than a range of  $0\text{--}360 \text{ mg L}^{-1}$  possessed by the  $\text{TiO}_2$  NPs-based COD sensor.<sup>321</sup> In addition, the former demonstrates faster response and better reproducibility than the latter. Further, the tubular nanostructure favors the improvement of the sensor's detection range. It

is safe to say that the development of nanostructured  $\text{TiO}_2$  will play an important role in the emerging technology roadmap of COD sensor.

To improve the sensitivity of COD sensor, attention needs to be paid to the fact that the water body contains refractory organics and  $\text{Cl}^-$  ion, both of which may lead to a flawed detection value, lower than the actual one. As previously mentioned, some scholars have probed into the problem and investigated the mechanism behind it.<sup>312</sup> They have proposed an efficient solution;<sup>333</sup> yet, the problem is only partially solved. Thus, one of the future tasks is to further expand the applicability of the photoanodes by maximizing the oxidation percentage of environmentally significant and persistent organic compounds. On such grounds, a new standard could be established based on PeCOD to replace the traditional one so as to obtain a more accurate COD value, which will, to the greatest extent, approximate the actual one in the water body.

### 3.3. Biosensor

**3.3.1. Measurement Principle.** The measurement principle of a biosensor varies according to its sensing mechanisms. Figure 22 shows three typical biosensors with (a) amperometry (current),<sup>336</sup> (b) potentiometry (voltage),<sup>337</sup> optical radiation (including (c) surface plasmon resonance (SPR)),<sup>338</sup> and (d) fluorescence<sup>339</sup> as output signals, respectively.

**3.3.1.1. Amperometric Model.** Amperometric measurement is usually adopted in a three-electrode system in which  $\text{TiO}_2$  electrode serves as working electrode coupling with reference electrode and counter electrode as shown in Figure 22a.<sup>336</sup> Target chemicals are dispersed in the electrolyte solution, and a redox reaction is created in the sensor. The current signal



generated from the redox reactions of an electroactive species at a given potential during sensing process can be continuously collected using an electrochemical workstation.<sup>340</sup> Typically, two types of current collecting models called amperometry and voltammetry are used in the testing process, based on whether the given potential is constant or not. In voltammetric model, the variation of potential is applied from a cyclic voltammetry (CV) scan between the working electrode and the counter electrode.<sup>341</sup> For both models, the peak values of the current measured over a linear potential range are directly proportional to the bulk concentration of the analyte.<sup>342</sup> Using a saturated calomel electrode as reference, Figure 23a shows the CVs of

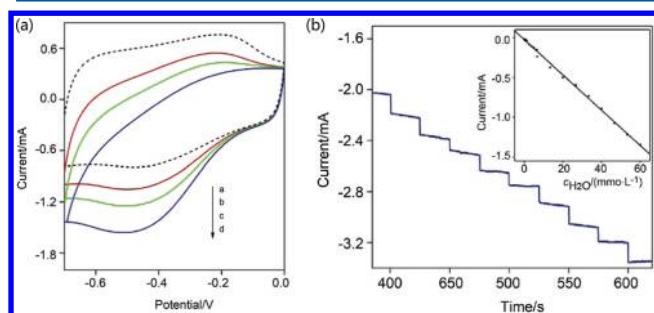


**Figure 23.** (a) CVs of Hb/C-TiO<sub>2</sub> NTs in the absence (a) or presence (d) of H<sub>2</sub>O<sub>2</sub> with different concentrations. (b) Typical amperometric response of H<sub>2</sub>O<sub>2</sub> at Hb/C-TiO<sub>2</sub> NTs with successive additions of H<sub>2</sub>O<sub>2</sub> at  $-0.45$  V. Reprinted with permission from ref 343. Copyright 2013 Wiley-VCH.

hemoglobin (Hb)/C-TiO<sub>2</sub> NTs in the absence (a) or the presence of H<sub>2</sub>O<sub>2</sub> of different concentrations. When H<sub>2</sub>O<sub>2</sub> was added, a typical peak current linearly associated with H<sub>2</sub>O<sub>2</sub> concentration was observed at about  $-0.42$  V.<sup>343</sup> A similar trend could be achieved by amperometry model when applying a constant potential. In the same experiment, as shown in Figure 23b, the steady-state current increases linearly with H<sub>2</sub>O<sub>2</sub> concentration after successive injections of H<sub>2</sub>O<sub>2</sub> to a stirred phosphate buffered saline (PBS) solution at  $-0.45$  V.

**3.3.1.2. Potentiometric Model.** Potentiometric measurement is usually adopted in an electrochemical cell, in which a potential signal can be obtained because of the accumulation of a charge potential when zero or no significant current flows through the working electrode relative to the reference electrode. Various field-effect transistor (FET) devices were

designed as potentiometric devices (see Figure 21b).<sup>337</sup> They are divided into the metal-oxide sensitive FET (MOSFET), the light-addressable potentiometric sensor (LAPS), the ion-sensitive FET (ISFET), and the ion-selective electrodes (ISE). Of those, ISFET and enzyme modified ISFET (EnFET) devices are the most studied and emphasized.<sup>344</sup>

The general working mechanism of FET is using an electric field to control the conductivity of a semiconductor film between two electrodes (i.e., the source and drain). The conductivity control is achieved by changing the electric field potential, relative to the third electrode, known as the gate. In linear mode, when the drain-to-source voltage is much less than the gate-to-source voltage, an FET operates like a resistor, and it can be switched between conductive and nonconductive states by changing the gate voltage. Alternatively, in saturation mode, an FET operates as a constant-current source and is often used as a voltage amplifier. In this mode, the level of current is mainly determined by the gate-to-source voltage. FET devices can detect weak-signal based on high impedance semiconductor; hence they are widely used in the growing field of electrochemical biosensing.<sup>340,345,346</sup> The change of the gate potential resulted from the sensing events provides a label-free detecting method, which is ideal for the electronic transduction of chemical or biochemical recognition. The sensing principle of TiO<sub>2</sub> nanowire FET device for rabbit IgG analyses is illustrated in Figure 24.<sup>347</sup>

**3.3.1.3. Optical Model.** The binding of biomolecules with targets would change the optical properties of electrode surface so that the variation of reflected light could be in proportion to the target concentration. Several types of optical models, including SPR, ECL, and fluorescence, are usually used for sensing signals based on light transducer rather than collecting electrochemical signals. Figure 21c shows the schematic diagram of a typical optical biosensor in which SPR reveals the concentration of the analyte. SPR is surface electromagnetic waves that propagate in a direction parallel to the metal/dielectric (or metal/vacuum) interface.<sup>348</sup> Because the wave is on the interface of the metal and the external medium (air or water, for example), these oscillations are very sensitive to any change of this interface such as the adsorption of molecules to the metal surface.

ECL is a kind of luminescence produced during electrochemical reactions in solutions where one/all reactants are produced electrochemically on the electrodes.<sup>349</sup> The measurement principle can be briefly described as: electrochemically

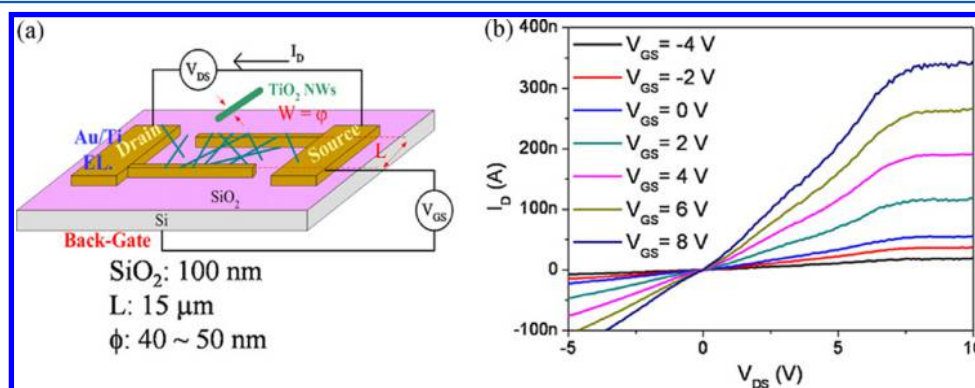


**Figure 24.** (a) Schematic diagram of bottom-gated multiwire TiO<sub>2</sub> NW device. (b) Gate-source voltage of TiO<sub>2</sub> NWs was measured to determine the relationship between the channel drain current and the drain–source voltage under various applied gate-source voltages. Reprinted with permission from ref 347. Copyright 2011 Elsevier.



generated intermediates undergo a highly exergonic reaction to produce an electronically excited state that, in turn, emits light upon relaxation to a lower-level state. The ECL biosensor is usually operated in an electrochemical cell that contains solution of luminescent species (polycyclic aromatic hydrocarbons,<sup>350</sup> metal complexes, quantum dots, or nanoparticles<sup>351</sup>) in aprotic organic solvent (ECL composition). ECL signal intensity is positively related to the concentration of luminescent species, so a specific analyte can be accurately determined according to the wavelength and intensity of emitted photon of light.

As for fluorescence, the fluorescence intensity is usually the manifestation of the concentration of a target substrate. For example, by loading antirabbit IgG on the TiO<sub>2</sub> electrode, the color changes when the amount of rabbit IgG is increased, as shown in Figure 21d.<sup>339</sup>

**3.3.2. Amperometric TiO<sub>2</sub> Biosensor.** Because reactions can be detected only when they are close to the electrode surface, the electrode material plays a crucial role in the electrochemical biosensors performances. In view of the functionality of a specific electrode, the surface modification and the dimensions of the electrode materials greatly influence its detection capability. Table 6 summarizes the sensing materials, and the performance of the amperometric TiO<sub>2</sub> biosensors developed in recent years.

TiO<sub>2</sub> material made by sol–gel method has been early studied and emerged as one matrix well suited for the immobilization of biomolecule (e.g., enzymes, protein molecules, and antibodies) and the construction of biosensor. As aforementioned in section 1.2.1, this kind of inorganic TiO<sub>2</sub> material can be prepared under ambient conditions and exhibits tunable porosity, high thermal stability, chemical inertness, and negligible swelling in both aqueous and nonaqueous solutions. It is well biocompatible and can retain the catalytic activities of biomolecule to a large extent. Various sol–gel made TiO<sub>2</sub> materials have been integrated into work electrode with binding molecules or polymer networks to form crack-free porous structures and have been characterized and applied to biosensing.<sup>352–360</sup> Yu et al.<sup>353</sup> developed an amperometric H<sub>2</sub>O<sub>2</sub> sensor by immobilizing horseradish peroxidase (HRP) in the TiO<sub>2</sub> film made by sol–gel method. When applied at –150 mV in the PBS/catechol electrolyte, the reduced form of catechol reacted further with the oxidized form of HRP to form reduced HRP, which catalyzes the reduction of H<sub>2</sub>O<sub>2</sub>. The sensor exhibited a rapid electrocatalytic response (less than 5 s), a linear calibration range from 0.08 to 0.56 mM with a detection limit of 1.5  $\mu$ M, and a high sensitivity (61.5  $\mu$ A mM<sup>–1</sup>) for H<sub>2</sub>O<sub>2</sub> monitoring.

By using sol–gel method and latex spheres template, ordered and periodic TiO<sub>2</sub> inversed-opal structure can be obtained. This structure favors photonic bandgaps (PBGs) and has become an important research area for biosensing. Cao et al.<sup>360</sup> proposed a 3D macroporous TiO<sub>2</sub> inverse opal biosensor. It was derived from a sol–gel procedure using polystyrene colloidal crystals as templates followed by incorporating them with glucose oxidase (GOx) as shown in Figure 25a. Because of the large effective surface of the three-dimensionally ordered macroporous structure, the obtained TiO<sub>2</sub> opal electrode had a better response to glucose concentration change than the ordinarily structured GOx/TiO<sub>2</sub>/ITO electrode. In their work, the sensitivity and the detection limit of glucose detection were 151  $\mu$ A cm<sup>–2</sup> mM<sup>–1</sup> and 0.02  $\mu$ M at a signal-to-noise ratio of 3, respectively. Using similar TiO<sub>2</sub> opal matrix, Wei et al.<sup>111</sup> deposited gold nanoparticles to prepare a three-dimensionally

ordered macroporous (3DOM) biosensor for H<sub>2</sub>O<sub>2</sub> detection. Under the same condition, 3DOM nanostructure showed superior properties over the gold-nanoparticle doped titanium dioxide nanoneedles (GTDNs) film in detection range and sensitivity. Specifically, it reached a linear range from 5.0  $\mu$ M to 1.0 mM and a sensitivity of 0.6  $\mu$ M, respectively (see Figure 25b).

Porous TiO<sub>2</sub> is a good candidate for biosensing materials due to its high surface area and tunable pore size. On the basis of the template-assisted hydrothermal method, various porous TiO<sub>2</sub> matrixes can be used for biosensing.<sup>361–365</sup> Mesoporous TiO<sub>2</sub> synthesized by Pluronic F127 template-assisted hydrothermal method has a highly organized mesoporous film with 8 nm diameter pore arrays. After layer-by-layer deposition of Prussian blue into the pores, the H<sub>2</sub>O<sub>2</sub> biosensor exhibits high reproducibility, environmental stability, and high sensitivity.<sup>364</sup> Bao et al.<sup>365</sup> reported porous TiO<sub>2</sub> material synthesized by carbon nanotube (CNT) template-assisted hydrothermal method. This material was applied in glucose biosensor, and when tested without any electron media, it showed facile, direct electrochemistry and good electrocatalytic performance. On the basis of the direct electrochemistry, high specific surface area, and unique nanostructures, the fabricated glucose sensor showed good stability, high sensitivity, and superb immobilizing effect on biomolecules. The slack porous TiO<sub>2</sub> has great attractiveness as a biosensing material, especially an enzyme-based biosensing material.

Other nanostructured TiO<sub>2</sub><sup>366–379</sup> including TiO<sub>2</sub> nanowires, TiO<sub>2</sub> nanoneedles, TiO<sub>2</sub> nanospheres, and TiO<sub>2</sub> nanotubes are also used as a matrix for sensor fabrication. In the nanostructured TiO<sub>2</sub>, vertically aligned TiO<sub>2</sub> NTs are widely employed for facilitating electron transfer as well as serving as a prospectively ideal “vessel” for immobilizing various biological components, such as enzyme, hemoglobin, antibody, antigen, cells, DNA, and bacteria.<sup>372–379</sup> Xie et al.<sup>372</sup> fabricated highly ordered TiO<sub>2</sub> NTs with an inner diameter of 60 nm and a total length of 540 nm by anodizing titanium foils. After the immobilization of GOx/pyrrole, the proposed electrochemical biosensor exhibited a very low detection limit, high stability, and very good reproducibility detecting glucose. Under the optimized conditions, the biosensor exhibited a high sensitivity of 45.5  $\mu$ A mM<sup>–1</sup> and a very low detection limit of 2  $\mu$ M. Vertically aligned TiO<sub>2</sub> NTs (see Figure 26) were also used to detect Pb<sup>2+</sup> where DNA was immobilized after a controllable carbon hybridization.<sup>379</sup> The designed DNA/C-TiO<sub>2</sub> NTs sensor for lead detection exhibited high sensitivity, selectivity, repeatability, wide pH adaptability, fast electro-accumulation capacity for lead, and easy regeneration, which are all attributed to the enhanced bioelectrochemical activities and the immobilization of abundant target biomolecules, DNA. The controllable carbon hybridization of the TiO<sub>2</sub> NTs retained its tubular structure, hydrophilicity, and biocompatibility, and also increased the conductivity of the electrode. The results showed that the lead sensor achieved a wide linear calibration range (0.01–160 nM) with the detection limitation of 3.3 pM. To our knowledge, this type of sensor is already realized for Pb<sup>2+</sup> determination in real water samples.

TiO<sub>2</sub> nanocomposite integrated with other semiconductor nanoparticles can provide better electron transportation and show an excellent capability to immobilize enzyme as well. So far, semiconductor composites such as graphene, NiO, SiO<sub>2</sub>, CeO<sub>2</sub>, ZrO<sub>2</sub>, CdTe, Fe<sub>3</sub>O<sub>4</sub>, and PbO<sub>2</sub> have been applied in various types of biosensors.<sup>380–388</sup> For example, TiO<sub>2</sub>–

Table 6. Summary of the Sensing Properties of Amperometric  $\text{TiO}_2$  Biosensor<sup>a</sup>

TiO <sub>2</sub> nanostruct	fabricatn method	electrode	biomolec	analyte	response					ref
					K <sub>m</sub> (mM)	D (mM)	L (μM)	S (μA mM <sup>-1</sup> cm <sup>-2</sup> )	RT (s)	
TiO <sub>2</sub> NPs	sol-gel	GCE	HRP	H <sub>2</sub> O <sub>2</sub>		4.0 × 10 <sup>-3</sup> to 1.0	0.8		30	352, 2002
TiO <sub>2</sub> NPs	sol-gel	GCE	HRP	H <sub>2</sub> O <sub>2</sub>	1.89	0.08–0.56	1.5	61.5	5	353, 2002
TiO <sub>2</sub> NPs	sol-gel	GCE	hemoglobin	H <sub>2</sub> O <sub>2</sub>	0.018	5.0 × 10 <sup>-4</sup> to 5.0 × 10 <sup>-2</sup>	0.12	1.29 × 10 <sup>3</sup>	5	354, 2003
TiO <sub>2</sub> NPs	sol-gel	GCE	tyrosinase	phenol	0.29	1.2 × 10 <sup>-4</sup> to 2.6 × 10 <sup>-1</sup>	0.1	103	5	355, 2003
TiO <sub>2</sub> NPs	sol-gel	GCE		HCG		2.5–12.5 mIU/mL	1.4 mIU/mL			356, 2005
TiO <sub>2</sub> NPs	sol-gel	Ti wires	urease	urea		8 × 10 <sup>-3</sup> to 3	5		25	357, 2009
TiO <sub>2</sub> NPs/LDH/silica	sol-gel	gold electrode	lactate dehydrogenase	lactic acid	2.2 × 10 <sup>-3</sup>	1.0 × 10 <sup>-3</sup> to 20 × 10 <sup>-3</sup>	0.4			358, 2008
TiO <sub>2</sub> NPs/Prussian blue	sol-gel	gold electrodes	GOx	glucose		0.02–15	5 × 10 <sup>3</sup>	12.74	10	359, 2008
TiO <sub>2</sub> opal	sol-gel/inverse opals	ITO electrode	GOx	glucose	1.4	0.05–2.5	0.02	151		360, 2008
TiO <sub>2</sub> opal	sol-gel/template	OTE	HRP	H <sub>2</sub> O <sub>2</sub>		0.5 × 10 <sup>-3</sup> to 6 × 10 <sup>-3</sup>	0.01	102.97		398, 2009
TiO <sub>2</sub> opal	sol-gel/template	ITO	hemoglobin	H <sub>2</sub> O <sub>2</sub>		5 × 10 <sup>-3</sup> to 1	0.6	144.5		111, 2011
nanoporous TiO <sub>2</sub> NPs (Nafion)	sol-gel	GCE	GOx	glucose		0–7	15		2	361, 2005
porous TiO <sub>2</sub> NPs	sol	Pt electrodes	GOx	glucose	6.08	0–3			30	362, 2001
mesoporous CNT/titania/Nafion	sol	GCE	alcohol dehydrogenase	ethanol		1 × 10 <sup>-5</sup> to 3 × 10 <sup>-3</sup>		51.6	2	363, 2007
mesoporous TiO <sub>2</sub> NPs	block-copolymer template	ITO		H <sub>2</sub> O <sub>2</sub>			0.03 ± 0.01	415 ± 20		364, 2010
TiO <sub>2</sub> nanofibers	electrospinning	Pt electrodes	GOx	glucose		0.01–6.98	0.01	9.25	10	365, 2008
TiO <sub>2</sub> nanoneedles	sol	ITO glass	cytochrome c	H <sub>2</sub> O <sub>2</sub>		8.5 × 10 <sup>-4</sup> to 24	0.26			366, 2010
carbonized TiO <sub>2</sub> nanotubes	hydrothermal	GCE	hemoglobin	H <sub>2</sub> O <sub>2</sub>	87.5 × 10 <sup>-3</sup>	1.0 × 10 <sup>-3</sup> to 0.1	0.92		3	367, 2009
Au/TiO <sub>2</sub> nanospheres	nano-TiO <sub>2</sub>	GCE	GOx/ferrocene	ProGRP		10.0–500 pg/mL	3.0 pg/mL			368, 2008
Pt/TiO <sub>2</sub> nanofiber	electrospinning	alumina		hydrazine			0.142	44.42		110, 2011
TiO <sub>2</sub> NWs		GCE	HRP	H <sub>2</sub> O <sub>2</sub>		0.004–1.15	0.32	124		369, 2009
TiO <sub>2</sub> NTs	hydrothermal	Ti foil	HRP	H <sub>2</sub> O <sub>2</sub>	1.9	5.0 × 10 <sup>-4</sup> to 1.0 × 10 <sup>-2</sup>	0.1			370, 2008

Table 6. continued

TiO <sub>2</sub> nanostruct	fabricatn method	electrode	biomolec	analyte	response					ref
					K <sub>m</sub> (mM)	D (mM)	L (μM)	S (μA mM <sup>-1</sup> cm <sup>-2</sup> )	RT (s)	
TiO <sub>2</sub> microspheres	hydrothermal	GCE	HRP	H <sub>2</sub> O <sub>2</sub>	4 × 10 <sup>-4</sup> to 1.4 × 10 <sup>-1</sup>	0.05			3	371, 2011
TiO <sub>2</sub> NTs	anodization	Ti electrode	GOx/pyrrole	glucose	0.01–1.0	2.0		45.5	5.6	372, 2007
Au/TiO <sub>2</sub> nanotube arrays	anodization	Ti electrode	HRP	H <sub>2</sub> O <sub>2</sub>	5 × 10 <sup>-3</sup> to 0.4	2			5	373, 2008
Pt-Au/TiO <sub>2</sub> nanotube arrays	anodization	Ti electrode	GOx	glucose	0–1.8	100		0.083661	3	374, 2008
Au/TiO <sub>2</sub> NTs	anodization	Ti electrode	cytochrome c	H <sub>2</sub> O <sub>2</sub>	2 × 10 <sup>-3</sup> to 3.49 × 10 <sup>-1</sup>	1.21				375, 2008
TiO <sub>2</sub> NTs/Prussian blue (PB)/Au	anodization	Ti electrode	GOx	glucose	0.015–4.00	5		36	10	376, 2009
Pt/carbon nanotubes/TiO <sub>2</sub> NTs	anodization	Ti electrode	GOx	glucose	0.006–1.5	5.7		0.24	3	377, 2009
C/TiO <sub>2</sub> NTs	anodization	Ti electrode	HRP and Th	H <sub>2</sub> O <sub>2</sub>						388, 2009
C/TiO <sub>2</sub> NTs	anodization	Ti electrode	hemoglobin	H <sub>2</sub> O <sub>2</sub>	8.5 × 10 <sup>-2</sup>	7.0 × 10 <sup>-8</sup>	3.1 × 10 <sup>-5</sup>		10	353, 2002
Au/TiO <sub>2</sub> hollow microsphere	hydrothermal	CPE	probe DNA	DNA sequence	1.0 × 10 <sup>-12</sup> to 1.0 × 10 <sup>-8</sup> mol/L	2.3 × 10 <sup>-13</sup> mol/L				411, 2010
PbO <sub>2</sub> /TiO <sub>2</sub> /Ti	sol–gel	Ti foil	acetylcholinesterase enzyme (AChE)	organophosphorous pesticides	1.34	1 × 10 <sup>-5</sup> to 2 × 10 <sup>-2</sup>	1 × 10 <sup>-4</sup>			382, 2013
TiO <sub>2</sub> –CeO <sub>2</sub> NPs	sol–gel	ITO glass	urease (Urs)	urea	4.8	10–700 mg/dL	0.166	0.9165	10	388, 2009
CeO <sub>2</sub> /TiO <sub>2</sub> NPs/Chit	TiO <sub>2</sub> powder	GCE	glutamate dehydrogenase tyrosinase	phenol	65.84 ± 2.41	1.0 × 10 <sup>-5</sup> to 5.0 × 10 <sup>-2</sup>	9.0 × 10 <sup>-3</sup>	86	2	381, 2008
TiO <sub>2</sub> /ZrO <sub>2</sub>		ITO	urease (Urs) and glutamate dehydrogenase (GLDH)	urea		5–100 mg/dL	0.44	2.74		382, 2013
TiO <sub>2</sub> /Er <sub>2</sub> O <sub>3</sub>	reactive sputtering	Si electrode	urease	urea				9.25 mV/mM	10	383, 2009
graphene/TiO <sub>2</sub> NPs/CTS	hydrothermal	carbon ionic liquid electrode	methylene blue	DNA sequence	1.0 × 10 <sup>-6</sup> to 1.0	7.21 × 10 <sup>-7</sup>				109, 2012
TiO <sub>2</sub> NPs/graphene	P25	GCE	GOx	glucose	0–8			6.2		384, 2012
TiO <sub>2</sub> NPs/graphene/NiO	hydrothermal	GCE	GOx	glucose	1.0–12.0	1.2		4.129	3	383, 2009
TiO <sub>2</sub> NPs/graphene	simple casting method	GCE	acetylcholinesterase (AChE)	organophosphate compounds (OPs)	0.22	0.001–2 ug mL <sup>-1</sup>	0.3 ng mL <sup>-1</sup>			386, 2011
Fe <sub>3</sub> O <sub>4</sub> /TiO <sub>2</sub> NPs	hydrothermal	carbon electrode	AChE	organophosphate compounds (OPs)		0.02–10 nM	0.01 nM			387, 2013
TiO <sub>2</sub> NPs/PEDOT	sol–gel	ITO glass		nicotine	0–5		4.9	31.35		389, 2009
TiO <sub>2</sub> NPs/Nafion	sol–gel		GOx	glucose	0.1–0.6	10		240	20	390, 2011

Table 6. continued

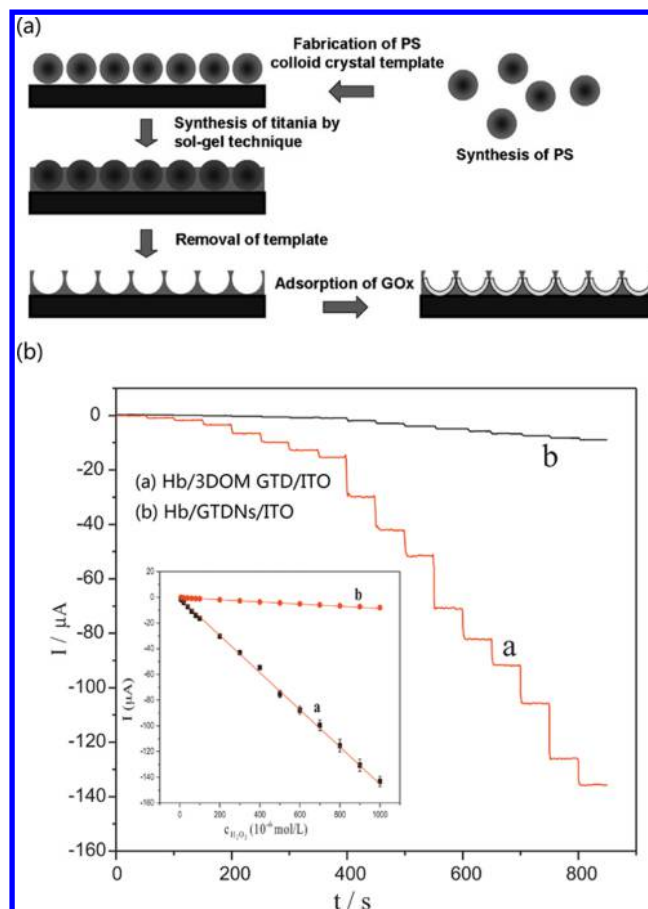
response										ref
TiO <sub>2</sub> nanostruct	fabricatn method	electrode	biomolec	analyte	K <sub>m</sub> (mM)	D (mM)	L (μM)	S (μA mM <sup>-1</sup> cm <sup>-2</sup> )	RT (s)	
Nafion/graphene/TiO <sub>2</sub> nanorods	hydrothermal	CILE	Hb	H <sub>2</sub> O <sub>2</sub>	3.3	0.6–21.0	0.22			391, 2013
TiO <sub>2</sub> NTs/methylene blue (MB)/chitosan	anodization	Ti electrode	HRP	H <sub>2</sub> O <sub>2</sub>		3 × 10 <sup>-4</sup> to 1.2 × 10 <sup>-1</sup>	9 × 10 <sup>-2</sup>	350	5	392, 2009
TiO <sub>2</sub> NTs/methylene blue (MB)/chitosan	anodization	Ti electrode	hemoglobin	H <sub>2</sub> O <sub>2</sub>	1.02	4.9 × 10 <sup>-6</sup>	1.5	31.8	5	393, 2011
Ag/TiO <sub>2</sub> NPs	TiO <sub>2</sub> suspension	gold electrode	protein kinase A	ATP		0 to 1 × 10 <sup>3</sup>	0.2			399, 2009
Pt /TiO <sub>2</sub> NTs	NaOH autoclave	GCE	GOx	glucose		2 × 10 <sup>-3</sup> to 12	1	43.6	3	400, 2010
Au/TiO <sub>2</sub> NPs	TiO <sub>2</sub> powder	GCE	HRP	H <sub>2</sub> O <sub>2</sub>	0.63	4.1 × 10 <sup>-2</sup> to 0.63	5.9		3	401, 2010
Au/graphene/TiO <sub>2</sub> NPs	TiO <sub>2</sub> powder	GCE	anti-CEA	CEA		0.01–80 ng/mL	3.4 pg/mL			402, 2011
TiO <sub>2</sub> /graphene/Pt/Pd		GCE	ChOx	cholesterol	0.21	5.0 × 10 <sup>-5</sup> to 5.9 × 10 <sup>-1</sup>	0.017		7	416, 2013
mesoporous TiO <sub>2</sub> /Pt nanowhiskers		ITO		glutathione		0.5–40 μmol L <sup>-1</sup>	0.1			394, 2012
TiO <sub>2</sub> NPs /AFP/CdTe	TiO <sub>2</sub> powder	ITO	GOx	AFP		0.5 pg/mL to 10 μg/mL	0.13 pg/mL			108, 2012
graphene/TiO <sub>2</sub> NPs	hydrothermal	GCE		NADH		1.0 × 10 <sup>-5</sup> to 2.0	3.0 × 10 <sup>-3</sup>			395, 2012
FeTPPS/TiO <sub>2</sub> nanoparticles	TiO <sub>2</sub> powder	ITO		glutathione		0.05–2.4	0.03		15	396, 2010
Au/TiO <sub>2</sub> NTs	anodization	Ti foil	antibodies/GOx	a-synuclein		50 pg mL <sup>-1</sup> to 100 ng mL <sup>-1</sup>	34 pg mL <sup>-1</sup>	34		397, 2010
chitosan/CdSe <sub>2</sub> Te <sub>1-x</sub> /TiO <sub>2</sub> NTs	anodization	Ti foil	BSA	PCP		1 nM to 0.3 μM	1 pM			405, 2010
CdSe/TiO <sub>2</sub>	liquid phase deposition	FTO	DNA	o-aminophenol		4.0 × 10 <sup>-7</sup> to 2.7 × 10 <sup>-5</sup> ML <sup>-1</sup>	8.0 × 10 <sup>-8</sup> ML <sup>-1</sup>			407, 2014
CdS QDs/TiO <sub>2</sub> NTs	anodization	Ti foil	antibodies	prostate-specific antigen			0.5 ng mL <sup>-1</sup>			408, 2012
WO <sub>3</sub> /TiO <sub>2</sub> NPs	Degussa P25	ITO		norepinephrine/riboflavin		3.23 × 10 <sup>-6</sup> to 3.88 × 10 <sup>-4</sup> M	1.7 × 10 <sup>-6</sup> M			409, 2012
						3.23 × 10 <sup>-7</sup> to 4.0 × 10 <sup>-5</sup> M	1.87 × 10 <sup>-7</sup> M			
CdSe/TiO <sub>2</sub> -RGO		ITO	antibodies	carcinoembryonic antigen		0.003–100 ng mL <sup>-1</sup>	1.38 pg mL <sup>-1</sup>			414, 2014
dopamine/TiO <sub>2</sub> NPs	sol	ITO		NADH		5.0 × 10 <sup>-7</sup> to 1.2 × 10 <sup>-4</sup> M	1.4 × 10 <sup>-7</sup> M			410, 2009
TiO <sub>2</sub> NPs	Degussa P25	carbon electrode		organophosphorus pesticides		0.2–1.0 μmol L <sup>-1</sup>	2.0 nmol L <sup>-1</sup>			415, 2011
PTCA/TiO <sub>2</sub> NPs		GCE		organophosphorus pesticides		0.1–10 nmol L <sup>-1</sup>	0.08 nmol L <sup>-1</sup>			416, 2013



Table 6. continued

TiO <sub>2</sub> nanostruct	Au/TiO <sub>2</sub> NPs	fabricatn method	electrode	probe DNA	biomolec	analyte	response					ref
							$K_m$ (mM)	$D$ (mM)	$L$ ( $\mu$ M)	$S$ ( $\mu$ A mM <sup>-1</sup> cm <sup>-2</sup> )	RT (s)	
		Degussa P25	FTO			linear DNA hybridization			1 nM			417, 2008

<sup>a</sup>Sensitivity,  $S$ ; linearity,  $L$ ; detection limit, DL; detection range, DR; Michaelis–Menten constant,  $K_m$ ; response time, RT; shelf life, SL; and reusability, Re.



**Figure 25.** (a) Schematic diagram of the fabrication procedure of the TiO<sub>2</sub> inverse opal by sol-gel technique. Reprinted with permission from ref 360. Copyright 2008 Wiley-VCH. (b) Amperometric responses of Hb/3DOM GTD/ITO electrode at an operating potential of  $-0.52$  V upon successive additions of H<sub>2</sub>O<sub>2</sub> in pH 7.0 PBS buffer. Reprinted with permission from ref 111. Copyright 2011 Elsevier.

graphene nanocomposite has a larger surface area, higher conductivity, and chemical stability with DNA.<sup>110</sup> It has been tested as a matrix in biosensing, in which the corresponding biosensor responded to DNA sequence in the range of  $1.0 \times 10^{-6}$  to  $1.0$  mM, with a detection limit of  $7.21 \times 10^{-7}$  M under optimized conditions. Similarly, TiO<sub>2</sub>–graphene nanohybrid was also used to detect organophosphorous pesticides (OPs) and exhibited a good a detection limit of  $0.3$  ng mL<sup>-1</sup>.<sup>386</sup> Moreover, Fe<sub>3</sub>O<sub>4</sub>/TiO<sub>2</sub> magnetic nanoparticles were prepared for the detection of OPs.<sup>387</sup> On the basis of the magnet, the composite was easily isolated from sample solutions, and the released cadmium ions were detected on a disposable screen-printed electrode (SPE), yielding a linear response over a broad OP-BChE concentration range from  $0.02$  to  $10$  nM, with a detection limit of  $0.01$  nM. As another example, the TiO<sub>2</sub>/SiO<sub>2</sub> nanocomposite-based glucose biosensor has achieved a wide determination concentration range, fast response, low detection limit, and high sensitivity. It has already been applied into the determination of glucose in human serum, and the feedback was successful. Using the dip-coating method, TiO<sub>2</sub>–CeO<sub>2</sub> nanocomposite film<sup>388</sup> was successfully deposited onto ITO-coated glass substrate and was then applied in a urea biosensor. By immobilizing mixed enzyme [urease (Urs) and glutamate dehydrogenase (GLDH)] on this composite electrode, the urea

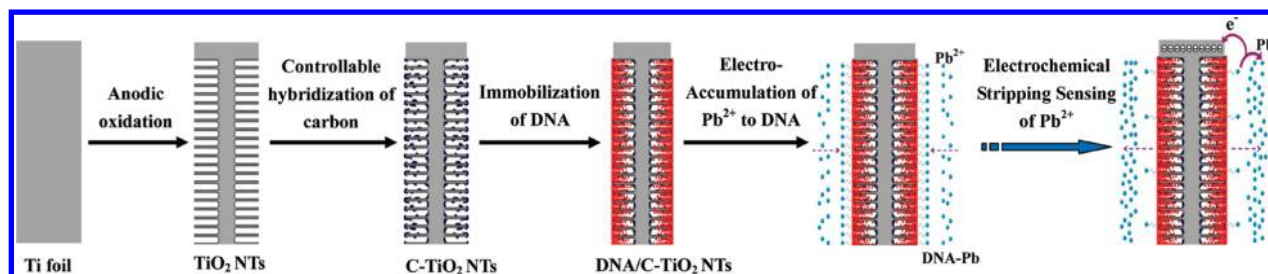


**Figure 26.** Schematic illustration for DNA/C-TiO<sub>2</sub> NTs construction and its Pb ion monitoring. Reprinted with permission from ref 379. Copyright 2010 American Chemical Society.

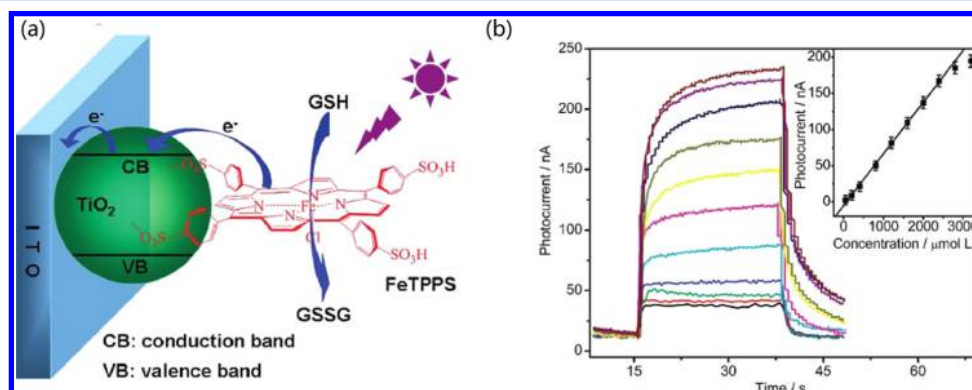


**Figure 27.** (a) Schematic illustration of photoelectrochemical process for oxidation of GSH at FeTPPS-TiO<sub>2</sub>-modified ITO electrode. (b) Photocurrent responses at FeTPPS-TiO<sub>2</sub>-modified ITO electrode in 0.1 M pH 7.0 PBS in the presence of 0, 50, 200, 400, 800, 1200, 1600, 2000, 2400, 2800, and 3200  $\mu\text{mol L}^{-1}$  GSH (from bottom to top) at +0.2 V to a light excitation at 380 nm. Inset: Linear calibration curve. Reprinted with permission from ref 396. Copyright 2010 American Chemical Society.

biosensor showed a response time of 10 s, a sensitivity of  $0.9165 \text{ uA cm}^{-2} \text{ mM}^{-1}$ , and a detection limit of 0.166  $\mu\text{M}$ .

TiO<sub>2</sub> related polymer composite provides a good platform for enzyme immobilization.<sup>389–393</sup> The presence of polymer, such as Nafion, chitosan, and cellulose, can help to prevent cracking of TiO<sub>2</sub> matrix, especially for sol–gel made film as mentioned above. In addition, each organic–inorganic hybrid material has its unique characteristic. For example, organic–inorganic hybrid material based on chitosan is biodegradable and nontoxic because chitosan is a natural polymer product. Moreover, amino groups in chitosan provide the hybrid material with a hydrophilic environment, which is compatible with the biomolecules. TiO<sub>2</sub>/cellulose composite fibers can be easily prepared from the hydrolysis of alkoxide after mixture of titanium alkoxide and cellulose and used to immobilize enzyme under mild reaction conditions.<sup>392</sup> The fibers are also easy to store. It was reported that the fibers were stable even in high ionic solutions with a wide range of pH values from 3 to 10.<sup>392</sup>

Because of super oxidation of TiO<sub>2</sub> under light illumination, photolight could be used to enhance the performance of biosensor with better biomolecule detection, which might need a high potential for oxidation.<sup>394–417</sup> Tu et al.<sup>396</sup> proposed the porphyrin-functionalized TiO<sub>2</sub> nanoparticles for glutathione (GSH) sensing through the dentate binding of TiO<sub>2</sub> nanoparticles with sulfonic groups of [meso-tetrakis(4-sulfonatophenyl)porphyrin] iron(III) monochloride (FeTPPS) as shown in Figure 27a. The proposed photoelectrochemical biosensor showed a rapid response, wide concentration range, low applied potential, and good selectivity in monitoring GSH under UV light. It can be seen from Figure 27b that the photocurrent density reversely correlated with the GSH concentration. Under the optimal conditions, the response

displayed a linear increase as the GSH concentration increased from 0.05 to 2.4  $\text{mmol L}^{-1}$  with a detection limit of 0.03  $\text{mmol L}^{-1}$ . A similar principle was adopted by Wei et al.,<sup>404</sup> who fabricated a photoelectrochemical biosensor for organophosphorous pesticides detection using acetylcholinesterase enzyme (AChE) functionalized PbO<sub>2</sub>/TiO<sub>2</sub>/Ti electrode. The detection currents were proportional to the organophosphorous pesticides, and the linearity range was from 0.01 to 20  $\mu\text{M}$  with a detection limit of 0.1 nM.

For TiO<sub>2</sub>-based photoelectrochemical biosensor, a critical issue has to be considered that the UV light ( $\lambda < 400 \text{ nm}$ ) causes severe damage to biomolecules. To overcome the problem, coupling with other narrow band gap semiconductors such as CdSe,<sup>405–407</sup> CdS,<sup>408</sup> and WO<sub>3</sub><sup>409</sup> is essential for TiO<sub>2</sub>-based biosensor to enhance the absorption in the visible range and to increase the duration of charge carriers. For example, Kang et al.<sup>405</sup> proposed a CdSe<sub>x</sub>Te<sub>1–x</sub> modified TiO<sub>2</sub> NTs biosensor using a photoelectron-deposition method as shown in Figure 28. Benefiting from CdSe<sub>x</sub>Te<sub>1–x</sub>, the sensor had a strong absorption of visible light and showed a lower density of recombination centers (surface states). Consequently, it enjoyed a longer lifetime of photogenerated carriers. By being loaded with an antibody pentachlorophenol (PCP) Ab and bovine serum albumin (BSA), the proposed sensor performed a label-free sensing to PCP (one of the most commonly environmental pollutants) with a linearity range of 1 nM to 0.3  $\mu\text{M}$  and a detection limit of 1 pM. In addition to semiconductor, Wang et al.<sup>410</sup> found that dopamine-coordinated TiO<sub>2</sub> nanoporous films had a wide excitation range of light in the visible region (up to 580 nm). This strategy largely reduces the destructive effect of UV light and the photogenerated holes of illuminated TiO<sub>2</sub> on biomolecules. In this research, the

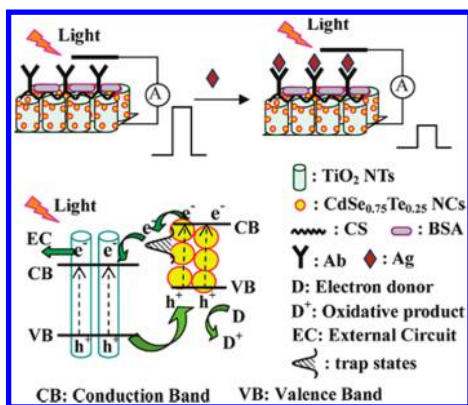


**Figure 28.** Scheme diagram of the immunosensor construction and ideal stepwise band edge structures for efficient transport of the excited electrons and holes in CdSe<sub>0.75</sub>Te<sub>0.25</sub>/TiO<sub>2</sub> NT electrodes. Reprinted with permission from ref 405. Copyright 2010 American Chemical Society.

detection limit of NADH was  $1.4 \times 10^{-7}$  M, and the detection range could extend up to  $1.2 \times 10^{-4}$  M. Another research reported by Chen et al.<sup>411</sup> showed that HRP functional TiO<sub>2</sub> NTs has an obvious photocurrent response under visible-light (400 nm) irradiation possibly due to the specific 1D ordered structure of TiO<sub>2</sub> NTs. By adding H<sub>2</sub>O<sub>2</sub> to the electrolyte, the photocurrent intensity increased with the increase of H<sub>2</sub>O<sub>2</sub> concentration, showing a low detection limit of  $1.8 \times 10^{-7}$  M for H<sub>2</sub>O<sub>2</sub> determination.

**3.3.3. TiO<sub>2</sub> Potentiometric Biosensor.** It is of increasing interest to apply ion-sensitive field-effect transistor in chemical sensing. The sensing process will be accompanied by a gate potential change, which gives a label-free advantage when recognizing the electronic transduction of chemical and biochemical processes. The gates of ISFET devices can be modified with nano-TiO<sub>2</sub> to meet different kinds of sensing purpose. Table 7 summarizes the sensing materials and performance of the potentiometric TiO<sub>2</sub> biosensors developed in recent years.

Chu et al.<sup>347</sup> proposed a TiO<sub>2</sub> nanowires FET sensor for rabbit IgG detection, as shown in Figure 29. They found that polypyrrole propylic acid (PPa) was a good material for the encapsulization of biomolecular on 1D nanomaterials. In their work, rabbit IgG as target protein was detected by this sensor, and a linear range for rabbit IgG determination from 119 pg/mL to 5.95 ng mL<sup>-1</sup> with a detection limit of  $-3.96$  A/(ng mL<sup>-1</sup>) for 5 V of the applied drain-source voltages was achieved.

The extended gate field-effect transistor (EGFET) was developed for biosensor using screen-printed technology. In a typical process, the conductive material as electrical transmitted layer is printed on the flexible plastic substrate, and the TiO<sub>2</sub> sensing membrane is deposited by RF sputtering system or sol-gel method. Lee et al.<sup>418</sup> investigated the performance of this type of electrodes for detecting glucose and achieved a linear range from 0 and 400 mg dL<sup>-1</sup> with a detection limit of 74.1 nV/cm<sup>2</sup>(100 mg dL<sup>-1</sup>)<sup>-1</sup> glucose. Chou et al.<sup>419</sup> printed UV glue on the surface of TiO<sub>2</sub> and successfully monitored uric acid concentration in blood. It was proved that the high chemical stability of TiO<sub>2</sub> sensing membrane maintained the sensing capability during electrochemical response in extreme pH environment.

Ozasa et al.<sup>420,421</sup> developed a two-dimensional electron-gas-field-effect-transistor (2DEG-FET) for cell-viability sensor. The TiO<sub>2</sub> film was prepared on GaAs (001) substrate by spin-coating of TiO<sub>2</sub> sol-gel. The 2DEG-FET electrode was fabricated with the combination of conventional photolithographic technique: wet etching by 1NH<sub>4</sub>OH:1H<sub>2</sub>O<sub>2</sub>:100H<sub>2</sub>O solution, and liftoff of vacuum-evaporated Au thin films. The performance of the 2DEG-FET-based sensor was characterized by examining H<sub>2</sub>O<sub>2</sub> concentration detection. As reported, a sensitivity of 410 mV mM<sup>-1</sup> was achieved.<sup>420</sup>

Much progress has been made on TiO<sub>2</sub> thin film-based ISFET technique. Lahav et al.<sup>423</sup> achieved an impressive selectivity in sensing Na<sup>+</sup>-1 and Na<sup>+</sup>-2, with a detection limit of  $(5 \pm 2) \times 10^{-4}$  M for Na<sup>+</sup>-1 and  $(1.0 \pm 2.0) \times 10^{-5}$  M for Na<sup>+</sup>-2, using a TiO<sub>2</sub> film that was imprinted with molecule sites for 4-chlorophenoxy acetic acid or 2,4-dichlorophenoxy acetic acid. Pogorelova et al.<sup>424</sup> prepared an imprinted polymeric membrane in an ISFET by the polymerization of titanium(IV) butoxide with titanium(IV) phosphonate complex. The membrane has recognition sites for various types of benzylphosphonic acid derivatives. The membrane-based sensor exhibited selectivity toward the imprinted substrates, the response time of which is ca. 45 s.

The present study has revealed that the imprint of chiroselective and chiroselective molecular recognition sites in TiO<sub>2</sub> thin films is associated with a field-effect transistor. The TiO<sub>2</sub> modified by chiral imprint can even be used to detect chiral organic compounds, such as chiral carboxylic acids. Lahav et al.<sup>425</sup> imprinted (R)- or (S)-2-methylferrocene carboxylic acids, (R)-1 or (S)-1, (R)- or (S)-2-phenylbutanoic acid, (R)-2 or (S)-2, and (R)- or (S)-2-propanoic acid, (R)-3 or (S)-3 onto TiO<sub>2</sub> thin film on the gate surface of ISFET device.<sup>370</sup> The imprinted sites reveal chiroselectivity and chiroselectivity only toward the imprinted enantiomer. Zayats et al.<sup>426</sup> examined the molecular imprinted inorganic TiO<sub>2</sub> film for the recognition of carboxylic acids (e.g., 4-chlorophenoxyacetic acid, fumaric acid, and maleic acid). The imprinted sites revealed selectivity toward the specific substrates. The subsequent elimination of the carboxylate yields the molecular contours of the carboxylate in the TiO<sub>2</sub> film and generates a Ti(IV)-OH site that undergoes dissociation that controls the gate potential. Thus, rebinding carboxylate to the imprinted sites can be electronically transduced by the functional ISFET device.

**3.3.4. TiO<sub>2</sub> Optical Biosensor.** In addition to the methods described above, optical transduction is conducted on the basis of surface resonance, electrochemiluminescence, or fluorescence. The light intensity at characteristic peak is usually the manifestation of the concentration of a target substrate. This method not involving liquid phase is superior to other methods. Table 7 summarizes the sensing materials and the performance of the optical TiO<sub>2</sub> biosensors developed in recent years.

**3.3.4.1. SPR.** Wang et al.<sup>338</sup> proposed a TiO<sub>2</sub>-based SPR biosensor, which showed the relationship between the concentration of human IgG and the shift of the resonant wavelength based on different sensing membranes. It demonstrated a satisfactory response to human IgG in the concentration range of 0.30–40.00 μg mL<sup>-1</sup>, 0.60–40.00 μg mL<sup>-1</sup>, 2.50–40.00 μg mL<sup>-1</sup>, and 5.00–40.00 μg mL<sup>-1</sup>, respectively.

Mun et al.<sup>427</sup> developed an optical interferometric biosensor for detecting rabbit IgG. The probe protein A was electrostatically bounded to the TiO<sub>2</sub> NTs and acted as a specific biomolecule for IgG. The optical reflectivity was a key index to

Table 7. Summary of the Sensing Properties of TiO<sub>2</sub> Potentiometric and Optical Biosensor As Well As Other Biosensor Type<sup>a</sup>

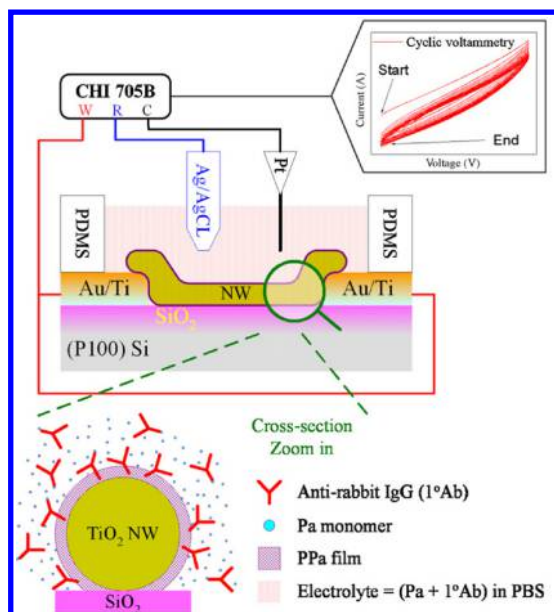
TiO <sub>2</sub> nanostruct	fabricatn method	transducer	biomolec	analyte	response					ref
					DR	DL	S	RT (s)	SL	
TiO <sub>2</sub> NWs	hydrothermal	EnFET	antirabbit IgG	rabbit IgG	119 pg/mL to 5.95 ng/mL	−3.96 A/(ng/mL)				347, 2011
TiO <sub>2</sub> NPs	sol–gel	EnFET	GOx	glucose	0–400 mg/dL		74.1 (nV cm <sup>−2</sup> ) (100 mg/dL) <sup>−1</sup>			418, 2008
TiO <sub>2</sub> NPs	R.F.	EGFET		uric acid						417, 2008
TiO <sub>2</sub> NPs	sol–gel	2DEG-FETs		H <sub>2</sub> O <sub>2</sub>			410 mV/mM			420, 2007
TiO <sub>2</sub> NPs	sol–gel	2DEG-FETs		H <sub>2</sub> O <sub>2</sub>			4.5 mV/μM			421, 2008
TiO <sub>2</sub> NPs/SiO <sub>2</sub>	sol–gel	ISFETs		chloroaromatic acids	5.0 × 10 <sup>−4</sup> to 6.0 × 10 <sup>−3</sup> M (1.0 ± 0.2) × 10 <sup>−5</sup> M	(5 ± 2) × 10 <sup>−4</sup> M 0.1–9.0 mM				423, 2001
TiO <sub>2</sub> NPs	sol–gel/ imprint	ISFETs		bthiophenol	5 × 10 <sup>−6</sup> to 8 × 10 <sup>−4</sup> M					424, 2004
TiO <sub>2</sub> /SiO <sub>2</sub> NPs	sol–gel	fluorescence	GOx	glucose	1.0 × 10 <sup>−9</sup> to 1.0 × 10 <sup>−2</sup> M	1.2 × 10 <sup>−10</sup> M		45		428, 2009
TiO <sub>2</sub> NTs	anodization	fluorescence	antirabbit IgG	rabbit IgG	0.1 pg mL <sup>−1</sup> to 100 ng mL <sup>−1</sup>	0.01 pg mL <sup>−1</sup>		89.7% after 3 mo		336, 2010
CdTe QDs/TiO <sub>2</sub> NTs	anodization	fluorescence		Bap (PAHs)	400 nM to 40 pM	15 pM				429, 2010
TiO <sub>2</sub> NPs	vapor deposition	fluorescence	urease	urea	2 × 10 <sup>−3</sup> to 0.3 mM	3.1 × 10 <sup>−6</sup> M				430, 2010
			GDH	glucose	2 × 10 <sup>−2</sup> to 10 mM	5.4 × 10 <sup>−6</sup> M				
			GLDH	glutamate	4 × 10 <sup>−2</sup> to 8 mM	7.8 × 10 <sup>−6</sup> M				
TiO <sub>2</sub> NPs	sol–gel	fluorescence		glutamate	0.02–10 mM	6.7 × 10 <sup>−6</sup> M		>80% after 5 weeks		431, 2006
TiO <sub>2</sub> NRs	GLAD	SPR								432, 2008
Au/titania membrane	sol–gel	SPR	rabbit antihuman IgG	human IgG	0.30–40.00 ug mL <sup>−1</sup>			57% after 30 da		433, 2010
TiO <sub>2</sub> NPs/SiO <sub>2</sub>		OWLS		trifluralin	2 × 10 <sup>−7</sup> to 3 × 10 <sup>−5</sup> ng mL <sup>−1</sup>					434, 2003
PLA/AuAg/TiO <sub>2</sub> (FIA)		ECL		H <sub>2</sub> O <sub>2</sub>	10 pM to 50 nM	0.822 pg				435, 2014
CdTe/CdS QDs/TiO <sub>2</sub> NTs	anodization	ECL	antibody	TBC	5.0 × 10 <sup>−7</sup> M to 4.0 × 10 <sup>−3</sup> M	6 pM		90% (after 1 mo)		436, 2014
Au/TiO <sub>2</sub> NPs	hydrothermal	ECL	GOx	glucose		2.5 × 10 <sup>−7</sup> M				437, 2013
AuAg/TiO <sub>2</sub> NPs		ECL		H <sub>2</sub> O <sub>2</sub>	0.42–170 nM	1.17 × 10 <sup>−13</sup> g		97% (after 15 da)		438, 2013
PLA/TiO <sub>2</sub> NTs	anodization	ECL	antibody	TBC	0.25–2.0 mg L <sup>−1</sup>	0.2 nM				439, 2013
PLA/TiO <sub>2</sub> NPs (FIA)		ECL		antioxidant	0.001–20 ng/mL	69.9 pg				440, 2013
CNTs/TiO <sub>2</sub> NPs	sol–gel	ECL	antibody <sub>2</sub>	prostate-specific antigen	400–10 000 cells per mL	0.8 pg/mL		stable after 3 weeks		441, 2013



Table 7. continued

TiO <sub>2</sub> nanostruct	fabricatn method	transducer	biomolec	analyte	response					ref
					DR	DL	S	RT (s)	SL	
CdS/TiO <sub>2</sub>	solvothermal	ECL	antibody	HepG2 cell	2.0 fg mL <sup>-1</sup> to 50 µg mL <sup>-1</sup>	396 cells per mL				442, 2013
CdS/TiO <sub>2</sub> NTs	anodization	ECL	antibody	RlgG	3.0 × 10 <sup>-12</sup> M to 1.0 × 10 <sup>-9</sup> M	1.0 fg mg <sup>-1</sup>				443, 2012
Ag/TiO <sub>2</sub> NTs	anodization	ECL		benzopyrene	1.0 × 10 <sup>-9</sup> M to 1.0 × 10 <sup>-4</sup> M	1.0 × 10 <sup>-12</sup> M				444, 2010
Ru(bpy) <sub>3</sub> <sup>2+</sup> /TiO <sub>2</sub> NTs	anodization	ECL		amines	0.02–25 mIU/mL	1.0 × 10 <sup>-9</sup> M				445, 2010
Ru(bpy) <sub>3</sub> <sup>2+</sup> /TiO <sub>2</sub> NPs		ECL	BSA	HCG	7.5 × 10 <sup>-9</sup> M to 2.5 × 10 <sup>-3</sup> M	0.007 mIU/mL				446, 2010
chitosan/Ru(bpy) <sub>3</sub> <sup>2+</sup> /TiO <sub>2</sub> NPs	hydrothermal	ECL		DBAE	0.30–10.00 mg/L	1.67 × 10 <sup>-10</sup> M				447, 2009
Nafon/TiO <sub>2</sub> NPs	Degussa P25	ECL		DO	2.0 × 10 <sup>-8</sup> g/mL to 1.0 × 10 <sup>-6</sup> g/mL	0.12 mg/L				448, 2008
Nafon/Ru(bpy) <sub>3</sub> <sup>2+</sup> /TiO <sub>2</sub> NPs	Degussa P25	ECL		chlorpheniramine maleate		6.0 × 10 <sup>-9</sup> g/mL				449, 2006
Au/TiO <sub>2</sub> NTs	anodization	surface-enhanced Raman scattering		BaP (PAHs)	1.0 × 10 <sup>-7</sup> to 1.0 × 10 <sup>-3</sup> M	1.26 × 10 <sup>-8</sup> M				450, 2012
Ag/TiO <sub>2</sub> NPs		PQC	probe DNA	<i>E. coli</i>						451, 2009
TiO <sub>2</sub> NPs	sol-gel	piezoelectric	probe DNA	<i>Pseudomonas aeruginosa</i>	10 <sup>-1</sup> to 10 <sup>-3</sup> g L <sup>-1</sup>	10 <sup>-4</sup> g L <sup>-1</sup>				452, 2004

<sup>a</sup>Sensitivity, S; detection limit, DL; detection range, DR; response time, RT; and shelf life, SL.



**Figure 29.** Experiment setup of the electrochemical polymerization (ECP) system. Reprinted with permission from ref 312. Copyright 2011 Elsevier.

distinguish the targets and analyze their concentration. As compared to porous  $\text{SiO}_2$  or porous  $\text{Al}_2\text{O}_3$ , the advantages of  $\text{TiO}_2$  NTs lie in the superb chemical stability in the pH range 2–12 and the sufficiently high surface affinity to allow strong noncovalent binding of the captured probe protein A.

**3.3.4.2. ECL.** The history of  $\text{TiO}_2$  NPs, in retrospect, resembles the history of other kinds of biosensor.  $\text{TiO}_2$  NPs were chosen and used for the ECL biosensor in its early stage due to its larger surface, more chemical activities, and electrocatalysis. Song et al.<sup>449</sup> reported a nano-titania/Nafion membrane with a  $\text{Ru}(\text{bpy})_3^{2+}$  label for the determination of chlorphenamine maleate (CPM). As a conventional label chemical,  $\text{Ru}(\text{bpy})_3^{2+}$  was immobilized via both an ion-exchange process and hydrophobic interactions. In this work, CPM was detected by the sensor, and a linear range for CPM determination from  $2.0 \times 10^{-8}$  to  $1.0 \times 10^{-6}$  g  $\text{mL}^{-1}$  with a detection limit of  $6.0 \times 10^{-9}$  g  $\text{mL}^{-1}$  was achieved. On the other hand, Tu's group<sup>438,454</sup> found that the nanosized noble metals such as AuAg and Au showed great potency for intensifying the ECL of luminol. They can promote, because of their effective catalytic properties, the formation of superoxide bound to  $\text{Ti}^{4+}$  and boost generation of electron–hole couples in  $\text{TiO}_2$  due to the depressed Fermi level pinning effect. By coupling them with  $\text{TiO}_2$  NPs, the scholars established a flow injection ECL analytic platform (ECL-FIA) for the determination of  $\text{H}_2\text{O}_2$  and fruitful antioxidant activity in application. With the use of AuAg/ $\text{TiO}_2$  NPs, a good mass detection limit of  $1.17 \times 10^{-13}$  g was achieved.<sup>435</sup>

It is worth noting that most studies have focused on  $\text{TiO}_2$  NTs as the substrate of the sensor over the past 4 years. The reason, as aforementioned, probably lies in the distinct tubular features of  $\text{TiO}_2$  NTs so that  $\text{TiO}_2$  nanotubes-based ECL sensors can be used to amplify the detected signals. Additionally, the numbers of hydroxyl groups on  $\text{TiO}_2$  NTs surfaces offer plenty of active points for function. In early 2010, Xu et al.<sup>445</sup> developed  $\text{Ru}(\text{bpy})_3^{2+}$  immobilized  $\text{TiO}_2$  NTs for the determination of amines in water. As reported, the sensor exhibits excellent sensitivity with a limit of detection of  $1.0 \times$

$10^{-9}$  M. It also shows a fast ECL response because the tubular structure provides a short diffusion path for active molecules from the solution to the active surface. Later, Song et al.<sup>443</sup> invented an ECL immunosensor based on CdS quantum dots (QDs) decorated  $\text{TiO}_2$  NTs, controllable with chemical bath deposition technique. Making use of the characteristics of cyclic ECL curves, the CdS/ $\text{TiO}_2$  NTs show 5-fold higher ECL intensity than that from the CdS/ $\text{TiO}_2$  compact layer for antigen detection. Cai's group<sup>431</sup> further proposed a label-free immunosensor based on core/shell thick CdTe/CdS quantum dots-functionalized  $\text{TiO}_2$  nanotube for a kind of flame retardant (tris-(2,3-dibromopropyl) isocyanurate, TBC) determination. Encapsulating the CdTe QDs with a thick layer of CdS can significantly increase the structural stability and suppresses the nonradiative recombination process of the QDs, as shown in Figure 31. In this work, the limit of detection (LOD) was determined to be 6 pM, which is comparable to the reported HPLC–MS method.<sup>452</sup>

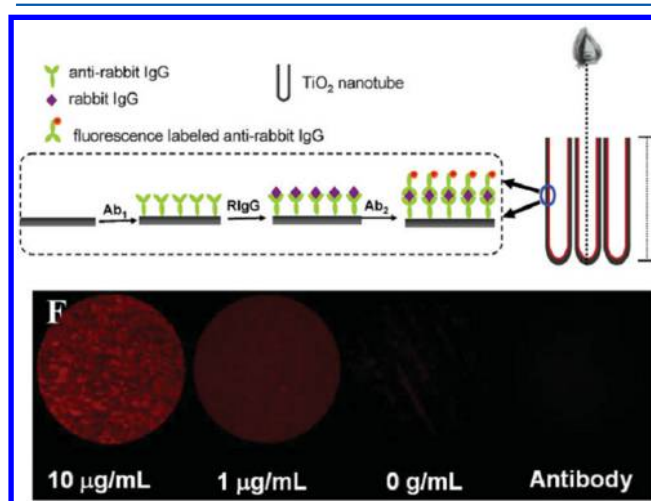


**Figure 30.** Scheme of immunoassay based on high-aspect-ratio  $\text{TiO}_2$  NTs. Fluorescence images of a sandwich-type immunoassay on  $\text{TiO}_2$  NTs for different RlgG concentrations and a control sample. Reprinted with permission from ref 339. Copyright 2010 Wiley-VCH.

**3.3.4.3. Fluorescence.** Li et al.<sup>422</sup> fabricated a  $\text{TiO}_2/\text{SiO}_2$  composite using sol–gel method and then applied it for glucose detection. The construction of the sensor was similar to that of other enzyme-based amperometric sensors, but the phosphorescence was instead used as monitoring signal. When glucose was continuously added, the phosphorescence intensity and the color of the biosensor changed dramatically. In their work, the linear range was from  $1.0 \times 10^{-9}$  to  $1.0 \times 10^{-2}$  M with a detection limit of  $1.2 \times 10^{-10}$  M and 89.76% of the initial performance sustained even after 3 months operation.

Song et al.<sup>339</sup> proposed a  $\text{TiO}_2$  NTs-based fluorescence immunosensor shown in Figure 30. They constructed a sandwich fluorescence immunoassay in combination of  $\text{TiO}_2$  NTs, antirabbit IgG, and target rabbit IgG (Figure 30). The sensor color gradually changed with an increase in the amount of the target matters. The linear range for rabbit IgG determination was from  $0.1 \text{ pg mL}^{-1}$  to  $100 \text{ ng mL}^{-1}$  with a detection limit of  $0.01 \text{ pg mL}^{-1}$ . In their work, a noticeable advantage was the self-cleaning offered by  $\text{TiO}_2$  NTs due to its excellent photocatalytic properties, which made the immunosensor reusable after short UV treatment. Moreover, the detection range could be significantly extended by using

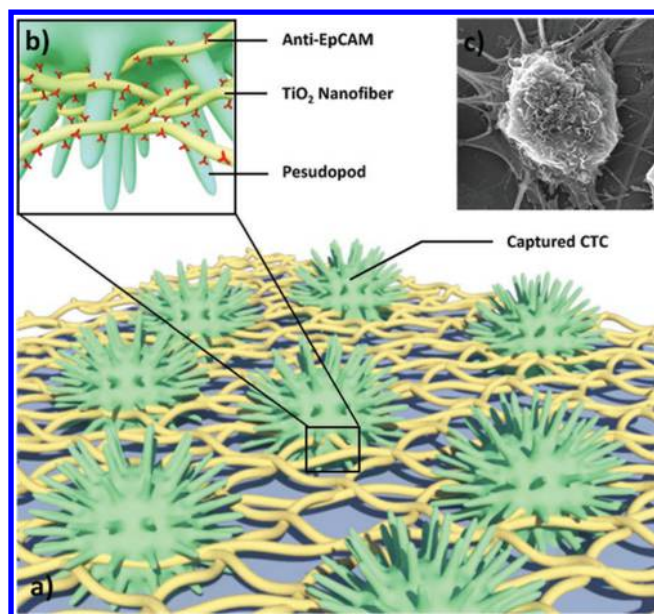


**Figure 31.** Schematic representation of the horizontally packed TiO<sub>2</sub> FBs for improved CTC capture through combining cell-capture-agent (i.e., Anti-EpCAM) and cancer cell-preferred nanoscale topography. Reprinted with permission from ref 457. Copyright 2012 Wiley-VCH.

transparent TiO<sub>2</sub> NTs based on a glass substrate, which allows for transmission-based UV/vis spectrophotometric detection. Similarly, Yang et al.,<sup>429</sup> incorporating CdTe with TiO<sub>2</sub> NTs, established a fluorescence sensor for benzo(a) pyrene (BaP) detection, a type of polycyclic aromatic hydrocarbons (PAHs). By loading BaP on the composite film, the detection limit was as low as 15 pM. In their work, the concentration of PAHs was proportional to the relative fluorescence intensity at 410–370 nm. Therefore, the sensor can be directly applied for PAHs detection without a need for calibration.

**3.3.5. Other TiO<sub>2</sub> Biosensor.** Surface-enhanced Raman spectroscopy or surface-enhanced Raman scattering (SERS) is a surface-sensitive technique that enhances Raman scattering through molecules adsorbed on rough metal surfaces or through nanostructures. In recent years, it has been considered to be a quantitative analytical technique, for instance, in single molecule detection.<sup>455</sup> In practice, SERS is critically dependent on its active substrates; thus providing available support for loading the active materials becomes very important. Cai's group<sup>450</sup> proposed a SERS biosensor using Au decorated TiO<sub>2</sub> NTs for detecting Bap (PAHs). In this work, they used TiO<sub>2</sub> NTs as sensor due to their advantages of tunable pore sizes and highly oriented growth characteristics, on the grounds of which active materials can be modified in their interior and outer space. The linear range for Bap determination was from  $1.0 \times 10^{-7}$  to  $1.0 \times 10^{-3}$  M with a detection limit of  $1.26 \times 10^{-8}$  M.

Piezoelectric quartz crystal (PQC) is a technology based on the electric charge that accumulates in crystals in response to applied mechanical stress. The PQC is sandwiched between two electrodes, which are generally composed of gold or silver on the quartz surface. As compared to electrochemical and optical methods, the PQC biosensor provides a label-free detection method using simple and portable equipment setup. Like most biosensors, a PQC electrode with high surface area and good biocompatibility is favored to increase the amount of active recognition molecules on the surface for a desirable sensitivity. Thanks to the advantages of nano TiO<sub>2</sub>, Sun et al.<sup>451</sup>

proposed a nano-Ag/TiO<sub>2</sub>-coated PQC electrode for detecting *E. coli* in environmental water. In their work, a detection limit of eight *E. coli* cells was obtained, which requires sampling at least 800 mL of water to detect a single *E. coli* cell in 100 mL of water.

Cell biosensor based on nanostructured TiO<sub>2</sub> is of new interest in tissue engineering because live cells and nanostructured materials share dimensions similar to those of cellular surface components and extracellular matrix (ECM) scaffolds. In a study of bone-remodeling-associated cells, TiO<sub>2</sub> NTs with a specific geometry presented their good cell adhesion and differentiation.<sup>456</sup> Later, using electrospun TiO<sub>2</sub> nanofiber, Zhang et al.<sup>457</sup> reported a cell capture assay for detecting circulating tumor cells (CTCs) from colorectal and gastric cancer patients. As shown in Figure 31, TiO<sub>2</sub> nanofiber grafted with cell capture agent (i.e., Anti-EpCAM) is well matched with pseudopod of CTCs in diameter. This implies that sufficient contact and efficient adhesive force can be formed, which may lead to improved cell/substrate affinity. This is further proved by a comparison with flat Si substrate, which had a very weak ability in capturing CTCs, whereas TiO<sub>2</sub> nanofiber deposited substrates exhibited considerable capture efficiency; for example, CTCs were captured respectively in two out of three cases with counts ranging from 0 to 2 CTCs per 0.5 mL blood sample of colorectal cancer patients, and seven out of seven cases with counts ranging from 3 to 19 CTCs per 0.5 mL blood sample of gastric cancer patients.

**3.3.6. Brief Summary.** A broad biosensor is one that can detect a variety of samples covering not only biomolecules (bacteria, cell, DNA, protein) but also environmental pollutants (Pesticide, flame retardant, polycyclic aromatic hydrocarbons). In this Review, various TiO<sub>2</sub>-based biosensors were fully discussed and well confirmed for their wide application.

As for other types of sensors, selectivity is an important feature for a biosensor. Reviewing most of the work, the analyte specificity for a biosensor is mainly established on the interaction between biological recognition elements and analyte, for example, the antigen–antibody interaction, which guarantees the highest selectivity.

On the other hand, the sensitivity is probably the most highly concerned feature of a biosensor. Sensitivity is, in effect, related to many factors, and excellent sensitivity depends on the proper choice of measurement technology, biological recognition elements, and electrode matrix. In terms of TiO<sub>2</sub> matrix, the nanostructured TiO<sub>2</sub>, obviously, shows remarkable advantages over the planar, including large surface area for loading more biomolecules, a short diffusion path for active molecules from the solution to the active surface, and fast electron transfer for signal capture, etc. As far as TiO<sub>2</sub> NTs are concerned, they have become one of the most popular TiO<sub>2</sub> matrixes in various biosensors. An obvious explanation is that TiO<sub>2</sub> NTs own all of the above-mentioned merits in addition to low cost and easy fabrication. This means that a feasible way to further improve the sensitivity of a biosensor lies with the newly developed nanostructured TiO<sub>2</sub>, which is probably superior to the TiO<sub>2</sub> NTs. Moreover, modifying TiO<sub>2</sub> with other chemicals (semiconductors, metal elements, polymers) also will help improve its sensitivity; say, graphene<sup>110,386</sup> can greatly promote electron transfer rate and electrocatalytic activity, which would benefit an electrochemical biosensor, or noble metal is an essential active material for the conjugation of biomolecules.



#### 4. SUMMARY AND FUTURE PROSPECTS

TiO<sub>2</sub> nanomaterials possess large specific surface area and unique attributes in chemical, physical, optical, electronic, and photocatalytic fields. Moreover, they possess nontoxic and environmentally friendly nature, excellent biocompatibility and stability, which allow TiO<sub>2</sub> nanomaterials to be adopted in a wide range of sensing devices, that is, gas sensing, COD sensing, and biosensing.

In terms of gas sensor, TiO<sub>2</sub>-based sensor is widely applicable for the detection of various gases such as H<sub>2</sub>, O<sub>2</sub>, CO, H<sub>2</sub>O, VOCs, etc. However, several obstacles have to be overcome for its future application. For example, the working temperatures are still high (~200 °C), and the recovery time is too long. These shortcomings can be partly avoided or improved by depositing noble metals, by composing with other semiconductors, and, most importantly, by introducing newly developed nanostructured TiO<sub>2</sub> to the sensors. Furthermore, the current research focuses merely on the target analyte in a simple matrix instead of complex matrixes and real samples.

In terms of COD sensor, TiO<sub>2</sub> nanomaterials-based COD sensors could effectively degrade organic pollutants photocatalytically and be widely applied in water pollutants monitoring systems. As compared to traditional monitoring methods, it dramatically improved the environmental monitoring technique. Above all, online monitoring became realistic because of the use of photocurrent as COD indication, which greatly simplified the monitoring process. Currently, researchers have entered the realm of in situ applications of surface water monitoring, and the results are promising. In the future, further application of this technique in more fields, such as industrial wastewater monitoring, can be expected. Because of the complexity of industrial wastewater, which contains many refractory organic matters, it is quite important to widen the applicability of the TiO<sub>2</sub>-based photoanodes by maximizing the oxidation percentage of a wide spectrum of organics. Furthermore, the online and on-site determination technology is also crucial. This could be achieved by combining emerging modern technologies, in particular, modern electronic technology, microelectronic lithography for sensor array construction, micromachining for lab-on-chip fabrication, microfabrication, and computing technology for automation.

Last but not least, TiO<sub>2</sub> is a perfect candidate for biosensors due to its good biocompatibility. According to different sensing mechanisms, TiO<sub>2</sub> biosensors could be embedded into electrochemical/optical systems. Most developments have been focused on amperometric devices as they can provide the fastest and most accurate measurements to date. The performance of biosensor can be improved by the introduction of other noble metals, inorganic and organic compounds, and by developing new nano materials. Research on biosensors is not only driving the ever-accelerating race to construct smaller, faster, cheaper, and more efficient devices, but also conducive to the successful integration of electronic and biological systems.

Overall, to develop efficient sensors with high accuracy, precision, reproducibility, and low detection limits, it is necessary to optimize the properties and microstructure of TiO<sub>2</sub>. Thus, factors such as electronic properties, chemical composition, structure and crystallinity, surface states, and morphology need to be further elucidated in great detail. Specifically, it is of top priority to construct novel, robust, and highly efficient nanostructured TiO<sub>2</sub> electrode by using modern

material synthesis technologies. Further, more simple synthetic methods should be investigated to the development of the microfabrication process to industrialize the application and fabrication of microminiaturized, integrated, and online monitoring sensors.

#### AUTHOR INFORMATION

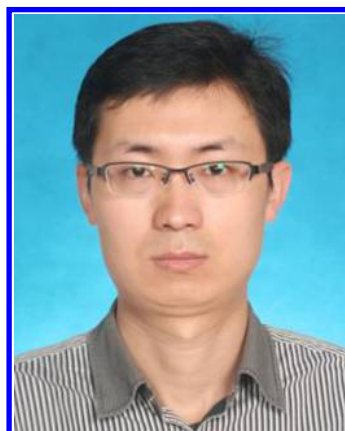
##### Corresponding Author

\*E-mail: zhoubaoxue@sjtu.edu.cn.

##### Notes

The authors declare no competing financial interest.

##### Biographies



Jing Bai holds a Ph.D. degree in environmental science from Shanghai Jiao Tong University in 2010 (supervisor: Prof. Baoxue Zhou). His Ph.D. research focused on the development of nanomaterials for organic pollutants treatments and environmental sensor, and he received “Outstanding Shanghai doctoral thesis” in 2012. He is currently working as an assistant researcher at Shanghai Jiao Tong University. His research is focused on the design of new strategies using nanomaterials for water splitting and organic pollutants treatments.



Baoxue Zhou is professor and head of the environmental function material group at School of Environmental Science and Engineering, Shanghai Jiao Tong University. He received his doctoral degree from Harbin Institute of Technology. His research is focused on photocatalytic/photoelectrocatalytic technology of nanomaterials for organic pollutants treatments, hydrogen production from water decomposition, and environmental sensor.



## ACKNOWLEDGMENTS

We would like to acknowledge the National Nature Science Foundation of China (nos. 20677039, 21177085, 21276153), Shanghai Commission for Science and Technology (no. 11JC1406200), and the 985 project (III) in China Universities (no. SJTU-TS0423116001) for financial support.

## REFERENCES

- (1) Akimoto, H. *Science* **2003**, *5*, 302.
- (2) Akyildiz, I. F.; Su, W.; Sankarasubramaniam, Y.; Cayirci, E. *IEEE Commun. Mag.* **2002**, *40*, 102.
- (3) Blais, F. J. *Electron. Imaging* **2004**, *13*, 231.
- (4) Waggoner, P. S.; Craighead, H. G. *Lab Chip* **2007**, *7*, 1238.
- (5) Grieshaber, D.; MacKenzie, R.; Vörös, J.; Reimhult, E. *Sensors* **2008**, *8*, 1400.
- (6) Homola, J. *Chem. Rev.* **2008**, *108*, 462.
- (7) Baughman, R. H.; Zakhidov, A. A.; De Heer, W. A. *Science* **2002**, *297*, 787.
- (8) Wang, Z. L. *J. Phys.: Condens. Matter* **2004**, *16*, R829.
- (9) Dai, Z. R.; Pan, Z. W.; Wang, Z. L. *Adv. Funct. Mater.* **2003**, *13*, 9.
- (10) Eranna, G.; Joshi, B. C.; Runthala, D. P.; Gupta, R. P. *CRC Crit. Rev. Solid State Sci.* **2004**, *29*, 111.
- (11) Lu, J. G.; Chang, P.; Fan, Z. *Mater. Sci. Eng., R* **2006**, *52*, 49.
- (12) Barsan, N.; Koziej, D.; Weimar, U. *Sens. Actuators, B* **2007**, *121*, 18.
- (13) Fujishima, A.; Honda, K. *Nature* **1972**, *37*, 238.
- (14) Fujishima, A.; Rao, T. N.; Tryk, D. A. *J. Photochem. Photobiol., C* **2000**, *1*, 1.
- (15) Tryk, D. A.; Fujishima, A.; Honda, K. *Electrochim. Acta* **2000**, *45*, 2363.
- (16) Grätzel, M. *Nature* **2001**, *414*, 338.
- (17) Konstantinou, I. K.; Albanis, T. A. *Appl. Catal., B* **2004**, *49*, 1.
- (18) Ni, M.; Leung, M. K. H.; Leung, D. Y. C.; Sumathy, K. *Renewable Sustainable Energy Rev.* **2007**, *11*, 401.
- (19) Millis, A.; Le Hunte, S. J. *Photochem. Photobiol., A* **1997**, *108*, 1.
- (20) Ghicov, A.; Schmuki, P. *Chem. Commun.* **2009**, *20*, 2791.
- (21) Chen, X. B.; Mao, S. S. *Chem. Rev.* **2007**, *107*, 2891.
- (22) Fujishima, A.; Zhang, X.; Tryk, D. A. *Surf. Sci. Rep.* **2008**, *63*, 515.
- (23) Grimes, C. A. *J. Mater. Chem.* **2007**, *17*, 1451.
- (24) Linsebigler, A. L.; Lu, G.; Yates, J. T., Jr. *Chem. Rev.* **1995**, *95*, 735.
- (25) Wunderlich, W.; Oekermann, T.; Miao, L. *J. Ceram. Process. Res.* **2004**, *5*, 343.
- (26) Thompson, T. L.; Yates, J. T. *Chem. Rev.* **2006**, *106*, 4428.
- (27) Diebold, U. *Surf. Sci. Rep.* **2003**, *48*, 53.
- (28) Linsebigler, A. L.; Lu, G.; Yates, J. T. *Chem. Rev.* **1995**, *95*, 735.
- (29) Mo, S.; Ching, W. *Phys. Rev. B* **1995**, *51*, 13023.
- (30) Norotsky, A.; Jamieson, J. C.; Kleppa, O. J. *Science* **1967**, *158*, 338.
- (31) Hu, Y.; Tsai, H. L.; Huang, C. L. *Mater. Sci. Eng., A* **2003**, *344*, 209.
- (32) Yang, S. R.; Wang, Z. C.; Wang, K. *Semicond. Mater.* **2004**.
- (33) Ruiz, A. M.; Sakaib, G.; Corneta, A.; Shimanoe, K.; Morante, J. R.; Yamazoe, N. *Sens. Actuators, B* **2003**, *93*, 509.
- (34) Tanaka, K.; Capule, M. F. V.; Hisanaga, T. *Chem. Phys. Lett.* **1991**, *187*, 73.
- (35) Li, G.; Chen, L.; Graham, M. E. *J. Mol. Catal. A: Chem.* **2007**, *275*, 30.
- (36) Mathur, S.; Erdem, A.; Cavalius, C.; Barth, S.; Altmayer, J. *Sens. Actuators, B* **2009**, *136*, 432.
- (37) Durrant, J. R. *Anal. Chem.* **1998**, *70*, 5111.
- (38) Kurokawa, Y.; Sano, T.; Ohta, H.; Nakagawa, Y. *Biotechnol. Bioeng.* **1993**, *42*, 394.
- (39) Kennedy, J. F.; Kay, I. M. *J. Chem. Soc., Perkin Trans.* **1976**, *1*, 329.
- (40) Chemseddine, A.; Moritz, T. *Eur. J. Inorg. Chem.* **1999**, 235.
- (41) Sugimoto, T.; Okada, K.; Itoh, H. *J. Colloid Interface Sci.* **1997**, *193*, 140.
- (42) Zhang, H.; Banfield, J. F. *J. Mater. Chem.* **1998**, *8*, 2073.
- (43) Lei, Y.; Zhang, L. D.; Fan, J. C. *Chem. Phys. Lett.* **2001**, *338*, 231.
- (44) Liu, S.; Huang, K. *Sol. Energy Mater. Sol. Cells* **2004**, *85*, 125.
- (45) Zhu, Y.; Li, H.; Koltypin, Y.; Hacohen, Y. R.; Gedanken, A. *Chem. Commun.* **2001**, 2616.
- (46) Hong, S. S.; Lee, M. S.; Park, S. S.; Lee, G. D. *Catal. Today* **2003**, *87*, 99.
- (47) Zhang, D.; Qi, L.; Ma, J.; Cheng, H. *J. Mater. Chem.* **2002**, *12*, 3677.
- (48) Lin, J.; Lin, Y.; Liu, P.; Meziani, M. J.; Allard, L. F.; Sun, Y. P. *J. Am. Chem. Soc.* **2002**, *124*, 11514.
- (49) Seifried, S.; Winterer, M.; Hahn, H. *Chem. Vap. Deposition* **2000**, *6*, 239.
- (50) Pradhan, S. K.; Reucroft, P. J.; Yang, F.; Dozier, A. *J. Cryst. Growth* **2003**, *256*, 83.
- (51) Wu, J. J.; Yu, C. C. *J. Phys. Chem. B* **2004**, *108*, 3377.
- (52) Wu, J. M.; Shih, H. C.; Wu, W. T. *Chem. Phys. Lett.* **2005**, *413*, 490.
- (53) Wu, J. M.; Shih, H. C.; Wu, W. T.; Tseng, Y. K.; Chen, I. C. *J. Cryst. Growth* **2005**, *281*, 384.
- (54) Xiang, B.; Zhang, Y.; Wang, Z.; Luo, X. H.; Zhu, Y. W.; Zhang, H. Z.; Yu, D. P. *J. Phys. D* **2005**, *38*, 1152.
- (55) Peng, X.; Chen, A. *J. Mater. Chem.* **2004**, *14*, 2542.
- (56) Varghese, O. K.; Gong, D.; Paulose, M.; Ong, K. G.; Dickey, E. C.; Grimes, C. A. *Adv. Mater.* **2003**, *15*, 624.
- (57) Mor, G. K.; Varghese, O. K.; Paulose, M.; Shankar, K.; Grimes, C. A. *Sol. Energy Mater. Sol. Cells* **2006**, *90*, 2011.
- (58) Grimes, C. A. *J. Mater. Chem.* **2007**, *17*, 1451.
- (59) Mor, G. K.; Shankar, K.; Paulose, M.; Varghese, O. K.; Grimes, C. A. *Nano Lett.* **2006**, *6*, 215.
- (60) Mor, G. K.; Shankar, K.; Paulose, M.; Varghese, O. K.; Grimes, C. A. *Nano Lett.* **2005**, *5*, 191.
- (61) Bauer, S.; Kleber, S.; Schmuki, P. *Electrochem. Commun.* **2006**, *8*, 1321.
- (62) Macak, J. M.; Tsuchiya, H.; Ghicov, A.; Yasuda, K.; Hahn, R.; Bauer, S.; Schmuki, P. *Curr. Opin. Solid State Mater. Sci.* **2007**, *11*, 3.
- (63) Ghicov, A.; Schmuki, P. *Chem. Commun.* **2009**, *20*, 2791.
- (64) Kowalski, D.; Kim, D.; Schmuki, P. *Nano Today* **2013**, *8*, 235.
- (65) Macák, J. M.; Tsuchiya, H.; Schmuki, P. *Angew. Chem., Int. Ed.* **2005**, *44*, 2100.
- (66) Roy, P.; Berger, S.; Schmuki, P. *Angew. Chem., Int. Ed.* **2011**, *50*, 2904.
- (67) Yasuda, K.; Macak, J. M.; Berger, S.; Ghicov, A.; Schmuki, P. *J. Electrochem. Soc.* **2007**, *154*, C472.
- (68) Albu, S. P.; Kim, D.; Schmuki, P. *Angew. Chem., Int. Ed.* **2008**, *47*, 1916.
- (69) Kim, D.; Ghicov, A.; Albu, S. P.; Schmuki, P. *J. Am. Chem. Soc.* **2008**, *130*, 16454.
- (70) Albu, S. P.; Ghicov, A.; Aldabergenova, S.; Drechsel, P.; LeClere, D.; Thompson, G. E.; Macak, J. M.; Schmuki, P. *Adv. Mater.* **2008**, *20*, 4135.
- (71) Song, Y. Y.; Schmidt-Stein, F.; Bauer, S.; Schmuki, P. *J. Am. Chem. Soc.* **2009**, *131*, 4230.
- (72) Berger, S.; Tsuchiya, H.; Schmuki, P. *Chem. Mater.* **2008**, *20*, 3245.
- (73) Tsuchiya, H.; Berger, S.; Macak, J. M.; Ghicov, A.; Schmuki, P. *Electrochem. Commun.* **2007**, *9*, 2397.
- (74) Ghicov, A.; Aldabergenova, S.; Tsuchiya, H.; Schmuki, P. *Angew. Chem., Int. Ed.* **2006**, *45*, 6993.
- (75) Yasuda, K.; Schmuki, P. *Electrochem. Commun.* **2007**, *9*, 615.
- (76) Yasuda, K.; Schmuki, P. *Electrochim. Acta* **2007**, *52*, 4053.
- (77) Macak, J. M.; Tsuchiya, H.; Taveira, L.; Ghicov, A.; Schmuki, P. *J. Biomed. Mater. Res., Part A* **2005**, *75A*, 928.
- (78) Tsuchiya, H.; Macak, J. M.; Ghicov, A.; Tang, Y. C.; Fujimoto, S.; Niinomi, M.; Noda, T.; Schmuki, P. *Electrochim. Acta* **2006**, *52*, 94.
- (79) Tsuchiya, H.; Macak, J. M.; Ghicov, A.; Schmuki, P. *Small* **2006**, *2*, 888.

- (80) Yang, J.; Mei, S.; Ferreira, J. M. F. *Mater. Sci. Eng., C* **2001**, *C15*, 183.
- (81) Feng, X.; Zhai, J.; Jiang, L. *Angew. Chem., Int. Ed.* **2005**, *44*, 5115.
- (82) Armstrong, A. R.; Armstrong, G.; Canales, J.; García, R.; Bruce, P. G. *Adv. Mater.* **2005**, *7*, 862.
- (83) Tétreault, N.; Horváth, E.; Moehl, T.; Brillet, J.; Smajda, R.; Bungener, S.; Cai, N.; Wang, P.; Zakeeruddin, S. M.; Forró, L.; Magrez, A.; Grätzel, M. *Nano* **2010**, *4*, 7644.
- (84) Liu, B.; Aydil, E. S. *J. Am. Chem. Soc.* **2009**, *131*, 3985.
- (85) Cho, I. S.; Chen, Z.; Forman, A. J.; Kim, D. R.; Rao, P. M.; Jaramillo, T. F.; Zheng, X. *Nano Lett.* **2011**, *11*, 4978.
- (86) Wu, N. Q.; Tafen, D. N.; Wang, H.; Zheng, J. G.; Lewis, J. P.; Liu, X. G.; Leonard, S. S.; Manivannan, A. *J. Am. Chem. Soc.* **2010**, *132*, 6679.
- (87) Sun, Z.; Kim, J. H.; Zhao, Y.; Bijarbooneh, F.; Malgras, V.; Lee, Y.; Kang, Y.-M.; Dou, S. X. *J. Am. Chem. Soc.* **2011**, *133*, 19314.
- (88) Yang, H. G.; Liu, G.; Qiao, S. Z.; Sun, C. H.; Jin, Y. G.; Smith, S. C.; Zou, J.; Cheng, H. M.; Lu, G. Q. *J. Am. Chem. Soc.* **2009**, *131*, 4078.
- (89) Xu, C.; Gao, D. *J. Phys. Chem. C* **2012**, *116*, 7236.
- (90) Qiu, J. J.; Yu, W. D.; Gao, X. D.; Li, X. M. *Nanotechnology* **2006**, *17*, 4695.
- (91) Yu, Y.; Yin, X.; Kvit, A.; Wang, X. *Nano Lett.* **2014**, online, DOI: 10.1021/nl5002907.
- (92) Li, Z.; Yao, C.; Yu, Y.; Cai, Z.; Wang, X. *Adv. Mater.* **2014**, online, DOI: 10.1002/adma.201303369.
- (93) Shi, J.; Hara, Y.; Sun, C.; Anderson, M. A.; Wang, X. *Nano Lett.* **2011**, *11*, 3413.
- (94) Yang, P.; Zhao, D.; Margolese, D. I.; Chmelka, B. F.; Stucky, G. D. *Nature* **1998**, *396*, 152.
- (95) Holland, B. T.; Blanford, C.; Stein, A. *Science* **1998**, *281*, 538.
- (96) Dong, W.; Bongard, H.; Tesche, B.; Marlow, F. *Adv. Mater.* **2002**, *14*, 1457.
- (97) Dong, W.; Marlow, F. *Phys. E* **2003**, *17*, 431.
- (98) Chen, J. L.; Freymann, G. V.; Kitaev, V.; Ozin, G. A. *J. Am. Chem. Soc.* **2007**, *129*, 1196.
- (99) Kwak, E. S.; Lee, W.; Park, N. G.; Kim, J. K.; Lee, H. J. *Adv. Funct. Mater.* **2009**, *19*, 1093.
- (100) Knezl, M.; Nielsch, K.; Niinistö, L. *Adv. Mater.* **2007**, *19*, 3425.
- (101) King, J. S.; Graugnard, E.; Summers, C. J. *Adv. Mater.* **2005**, *17*, 1010.
- (102) Wang, X. D.; Graugnard, E.; King, J. S.; Wang, Z. L.; Summers, C. *Nano Lett.* **2004**, *4*, 2223.
- (103) Tetreault, N.; Arsénault, E.; Heiniger, L.-P.; Soheilnia, N.; Brillet, J.; Moehl, T.; Zakeeruddin, S.; Ozin, G. A.; Grätzel, M. *Nano Lett.* **2011**, *11*, 4579.
- (104) Crossland, E. J. W.; Noel, N.; Sivaram, V.; Leijtens, T.; Alexander-Webber, J. A.; Snaith, H. J. *Nature* **2013**, *495*, 215.
- (105) Kim, H.; Hong, M. H.; Jang, H. W.; Yoon, S. J.; Park, H. H. *Thin Solid Films* **2013**, *529*, 89.
- (106) Wang, B.; Zhao, Y.; Hu, L.; Cao, J.; Gao, F.; Liu, Y.; Wang, L. *Chin. Sci. Bull.* **2010**, *55*, 228.
- (107) Varghese, O. K.; Mor, G. K.; Grimes, C. A.; Paulose, M.; Mukherjee, N. J. *Nanosci. Nanotechnol.* **2004**, *4*, 733.
- (108) Li, Y. J.; Ma, M. J.; Zhu, J. J. *Anal. Chem.* **2012**, *84*, 10492.
- (109) Gao, H.; Sun, M.; Lin, C.; Wang, S. *Electroanalysis* **2012**, *24*, 2283.
- (110) Zhuo, Y.; Chai, Y. Q.; Yuan, R.; Mao, L.; Yuan, Y. L. *Biosens. Bioelectron.* **2011**, *26*, 3838.
- (111) Wei, N.; Xin, X.; Du, J.; Li, J. *Biosens. Bioelectron.* **2011**, *26*, 3602.
- (112) Göpel, W.; Schierbaum, K. *Sens. Actuators, B* **1995**, *26/27*, 1.
- (113) Williams, D. *Sens. Actuators, B* **1999**, *57*, 1.
- (114) Draper, R. B.; Fox, M. A. *J. Phys. Chem.* **1990**, *94*, 4628.
- (115) Geng, P.; Zheng, J. H.; Zhang, X. N.; Wang, Q. J.; Zhang, W.; Jin, L. T.; Feng, Z.; Wu, Z. R. *Electrochem. Commun.* **2007**, *9*, 2162.
- (116) Díaz, V.; Ibáñez, R.; Gímez, P.; Urtiaga, A. M.; Ortiz, I. *Water Res.* **2011**, *45*, 125.
- (117) Chen, H. Y. *Environ. Expl.* **2000**, *15*, 47.
- (118) Baker, J. R.; Mark, M. W.; Mihelcic, J. R. *Water Res.* **1999**, *33*, 327.
- (119) Lee, K. H.; Ishikawa, T.; Mcniven, S. J.; Nomura, Y.; Hiratsuka, A.; Sasaki, S.; Arikawa, Y.; Karube, I. *Anal. Chim. Acta* **1999**, *398*, 161.
- (120) Qiu, J. X.; Zhang, S. Q.; Zhao, H. J. *J. Hazard. Mater.* **2012**, *211–212*, 381.
- (121) Jiang, D.; Zhao, H.; Zhang, S.; John, R. J. *Phys. Chem. B* **2003**, *107*, 12774.
- (122) Bai, J.; Li, J. H.; Liu, Y. B.; Zhou, B. X. *Appl. Catal., B* **2010**, *95*, 408.
- (123) Jiang, D.; Zhao, H. J.; Zhang, S.; John, R.; Will, G. D. J. *Photochem. Photobiol., A* **2003**, *156*, 201.
- (124) Lowe, C. R. *Trends Biotechnol.* **1984**, *2*, 59.
- (125) Chaubey, A.; Malhotra, B. D. *Biosens. Bioelectron.* **2002**, *17*, 441.
- (126) Mathur, S.; Erdem, A.; Cavelius, C.; Barth, S.; Altmayer, J. *Sens. Actuators, B* **2009**, *136*, 432.
- (127) Durrant, J. R. *Anal. Chem.* **1998**, *70*, 5111.
- (128) Eggins, B. *Chemical Sensors and Biosensors. Analytical Techniques in the Sciences*; John Wiley & Sons: West Sussex, 2002.
- (129) Varghese, O. K.; Gong, D.; Paulose, M.; Ong, K. G.; Grimes, C. A. *Sens. Actuators, B* **2003**, *93*, 338.
- (130) Zuruzi, A. S.; MacDonald, N. C.; Moskovits, M.; Kolmakov, A. *Angew. Chem., Int. Ed.* **2007**, *46*, 4298.
- (131) Munuera, G.; González-Elipe, A. R.; Muñoz, A.; Fernández, A. *Sens. Actuators* **1989**, *18*, 337.
- (132) Göpel, W.; Kirner, U.; Wiemhöfer, H. D.; Rocker, G. *Solid State Ionics* **1988**, *28–30*, 1423.
- (133) Akbar, S. A.; Younkman, L. B.; Dutta, P. K. *Sensor* **1998**, *690*, 161.
- (134) Mather, G. C.; Marques, F. M. B.; Frade, J. R. J. *Eur. Ceram. Soc.* **1999**, *19*, 887.
- (135) Jun, Y. K.; Kim, H. S.; Lee, J. H.; Hong, S. H. *Sens. Actuators, B* **2005**, *107*, 264.
- (136) Devi, G. S.; Hyodo, T.; Shimizu, Y.; Egashira, M. *Sens. Actuators, B* **2002**, *87*, 122.
- (137) Shimizu, Y.; Kuwano, N.; Hyodo, T.; Egashira, M. *Sens. Actuators, B* **2002**, *83*, 195.
- (138) Shimizu, Y.; Hyodo, T.; Egashira, M. *Sens. Actuators, B* **2007**, *121*, 219.
- (139) Iwanaga, T.; Hyodo, T.; Shimizu, Y.; Egashira, M. *Sens. Actuators, B* **2003**, *93*, 519.
- (140) Mor, G. K.; Varghese, O. K.; Paulose, M.; Shankar, K.; Grimes, C. A. *Sol. Energy Mater. Sol. Cells* **2006**, *90*, 2011.
- (141) Varghese, O. K.; Gong, D. W.; Paulose, M.; Ong, K. G.; Dickey, E. C.; Grimes, C. A. *Adv. Mater.* **2003**, *15*, 624.
- (142) Khameneh Asl, S.; Alavi, B.; Ahmadi, S. *Surf. Interface Anal.* **2012**, *44*, 1051.
- (143) Chen, K.; Xie, K.; Feng, X.; Wang, S.; Hu, R.; Gu, H.; Li, Y. *Int. J. Hydrogen Energy* **2012**, *37*, 13602.
- (144) Yoriya, S.; Prakasam, H. E.; Varghese, O. K.; Shankar, K.; Paulose, M.; Mor, G. K.; Latempa, T. J.; Grimes, C. A. *Sens. Lett.* **2006**, *4*, 334.
- (145) Jia, W.; Su, L.; Ding, Yu.; Schempf, A.; Wang, Y.; Lei, Yu. J. *Phys. Chem. C* **2009**, *113*, 16402.
- (146) Carney, C. M.; Yoo, S.; Akbar, S. A. *Sens. Actuators, B* **2005**, *108*, 29.
- (147) Monkowski, A. J.; Morrill, A.; MacDonald, N. C. *J. Electrochem. Soc.* **2008**, *155*, J297.
- (148) Rout, C. S.; Kulkarni, G. U.; Rao, C. N. R. *J. Phys. D: Appl. Phys.* **2007**, *40*, 2777.
- (149) De Luca, L.; Donato, A.; Santangelo, S.; Faggio, G.; Messina, G.; Donato, N.; Neri, G. *Int. J. Hydrogen Energy* **2012**, *37*, 1842.
- (150) Ampelli, C.; Spadaro, D.; Neri, G.; Donato, N.; Latino, M.; Passalacqua, R.; Perathoner, S.; Centi, G. *Chem. Eng. Trans.* **2012**, *26*, 333.
- (151) Hazra, S. K.; Basu, S. *Sens. Actuators, B* **2006**, *115*, 403.
- (152) Imawan, C.; Solzbacher, F.; Steffes, H.; Obermeier, E. *Sens. Actuators, B* **2000**, *68*, 184.

- (153) Buso, D.; Post, M.; Cantalini, C.; Mulvaney, P.; Martucci, A. *Adv. Funct. Mater.* **2008**, *18*, 3843.
- (154) Shastri, A. G.; Schwank, J. *Appl. Surf. Sci.* **1987**, *29*, 341.
- (155) Munuera, G.; González-Elipé, A. R.; Muñoz, A.; Fernández, A.; Soria, J.; Conesa, J.; Sanz, J. *Sens. Actuators* **1989**, *18*, 337.
- (156) Kobayashi, H.; Kishimoto, K.; Nakato, Y.; Tsubomura, H. *Sens. Actuators, B* **1993**, *13*, 125.
- (157) Walton, R. M.; Liu, H.; Gland, J. L.; Schwank, J. W. *Sens. Actuators, B* **1997**, *41*, 143.
- (158) Mor, G. K.; Varghese, O. K.; Paulose, M.; Ong, K. G.; Grimes, C. A. *Thin Solid Films* **2006**, *496*, 42.
- (159) Madou, M. J.; Morrison, S. R. *Chemical Sensing with Solid State Devices*; Academic Press Inc.: London, 1989; ISBN-10: 0124649653.
- (160) Diebold, U. *Surf. Sci. Rep.* **2003**, *48*, 53.
- (161) Xu, Y.; Zhou, X.; Toft Sørensen, O. *Sensors. Actuators, B* **2000**, *65*, 2.
- (162) Della Gaspera, E.; Guglielmi, M.; Agnoli, S.; Granozzi, G.; Post, M. L.; Bello, V.; Mattei, G.; Martucci, A. *Chem. Mater.* **2010**, *22*, 3407.
- (163) Liu, H.; Ding, D.; Ning, C.; Li, Z. *Nanotechnology* **2012**, *23*, 015502.
- (164) Li, Z.; Ding, D.; Ning, C. *Nanoscale Res. Lett.* **2013**, *8*, 1.
- (165) Morimoto, T.; Nagao, M.; Tokuda, F. *J. Phys. Chem.* **1969**, *73*, 243.
- (166) Şennik, E.; Çolak, Z.; Kiliç, N.; Öztürk, Z. *Int. J. Hydrogen Energy* **2010**, *35*, 4420.
- (167) Du, X.; Wang, Y.; Mu, Y.; Gui, L.; Wang, P.; Tang, Y. *Chem. Mater.* **2002**, *14*, 3953.
- (168) Kolmakov, A.; Zhang, Y.; Cheng, G.; Moskovits, M. *Adv. Mater.* **2003**, *15*, 997.
- (169) Wang, R.; Okajima, T.; Kitamura, F.; Ohsaka, T. *Electroanalysis* **2004**, *16*, 66.
- (170) Liu, Z.; Yamazaki, T.; Shen, Y.; Kikuta, T.; Nakatani, N.; Li, Y. *Sens. Actuators, B* **2008**, *129*, 666.
- (171) Fryberger, T. B.; Semancik, S. *Sens. Actuators, B* **1990**, *2*, 305.
- (172) Shie, J.-W.; Yogeswaran, U.; Chen, S.-M. *Talanta* **2009**, *78*, 896.
- (173) *Ceram. Bull.* **1975**, *54*, 280.
- (174) Kaiser, W. J.; Logothetis. *SAE Tech. Paper* **1983**, no. 830167.
- (175) Howarth, D. S.; Micheli, A. L. *SAE Tech. Paper* **1984**, no. 840140.
- (176) Takami, A.; Matsuura, T.; Miyata, S.; Furusaki, K.; Watanabe, Y. *SAE Tech. Paper* **1987**, no. 870290.
- (177) Tien, T. Y.; Stadler, H. L. *Ceram. Bull.* **1975**, *54*, 280.
- (178) Micheli, A. L. *Am. Ceram. Soc. Bull.* **1984**, *63*, 694.
- (179) Takami, A. *Am. Ceram. Soc. Bull.* **1988**, *67*, 1956.
- (180) Lu, C. C.; Huang, Y. S.; Huang, J. W.; Chang, C. K.; Wu, S. P. *Sensors* **2010**, *10*, 670.
- (181) Zuruzi, A. S.; Kolmakov, A.; MacDonald, N. C.; Moskovits, M. *Appl. Phys. Lett.* **2006**, *88*, 102904.
- (182) Zhou, Z.; Shinar, R.; Allison, A. J.; Shinar, J. *Adv. Funct. Mater.* **2007**, *17*, 3530.
- (183) Lu, H. F.; Li, F.; Liu, G.; Chen, Z. G.; Wang, D. W.; Fang, H. T.; Lu, G. Q.; Jiang, Z. H.; Cheng, H. M. *Nanotechnology* **2008**, *19*, 405504.
- (184) Li, X.; Ramasamy, R.; Dutta, P. K. *Sens. Actuators, B* **2009**, *143*, 308.
- (185) Yang, M.; Li, L. *Sens. Actuators, B* **2010**, *147*, 622.
- (186) Huyen, D. N.; Tung, N. T.; Thien, N. D.; Le Thanh, H. *Sensors* **2011**, *11*, 1924.
- (187) Wu, M. T.; Yao, X.; Yuan, Z. H.; Sun, H. T.; Wu, W. C.; Chen, Q. H.; Xu, G. Y. *Sens. Actuators, B* **1993**, *B14*, 491.
- (188) Xu, Y.; Yao, K.; Zhou, X.; Cao, Q. *Sens. Actuators, B* **1993**, *14*, 492.
- (189) Patel, S. V.; Wise, K. D. *Sens. Actuators, B* **1997**, *42*, 205.
- (190) Francioso, L.; Presicce, D. S.; Siciliano, P.; Ficarella, A. *Sens. Actuators, B* **2007**, *123*, 516.
- (191) Castañeda, L. *Mater. Sci. Eng., B* **2007**, *139*, 149.
- (192) Li, M.; Chen, Y. *Sens. Actuators, B* **1996**, *32*, 83.
- (193) Sharma, R. K.; Bhatnagar, M. C.; Sharma, G. L. *Sens. Actuators, B* **1997**, *45*, 209.
- (194) Comini, E.; Sberveglieri, G.; Ferroni, M.; Guidi, V.; Martinelli, G. *Sens. Actuators, B* **2003**, *93*, 409.
- (195) Ruiz, A. M.; Cornet, A.; Morante, J. R. *Sens. Actuators, B* **2004**, *100*, 256.
- (196) Bonini, N.; Carotta, M. C.; Chiorino, A.; Guidi, V.; Malagù, C.; Martinelli, G.; Paglialonga, L.; Sacerdoti, M. *Sens. Actuators, B* **2000**, *68*, 274.
- (197) Comini, E.; Sberveglieri, G.; Ferroni, M.; Guidi, V.; Martinelli, G. *Sens. Actuators, B* **2003**, *93*, 409.
- (198) Sharma, R. K.; Bhatnagar, M. C. *Sens. Actuators, B* **1999**, *56*, 215.
- (199) Sharma, R. K.; Bhatnagar, M. C.; Sharma, G. L. *Sens. Actuators, B* **1998**, *46*, 194.
- (200) Sotter, E.; Vilanova, X.; Llobet, E.; Vasiliev, A.; Correig, X. *Sens. Actuators, B* **2007**, *127*, 567.
- (201) Zhuiykov, S.; Wlodarski, W.; Li, Y. *Sens. Actuators, B* **2001**, *77*, 484.
- (202) Frank, M. L.; Fulkerson, M. D.; Patton, B. R.; Dutta, P. K. *Sens. Actuators, B* **2002**, *87*, 471.
- (203) Trinchì, A.; Li, Y. X.; Wlodarski, W.; Kaciulis, S.; Pandolfi, L.; Viticoli, S.; Comini, E.; Sberveglieri, G. *Sens. Actuators, B* **2003**, *95*, 145.
- (204) Rajabbeigi, N.; Elyassi, B.; Khodadadi, A. A.; Mohajerzadeh, S.; Mortazavi, Y.; Sahimi, M. *Sens. Actuators, B* **2005**, *108*, 341.
- (205) Lee, H. C.; Hwang, W. S. *Appl. Surf. Sci.* **2006**, *253*, 1889.
- (206) Llobet, E.; Espinosa, E. H.; Sotter, E.; Ionescu, R.; Vilanova, X.; Torres, J.; Felten, A.; Pireaux, J. J.; Ke, X.; Van Tendeloo, G.; Renaux, F.; Paint, Y.; Hecq, M.; Bittencourt, C. *Nanotechnology* **2008**, *19*, 375501.
- (207) Wang, Q.; Guo, X.; Cai, L.; Cao, Y.; Gan, L.; Liu, S.; Wang, Z.; Zhang, H.; Li, L. *Chem. Sci.* **2011**, *2*, 1860.
- (208) McCafferty, E.; Zettlemoyer, A. C. *Faraday Discuss.* **1971**, *52*, 239.
- (209) Thorp, J. M. *Trans. Faraday Soc.* **1959**, *55*, 442.
- (210) Ansbacher, F.; Jason, A. C. *Nature* **1953**, *24*, 177.
- (211) Yu, J.; Zhao, X.; Zhao, Q.; Wang, G. *Mater. Chem. Phys.* **2001**, *68*, 253.
- (212) Nitta, T.; Terada, Z.; Hayakawa, S. *J. Am. Ceram. Soc.* **1980**, *63*, 295.
- (213) Wu, R. J.; Sun, Y. L.; Lin, C. C.; Chen, H. W.; Chavali, M. *Sens. Actuators, B* **2006**, *115*, 198.
- (214) Zhang, Y.; Fu, W.; Yang, H.; Qi, Q.; Zeng, Y.; Zhang, T.; Ge, R.; Zou, G. *Appl. Surf. Sci.* **2008**, *254*, 5545.
- (215) Li, Z. Y.; Zhang, H. N.; Zheng, W.; Wang, W.; Huang, H. M.; Wang, C.; MacDiarmid, A. G.; Wei, Y. *J. Am. Chem. Soc.* **2008**, *130*, 5036.
- (216) Yadav, B. C.; Pandey, N. K.; Srivastava, A. K.; Sharma, P. *Meas. Sci. Technol.* **2007**, *18*, 260.
- (217) Wang, Z.; Shi, L.; Wu, F.; Yuan, S.; Zhao, Y.; Zhang, M. *Nanotechnology* **2011**, *22*, 275502.
- (218) Faia, P. M.; Furtado, C. S.; Ferreira, A. J. *Sens. Actuators, B* **2004**, *101*, 183.
- (219) Ying, J.; Wan, C.; He, P. *Sens. Actuators, B* **2000**, *62*, 165.
- (220) Sluneko, J.; Holc, J.; Kosec, M.; Kolar, D. *Electron. Comp. Mater.* **1996**, *26*, 285.
- (221) Jain, M. K.; Bhatnagar, M. C.; Sharma, G. L. *Sens. Actuators, B* **1999**, *55*, 180.
- (222) Tai, W.; Oh, J. *Sens. Actuators* **2002**, *B 85*, 154.
- (223) Tai, W.; Kim, J.; Oh, J. *Sens. Actuators, B* **2003**, *96*, 477.
- (224) Niranjana, R. S.; Sathaye, S. D.; Mulla, I. S. *Sens. Actuators, B* **2001**, *81*, 64.
- (225) Li, H.; Shi, Z.; Liu, H. *J. Rare Earth* **2010**, *28*, 23.
- (226) Tai, W. P.; Kim, J. G.; Oh, J. H.; Lee, C.; Park, D. W.; Ahn, W. S. *J. Mater. Sci.: Mater. Electron.* **2005**, *16*, 517.
- (227) Sun, A.; Huang, L.; Li, Y. *Sens. Actuators, B* **2009**, *139*, 543.
- (228) Su, P. G.; Chang, Y. P. *Sens. Actuators, B* **2008**, *129*, 915.
- (229) Su, P. G.; Wang, C. P. *Sens. Actuators, B* **2008**, *129*, 538.



- (230) Su, P. G.; Huang, L. N. *Sens. Actuators, B* **2007**, *123*, 501.
- (231) Makita, K.; Nogami, M.; Abe, Y. *J. Mater. Sci. Lett.* **1997**, *16*, 550.
- (232) Traversa, E.; Gnappi, G.; Montenero, A.; Gusmano, G. *Sens. Actuators, B* **1996**, *31*, 59.
- (233) Grimes, C. A.; Kouzoudis, D.; Dickey, E.; Qian, D.; Anderson, M. A.; Shahidain, R.; Lindsey, M.; Green, L. *J. Appl. Phys.* **2000**, *87*, 5341.
- (234) Mukundan, R.; Garzon, F. *Electrochem. Soc. Interface* **2004**, *13*, 30.
- (235) Teleki, A.; Bjelobrk, N.; Pratsinis, S. E. *Sens. Actuators, B* **2008**, *130*, 367.
- (236) Seeley, Z. M.; Bandyopadhyay, A.; Bose, S. *Mater. Sci. Eng., B* **2009**, *164*, 38.
- (237) Liu, X.; Ling, Y.; Huang, L.; Gao, W. *J. Nanosci. Nanotechnol.* **2013**, *13*, 869.
- (238) Lee, J. S.; Ha, T. J.; Hong, M. H.; Park, H. H. *Thin Solid Films* **2013**, *529*, 98.
- (239) Lee, J. S.; Ha, T. J.; Hong, M. H.; Park, C. S.; Park, H. H. *Appl. Surf. Sci.* **2013**, *269*, 125.
- (240) Kim, H.; Hong, M. H.; Jang, H. W.; Yoon, S. J.; Park, H. H. *Thin Solid Films* **2013**, *529*, 89.
- (241) Wang, B.; Zhao, Y.; Hu, L.; Cao, J.; Gao, F.; Liu, Y.; Wang, L. *Chin. Sci. Bull.* **2010**, *55*, 228.
- (242) Park, J.; Moon, J.; Lee, S. J.; Kim, S. H.; Zyung, T.; Chu, H. Y. *Mater. Lett.* **2010**, *64*, 255.
- (243) Moon, H. G.; Shim, Y. S.; Jang, H. W.; Kim, J. S.; Choi, K. J.; Kang, C. Y.; Choi, J. W.; Park, H. H.; Yoon, S. J. *Sens. Actuators, B* **2010**, *149*, 116.
- (244) Jun, Y. K.; Kim, H. S.; Lee, J. H.; Hong, S. H. *Sens. Actuators, B* **2006**, *120*, 69.
- (245) Comini, E.; Guidi, V.; Frigeri, C.; Riccò, I.; Sberveglieri, G. *Sens. Actuators, B* **2001**, *77*, 16.
- (246) Park, J. Y.; Azad, A. M.; Song, S. J.; Wachsmann, E. D. *J. Am. Ceram. Soc.* **2010**, *93*, 742.
- (247) Lee, J. S.; Ha, T. J.; Hong, M. H.; Park, C. S.; Park, H. H. *Appl. Surf. Sci.* **2013**, *269*, 125.
- (248) Ram, M. K.; Yavuz, O.; Lahsangah, V.; Aldissi, M. *Sens. Actuators, B* **2005**, *106*, 750.
- (249) Ruiz, A. M.; Cornet, A.; Shimanoe, K.; Morante, J. R.; Yamazoe, N. *Sens. Actuators, B* **2005**, *109*, 7.
- (250) Dutta, P. K.; Frank, M.; Hunter, G. W.; George, M. *Sens. Actuators, B* **2005**, *106*, 810.
- (251) Mendell, M. J. *Indoor Air* **2007**, *17*, 259.
- (252) Skubal, L. R.; Meshkov, N. K.; Vogt, M. C. *J. Photochem. Photobiol., A* **2002**, *148*, 103.
- (253) Taurino, A. M.; Capone, S.; Siciliano, P.; Toccoli, T.; Boschetti, A.; Guerini, L.; Iannotta, S. *Sens. Actuators, B* **2003**, *92*, 292.
- (254) Teleki, A.; Pratsinis, S. E.; Kalyanasundaram, K.; Gouma, P. I. *Sens. Actuators, B* **2006**, *119*, 683.
- (255) Rella, R.; Spadavecchia, J.; Manera, M. G.; Capone, S.; Taurino, A.; Martino, M.; Caricato, A. P.; Tunno, T. *Sens. Actuators, B* **2007**, *127*, 426.
- (256) Si, S. H.; Fung, Y. S.; Zhu, D. R. *Sens. Actuators, B* **2005**, *108*, 165.
- (257) Ding, Y.; Wang, Y.; Zhang, L.; Zhang, H.; Li, C. M.; Lei, Y. *Nanoscale* **2011**, *3*, 1149.
- (258) Seo, M. H.; Yuasa, M.; Kida, T.; Huh, J. S.; Yamazoe, N.; Shimanoe, K. *Sens. Actuators, B* **2011**, *154*, 251.
- (259) Seo, M. H.; Yuasa, M.; Kida, T.; Huh, J. S.; Shimanoe, K.; Yamazoe, N. *Sens. Actuators, B* **2009**, *137*, 513.
- (260) Lin, S.; Li, D.; Wu, J.; Li, X.; Akbar, S. A. *Sens. Actuators, B* **2011**, *156*, 505.
- (261) Wu, G. Q.; Zhang, J. W.; Wang, X. Y.; Liao, J. J.; Xia, H.; Akbar, S. A.; Li, J. B.; Lin, S. W.; Li, X. G.; Wang, J. *Ceram. Int.* **2012**, *38*, 6341.
- (262) Wang, X.; Cui, F.; Lin, J.; Ding, B.; Yu, J.; Al-Deyab, S. S. *Sens. Actuators, B* **2012**, *171–172*, 658.
- (263) Zeng, W.; Liu, T.; Wang, Z.; Tsukimoto, S.; Saito, M.; Ikuhara, Y. *Sensors* **2009**, *9*, 9029.
- (264) Zeng, W.; Tianmo, L. *Phys. B (Amsterdam, Neth.)* **2010**, *405*, 1345.
- (265) Zeng, W.; Liu, T.; Wang, Z. *Physica E* **2010**, *43*, 633.
- (266) Zeng, W.; Liu, T.; Liu, D. *Physica B* **2010**, *405*, 4235.
- (267) Li, S.; Li, F.; Rao, Z. *Sens. Actuators, B* **2010**, *145*, 78.
- (268) Wu, G.; Zhang, J.; Wang, X.; Liao, J.; Xia, H.; Akbar, S. A.; Li, J.; Lin, S.; Li, X.; Wang, J. *Ceram. Int.* **2012**, *38*, 6341.
- (269) Chen, H.; Liu, Y.; Xie, C.; Wu, J.; Zeng, D.; Liao, Y. *Ceram. Int.* **2012**, *38*, 503.
- (270) Liu, L.; Lia, X.; Dutta, P. K.; Wang, J. *Sens. Actuators, B* **2013**, *185*, 1.
- (271) Barreca, D.; Comini, E.; Ferrucci, A. P.; Gasparotto, A.; Maccato, C.; Maragno, C.; Sberveglieri, G.; Tondello, E. *Chem. Mater.* **2007**, *19*, 5642.
- (272) Radecka, M.; Kusior, A.; Lacz, A.; Trenczek-Zajac, A.; Lyson-Sypien, B.; Zakrzewska, K. J. *Therm. Anal. Calorim.* **2012**, *108*, 1079.
- (273) Galatsis, K.; Li, Y. X.; Wlodarski, W.; Comini, E.; Faglia, G.; Sberveglieri, G. *Sens. Actuators, B* **2001**, *77*, 472.
- (274) Wang, Y.; Jia, W.; Strout, T.; Ding, Y.; Lei, Y. *Sensors* **2009**, *9*, 6752.
- (275) Ruiz, A. M.; Sakai, G.; Cornet, A.; Shimanoe, K.; Morante, J. R.; Yamazoe, N. *Sens. Actuators, B* **2003**, *93*, 509.
- (276) Li, Y.; Wlodarski, W.; Galatsis, K.; Moslih, S. H.; Cole, J.; Russo, S.; Rockelmann, N. *Sens. Actuators, B* **2002**, *83*, 160.
- (277) Moon, J.; Park, J. A.; Lee, S. J.; Zyung, T.; Kim, I. D. *Sens. Actuators, B* **2010**, *149*, 301.
- (278) Pawar, S. G.; Patil, S. L.; Chougule, M. A.; Raut, B. T.; Godase, P. R.; Mulik, R. N.; Sen, S.; Patil, V. B. *IEEE Sens. J.* **2011**, *11*, 2980.
- (279) Tai, H.; Jiang, Y.; Xie, G.; Yu, J. *J. Mater. Sci. Technol.* **2010**, *26*, 605.
- (280) Gong, J.; Li, Y.; Hu, Z.; Zhou, Z.; Deng, Y. *J. Phys. Chem. C* **2010**, *114*, 9970.
- (281) Tai, H.; Jiang, Y.; Xie, G.; Yu, J.; Zhao, M. *Int. J. Environ. Anal. Chem.* **2007**, *87*, 539.
- (282) Wu, Y.; Xing, S.; Fu, J. *J. Appl. Polym. Sci.* **2010**, *118*, 3351.
- (283) Lee, S. W.; Takahara, N.; Korposh, S.; Yang, D. H.; Toko, K.; Kuntake, T. *Anal. Chem.* **2010**, *82*, 2228.
- (284) Sánchez, M.; Rincón, M. E. *Sens. Actuators, B* **2009**, *140*, 17.
- (285) Karunakaran, B.; Uthirakumar, P.; Chung, S. J.; Velumani, S.; Suh, E. K. *Mater. Charact.* **2007**, *58*, 680.
- (286) Dhivyaa, P.; Prasad, A. K.; Sridharan, M. *Ceram. Int.* **2013**, in press.
- (287) Waghmare, S. D.; Shinde, D. V.; Zate, M. K.; Konda, R.; Mane, R. S.; Han, S. H. *Scr. Mater.* **2013**, *68*, 735.
- (288) Wang, Y.; Jia, W.; Strout, T.; Schempf, A.; Zhang, H.; Li, B.; Cui, J.; Lei, Y. *Electroanalysis* **2009**, *21*, 1432.
- (289) Jung, J. Y.; Lee, C. S. *J. Ind. Eng. Chem.* **2011**, *17*, 237.
- (290) Wang, Q.; Dong, X.; Pang, Z.; Du, Y.; Xia, X.; Wei, Q.; Huang, F. *Sensors (Switzerland)* **2012**, *12*, 17046.
- (291) Liou, W. J.; Lin, H. M. *China Particuol.* **2007**, *5*, 225.
- (292) Huusko, J.; Lantto, V.; Torvela, H. *Sens. Actuators, B* **1993**, *16*, 245.
- (293) Chaudhari, G. N.; Bambole, D. R.; Bodade, A. B.; Padole, P. R. *J. Mater. Sci.* **2006**, *41*, 4860.
- (294) Garadkar, K. M.; Shirke, B. S.; Hankare, P. P.; Path, D. R. *Sens. Lett.* **2001**, *9*, 526.
- (295) Topalian, Z.; Smulko, J. M.; Niklasson, G. A.; Granqvist, G. G. *J. Phys.: Conf. Ser.* **2007**, *76*.
- (296) Bodade, A. B.; Bende, A. M.; Chaudhari, G. N. *Vacuum* **2008**, *82*, 588.
- (297) Lin, H. M.; Hsu, T. Y.; Tung, C. Y.; Hsu, C. M. *Nanostruct. Mater.* **1995**, *6*, 1001.
- (298) Hwang, S.; Kwon, H.; Chhajed, S.; Byon, J. W.; Baik, J. M.; Im, J.; Oh, S. H.; Jang, H. W.; Yoon, S. J.; Kim, J. K. *Analyst* **2013**, *138*, 443.
- (299) Zhang, Z.; Yuan, Y.; Fang, Y.; Liang, L.; Ding, H.; Jin, L. *Talanta* **2007**, *73*, 523.



- (300) Lee, K. H.; Kim, Y. C.; Suzuki, H.; Ikebukuro, K.; Hashimoto, K.; Karube, I. *Electroanalysis* **2000**, *12*, 1334.
- (301) Kim, Y. C.; Lee, K. H. *Anal. Chem.* **2000**, *72*, 3379.
- (302) Kim, Y. C.; Sasaki, S.; Yano, K.; Ikebukuro, K.; Hashimoto, K.; Karube, I. *Anal. Chim. Acta* **2001**, *432*, 59.
- (303) Ai, S.; Li, J.; Yang, Y.; Gao, M.; Pan, Z.; Jin, L. *Anal. Chim. Acta* **2004**, *509*, 237.
- (304) Li, J.; Li, L.; Zheng, L.; Xian, Y.; Jin, L. *Talanta* **2006**, *68*, 765.
- (305) Wang, H.; Zhong, S.; He, Y.; Song, G. *Sens. Actuators, B* **2011**, *160*, 195.
- (306) Ding, H. C.; Chai, Y. H.; Zhang, Z. H.; Liu, M. C.; Xian, Y. Z.; Pan, Z. S.; Jin, L. T. *Chin. J. Chem.* **2005**, *23*, 1425.
- (307) Zhang, Z.; Yuan, Y.; Fang, Y.; Liang, L.; Ding, H.; Jin, L. *Talanta* **2007**, *73*, 523.
- (308) Zhao, H.; Jiang, D.; Zhang, S.; Catterall, K.; John, R. *Anal. Chem.* **2004**, *76*, 155.
- (309) Fang, Y. J.; Zhang, H. Z.; Yuan, Y.; Ding, H. C.; Jin, L. T. *Modern Sci. Instrum.* **2006**, *4*, 41.
- (310) Li, J.; Zheng, L.; Li, L.; Shi, G.; Xian, Y.; Jin, L. *Electroanalysis* **2006**, *18*, 2251.
- (311) Zheng, Q.; Zhou, B. X.; Bai, J.; Li, L. H.; Jin, Z. J.; Zhang, J. L.; Li, J. H.; Zhu, X. Y. *Adv. Mater.* **2008**, *20*, 1044.
- (312) Chen, H. C.; Zhang, J. L.; Chen, Q. P.; Li, J. H.; Li, D.; Dong, C. P.; Liu, Y. B.; Zhou, B. X.; Shang, S. C.; Cai, W. M. *Anal. Methods* **2012**, *4*, 1790.
- (313) Li, X. J.; Yin, W. P.; Li, J. Y.; Bai, J.; Huang, K.; Li, J. H.; Zhou, B. X. *Water Environ. Res.* **2014**, *86*, 532.
- (314) Quan, X.; Yang, S. G.; Ruan, X. L.; Zhao, H. M. *Environ. Sci. Technol.* **2005**, *39*, 3770.
- (315) Bai, J.; Liu, Y.; Li, J.; Zhou, B.; Zheng, Q.; Cai, W. *Appl. Catal., B: Environ.* **2010**, *98*, 154.
- (316) Li, J.; Zheng, L.; Li, L.; Shi, G.; Xian, Y.; Jin, L. *Electroanalysis* **2006**, *18*, 1014.
- (317) Li, J.; Zheng, L.; Li, L.; Shi, G.; Xian, Y.; Jin, L. *Talanta* **2007**, *72*, 1752.
- (318) Li, J.; Zheng, L.; Li, L.; Shi, G.; Xian, Y.; Jin, L. *Meas. Sci. Technol.* **2007**, *18*, 945.
- (319) Liang, L. H.; Zhang, Z. H.; Yuan, Y.; Zeng, L. P.; Jin, L. T. *Chem. Sens.* **2008**, *28*, 57.
- (320) Zhao, H.; Jiang, D.; Zhang, S.; Catterall, K.; John, R. *Anal. Chem.* **2004**, *76*, 155.
- (321) Zhang, S.; Zhao, H.; Jiang, D.; John, R. *Anal. Chim. Acta* **2004**, *514*, 89.
- (322) Zhang, S.; Jiang, D.; Zhao, H. *Environ. Sci. Technol.* **2006**, *40*, 2363.
- (323) Zhang, S.; Li, L.; Zhao, H. *Environ. Sci. Technol.* **2009**, *43*, 7810.
- (324) Mu, Q.; Li, Y.; Zhang, Q.; Wang, H. *Sens. Actuators, B* **2011**, *155*, 804.
- (325) Yuan, S.; Mao, R.; Li, Y.; Zhang, Q.; Wang, H. *Electrochim. Acta* **2012**, *60*, 347.
- (326) Wang, C.; Wu, J.; Wang, P.; Ao, Y.; Hou, J.; Qian, J. *Anal. Chim. Acta* **2013**, *767*, 141.
- (327) Zhang, J.; Zhou, B.; Zheng, Q.; Li, J.; Bai, J.; Liu, Y.; Cai, W. *Water Res.* **2009**, *43*, 1986.
- (328) Han, Y.; Qiu, J.; Miao, Y.; Han, J.; Zhang, S.; Zhang, H.; Zhao, H. *Anal. Methods* **2011**, *3*, 2003.
- (329) Qu, X.; Tian, M.; Chen, S.; Liao, B.; Chen, A. *Electroanalysis* **2011**, *23*, 1267.
- (330) Wang, C.; Wu, J. C.; Wang, P. F.; Ao, Y. H.; Hou, J.; Qian, J. *Sens. Actuators, B* **2013**, *181*, 1.
- (331) Zhao, L.; Gong, S.; Zhu, L.; Yang, P. *Shiyan Jishu Yu Guanli* **2010**, *27*, 34.
- (332) Li, S. X.; Zheng, F. Y.; Cai, S. J.; Liang, W. J.; Li, Y. C. *Sens. Actuators, B* **2013**, *188*, 280.
- (333) Li, L. H.; Zhang, S. Q.; Li, G. Y.; Zhao, H. J. *Anal. Chim. Acta* **2012**, *754*, 47.
- (334) Ruzicka, J.; Hansen, E. H. *Anal. Chim. Acta* **1975**, *78*, 145.
- (335) Kim, Y. C.; Sasaki, S.; Yano, K.; Ikebukuro, K.; Hashimoto, K.; Karube, I. *Anal. Chem.* **2002**, *74*, 3858.
- (336) Chou, J. C.; Yang, H. Y.; Chen, C. W. *Microelectron. Reliab.* **2010**, *50*, 753.
- (337) Lahav, M.; Kharitonov, A. B.; Katz, O.; Kunitake, T.; Willner, T. *Anal. Chem.* **2001**, *73*, 720.
- (338) Wang, J.; Wang, L.; Sun, Y.; Zhu, X.; Cao, Y.; Wang, X.; Zhang, H.; Song, D. *Colloids Surf., B* **2010**, *75*, 520.
- (339) Song, Y. Y.; Schmidt-Stein, F.; Berger, S.; Schmuki, P. *Small* **2010**, *6*, 1180.
- (340) Lippa, P. B.; Sokoll, L. J.; Chan, D. W. *Clin. Chim. Acta* **2001**, *314*, 1.
- (341) Pei, R. J.; Cheng, Z. L.; Wang, E. K.; Yang, X. R. *Biosens. Bioelectron.* **2001**, *16*, 355.
- (342) Thevenot, D. R.; Toth, K.; Durst, R. A.; Wilson, G. S. *Biosens. Bioelectron.* **2001**, *16*, 121.
- (343) Liu, M.; Zhao, G.; Tang, Y.; Shi, H.; Yang, N. *Chin. J. Chem.* **2013**, *31*, 215.
- (344) Poghosian, A. S. *Sens. Actuators, B* **1997**, *44*, 361.
- (345) Wang, Y.; Xu, H.; Zhang, J.; Li, G. *Sensors* **2008**, *8*, 2043.
- (346) Horenstein, M. N. *Microelectronic circuits and devices*; Prentice Hall: Englewood Cliffs, New Jersey, 1990.
- (347) Chu, Y. M.; Lin, C. C.; Chang, H. C.; Li, C.; Guo, C. *Biosens. Bioelectron.* **2011**, *26*, 2334.
- (348) Sabban, S. Ph.D. Thesis, 2011.
- (349) Bard, A. J.; Dekker, M. *Electrogenerated Chemiluminescence*; Marcel Dekker, Inc.: New York, 2004.
- (350) Valenti, G.; Bruno, C.; Rapino, S.; Fiorani, A.; Jackson, E. A.; Scott, L. T.; Paolucci, F.; Marcaccio, M. *J. Phys. Chem. C* **2010**, *114*, 19467.
- (351) Rampazzo, E.; Bonacchi, S.; Genovese, D.; Juris, R.; Marcaccio, M.; Montalti, M.; Paolucci, F.; Sgarzi, M.; Valenti, G.; Zaccaroni, N.; Prodi, L. *Coord. Chem. Rev.* **2012**, *256*, 1664.
- (352) Xu, X.; Zhao, J.; Jiang, D.; Kong, J.; Liu, B.; Deng, J. *Anal. Bioanal. Chem.* **2002**, *374*, 1261.
- (353) Yu, J.; Ju, H. *Anal. Chem.* **2002**, *74*, 3579.
- (354) Yu, J.; Ju, H. *Anal. Chim. Acta* **2003**, *486*, 209.
- (355) Yu, J.; Liu, S.; Ju, H. *Biosens. Bioelectron.* **2003**, *19*, 509.
- (356) Chen, J.; Yan, F.; Dai, Z.; Ju, H. *Biosens. Bioelectron.* **2005**, *21*, 330.
- (357) Chen, X.; Yang, Z.; Si, S. J. *Electroanal. Chem.* **2009**, *635*, 1.
- (358) Cheng, J.; Di, J.; Hong, J.; Yao, K.; Sun, Y.; Zhuang, J.; Xu, Q.; Zheng, H.; Bi, S. *Talanta* **2008**, *76*, 1065.
- (359) Liang, R.; Jiang, J.; Qiu, J. *Anal. Sci.* **2008**, *24*, 1425.
- (360) Cao, H.; Zhu, Y.; Tang, L.; Yang, X.; Li, C. *Electroanalysis* **2008**, *20*, 2223.
- (361) Choi, H. N.; Kim, M. A.; Lee, W. Y. *Anal. Chim. Acta* **2005**, *537*, 179.
- (362) Li, Q.; Luo, G.; Feng, J.; Zhou, Q.; Zhang, L.; Zhu, Y. *Electroanalysis* **2001**, *13*, 413.
- (363) Han, N. C.; Lyu, Y. K.; Jee, H. H.; Lee, W. Y. *Electroanalysis* **2007**, *19*, 1524.
- (364) Gaitán, M.; Gonçalves, V. R.; Soler-Illia, G. J. A. A.; Baraldo, L. M.; de Torresi, S. I. C. *Biosens. Bioelectron.* **2010**, *26*, 890.
- (365) Bao, S. J.; Li, C. M.; Zang, J. F.; Cui, X. Q.; Qiao, Y.; Guo, J. *Adv. Funct. Mater.* **2008**, *18*, 591.
- (366) Tang, H.; Yan, F.; Tai, Q.; Chan, H. L. *Biosens. Bioelectron.* **2010**, *25*, 1646.
- (367) Luo, Y.; Liu, H.; Rui, Q.; Tian, Y. *Anal. Chem.* **2009**, *81*, 3035.
- (368) Guo, C.; Hu, F.; Li, C. M.; Shen, P. K. *Biosens. Bioelectron.* **2008**, *24*, 819.
- (369) Zhang, M.; Li, L.; Du, Z.; Xu, S.; Li, C.; Chen, X.; Zhang, T.; Wang, T. *Sens. Lett.* **2009**, *7*, 543.
- (370) Wu, F.; Xu, J.; Tian, Y.; Hu, Z.; Wang, L.; Xian, Y.; Jin, L. *Biosens. Bioelectron.* **2008**, *24*, 198.
- (371) Xie, Q.; Zhao, Y.; Chen, X.; Liu, H.; Evans, D. G.; Yang, W. *Biomaterials* **2011**, *32*, 6588.
- (372) Xie, Y.; Zhou, L.; Huang, H. *Biosens. Bioelectron.* **2007**, *22*, 2812.
- (373) Kafi, A. K. M.; Wu, G.; Chen, A. *Biosens. Bioelectron.* **2008**, *24*, 566.

- (374) Kang, Q.; Yang, L.; Cai, Q. *Bioelectrochemistry* **2008**, *74*, 62.
- (375) Zhao, G.; Lei, Y.; Zhang, Y.; Li, H.; Liu, M. *J. Phys. Chem. C* **2008**, *112*, 14786.
- (376) Benvenuto, P.; Kafi, A. K. M.; Chen, A. J. *Electroanal. Chem.* **2009**, 627, 76.
- (377) Pang, X.; He, D.; Luo, S.; Cai, Q. *Sens. Actuators, B* **2009**, *137*, 134.
- (378) Zhang, Y.; Xiao, P.; Zhou, X.; Liu, D.; Garcia, B. B.; Cao, G. *J. Mater. Chem.* **2009**, *19*, 948.
- (379) Liu, M.; Zhao, G.; Tang, Y.; Yu, Z.; Lei, Y.; Li, M.; Zhang, Y.; Li, D. *Environ. Sci. Technol.* **2010**, *44*, 4241.
- (380) Wei, Y.; Li, Y.; Qu, Y.; Xiao, F.; Shi, G.; Jin, L. *Anal. Chim. Acta* **2009**, *643*, 13.
- (381) Njagi, J.; Ispas, C.; Andreescu, S. *Anal. Chem.* **2008**, *80*, 7266.
- (382) Srivastava, S.; Ali, M. A.; Solanki, P. R.; Chavhan, P. M.; Pandey, M. K.; Mulchandani, A.; Srivastava, A.; Malhotra, B. D. *RSC Adv.* **2013**, *3*, 228.
- (383) Pan, T. M.; Lin, J. C. *Sens. Actuators, B* **2009**, *138*, 474.
- (384) Jang, H. D.; Kim, S. K.; Chang, H.; Roh, K. M.; Choi, J. W.; Huang, J. *Biosens. Bioelectron.* **2012**, *38*, 184.
- (385) Xu, C. X.; Huang, K. J.; Chen, X. M.; Xiong, X. Q. *J. Solid State Electrochem.* **2012**, *16*, 3747.
- (386) Wang, K.; Li, H. N.; Wu, J.; Ju, C.; Yan, J. J.; Liu, Q.; Qiu, B. *Analyst* **2011**, *136*, 3349.
- (387) Zhang, X.; Wang, H.; Yang, C.; Du, D.; Lin, Y. *Biosens. Bioelectron.* **2013**, *41*, 669.
- (388) Ansari, A. A.; Sumana, G.; Pandey, M. K.; Malhotra, B. D. *J. Mater. Res.* **2009**, *24*, 1667.
- (389) Wu, C. T.; Chen, P. Y.; Chen, J. G.; Suryanarayanan, V.; Ho, K. C. *Anal. Chim. Acta* **2009**, *633*, 119.
- (390) Yao, H.; Shum, A. J.; Cowan, M.; Lähdesmäki, I.; Parviz, B. A. *Biosens. Bioelectron.* **2011**, *26*, 3290.
- (391) Sun, W.; Guo, Y.; Ju, X.; Zhang, Y.; Wang, X.; Sun, Z. *Biosens. Bioelectron.* **2013**, *42*, 207.
- (392) Kafi, A. K. M.; Chen, A. *Talanta* **2009**, *79*, 97.
- (393) Kafi, A. K. M.; Wu, G.; Benvenuto, P.; Chen, A. J. *Electroanal. Chem.* **2011**, 662, 64.
- (394) Chen, G.; Wang, J.; Wu, C.; Li, C. Z.; Jiang, H.; Wang, X. *Langmuir* **2012**, *28*, 12393.
- (395) Wang, K.; Wu, J.; Liu, Q.; Jin, Y.; Yan, J.; Cai, J. *Anal. Chim. Acta* **2012**, *745*, 131.
- (396) Tu, W.; Dong, Y.; Lei, J.; Ju, H. *Anal. Chem.* **2010**, *82*, 8711.
- (397) An, Y.; Tang, L.; Jiang, X.; Chen, H.; Yang, M.; Jin, L.; Zhang, S.; Zhang, W. *Chem.—Eur. J.* **2010**, *16*, 14439.
- (398) Zhu, Y.; Cao, H.; Tang, L.; Yang, X.; Li, C. *Electrochim. Acta* **2009**, *54*, 2823.
- (399) Ji, J.; Yang, H.; Liu, Y.; Chen, H.; Kong, J.; Liu, B. *Chem. Commun.* **2009**, 12, 1508.
- (400) Han, X.; Zhu, Y.; Yang, X.; Li, C. *J. Alloys Compd.* **2010**, *500*, 247.
- (401) Wang, Y.; Ma, X.; Wen, Y.; Xing, Y.; Zhang, Z.; Yang, H. *Biosens. Bioelectron.* **2010**, *25*, 2442.
- (402) Han, J.; Zhuo, Y.; Chai, Y. Q.; Mao, L.; Yuan, Y. L.; Yuan, R. *Talanta* **2011**, *85*, 130.
- (403) Cao, S.; Zhang, L.; Chai, Y.; Yuan, R. *Biosens. Bioelectron.* **2013**, *42*, 532.
- (404) Wei, Y.; Li, Y.; Qu, Y.; Xiao, F.; Shi, G.; Jin, L. *Anal. Chim. Acta* **2009**, *643*, 13.
- (405) Kang, Q.; Yang, L.; Chen, Y.; Luo, S.; Wen, L.; Cai, Q.; Yao, S. *Anal. Chem.* **2010**, *82*, 9749.
- (406) Yan, K.; Wang, R.; Zhang, J. *Biosens. Bioelectron.* **2014**, *53*, 301.
- (407) Wang, K.; Wu, J.; Liu, Q.; Jin, Y. C.; Yan, J. J.; Cai, J. R. *Anal. Chim. Acta* **2012**, *745*, 131.
- (408) Zhao, W.; Ma, Z.; Yan, D.; Xu, J.; Chen, H. *Anal. Chem.* **2012**, *84*, 10518.
- (409) Li, Y.; Hsu, P.; Chen, S. *Sens. Actuators, B* **2012**, *174*, 427.
- (410) Wang, G.; Xu, J.; Chen, H. *Biosens. Bioelectron.* **2009**, *24*, 2494.
- (411) Chen, D.; Zhang, H.; Li, X.; Li, J. *Anal. Chem.* **2010**, *82*, 2253.
- (412) Zhu, Y.; Cao, H.; Tang, L.; Yang, X.; Li, C. *Electrochim. Acta* **2009**, *54*, 2823.
- (413) Zhang, Y.; Yang, T.; Zhou, N.; Zhang, W.; Jiao, K. *Sci. China, Ser. B: Chem.* **2008**, *51*, 1066.
- (414) Zeng, X.; Bao, J.; Han, M.; Tu, W.; Dai, Z. *Biosens. Bioelectron.* **2014**, *54*, 331.
- (415) Li, H.; Li, J.; Yang, Z.; Xu, Q.; Hu, X. *Anal. Chem.* **2011**, *83*, 5290.
- (416) Lia, H.; Li, J.; Xu, Q.; Yang, Z.; Hu, X. *Anal. Chim. Acta* **2013**, *766*, 47.
- (417) Lu, W.; Jin, Y.; Wang, G.; Chen, D.; Li, J. *Biosens. Bioelectron.* **2008**, *23*, 1534.
- (418) Lee, H. C.; Lin, J. L.; Chin, Y. L.; Sun, T. P. *Sens. Lett.* **2008**, *6*, 1001.
- (419) Chou, J. C.; Lin, C. Y. *Sens. Lett.* **2008**, *6*, 929.
- (420) Ozasa, K.; Nemoto, S.; Lee, Y.; Mochitate, K.; Hara, M.; Maeda, M. *Appl. Surf. Sci.* **2007**, *254*, 36.
- (421) Ozasa, K.; Nemoto, S.; Li, Y.; Hara, M.; Maeda, M.; Mochitate, K. *Surf. Interface Anal.* **2008**, *40*, 579.
- (422) Li, Y.; Liu, X.; Yuan, H.; Xiao, D. *Biosens. Bioelectron.* **2009**, *24*, 3706.
- (423) Lahav, M.; Kharitonov, A. B.; Katz, O.; Kunitake, T.; Willner, I. *Anal. Chem.* **2001**, *73*, 720.
- (424) Pogorelova, S. P.; Kharitonov, A. B.; Willner, I.; Sukenik, C. N.; Pizem, H.; Bayer, T. *Anal. Chim. Acta* **2004**, *504*, 113.
- (425) Lahav, M.; Kharitonov, A. B.; Willner, I. *Chem.—Eur. J.* **2001**, *7*, 3992.
- (426) Zayats, M.; Lahav, M.; Kharitonov, A. B.; Willner, I. *Tetrahedron* **2002**, *58*, 815.
- (427) Mun, K. S.; Alvarez, S. D.; Choi, W. Y.; Sailor, M. J. *ACS Nano* **2010**, *4*, 2070.
- (428) Ji, J.; Yang, H.; Liu, Y.; Chen, H.; Kong, J.; Liu, B. *Chem. Commun.* **2009**, 12, 1508.
- (429) Yang, L.; Chen, B.; Luo, S.; Li, J.; Liu, R.; Cai, Q. *Environ. Sci. Technol.* **2010**, *44*, 7884.
- (430) Doong, R. A.; Shih, H. M. *Biosens. Bioelectron.* **2010**, *25*, 1439.
- (431) Doong, R. A.; Shih, H. M. *Biosens. Bioelectron.* **2006**, *22*, 185.
- (432) Zhang, W.; Ganesh, N.; Block, I. D.; Cunningham, B. T. *Sens. Actuators, B* **2008**, *131*, 279.
- (433) Wang, J.; Wang, L.; Sun, Y.; Zhu, X.; Cao, Y.; Wang, X.; Zhang, H.; Song, D. *Colloids Surf., B* **2010**, *75*, 520.
- (434) Székács, A.; Trummer, N.; Adányi, N.; Váradi, M.; Szendro, I. *Anal. Chim. Acta* **2003**, *487*, 15.
- (435) Wei, X.; Xiao, C.; Liu, C.; Wang, K.; Tu, Y. *Electroanalysis* **2014**, *26*, 807.
- (436) Tong, X.; Sheng, P.; Yan, Z.; Tran, T. T.; Wang, X.; Cai, J.; Cai, Q. *Sens. Actuators, B* **2014**, *198*, 41.
- (437) Ding, S.; Gao, B.; Shan, D.; Sun, Y.; Cosnier, S. *Biosens. Bioelectron.* **2013**, *39*, 342.
- (438) Wei, X.; Xiao, C.; Wang, K.; Tu, Y. *J. Electroanal. Chem.* **2013**, *702*, 37.
- (439) Yuan, L.; Zhou, L.; Li, J.; Shi, L.; Tran, T. T.; Chen, L.; Huang, C.; Yan, Z.; Cai, Q. *Anal. Methods* **2013**, *5*, 3626.
- (440) Liu, C.; Wei, X.; Tu, Y. *Talanta* **2013**, *111*, 156.
- (441) Li, W.; Ge, S.; Wang, S.; Yan, M.; Ge, L.; Yu, J. *Luminescence* **2013**, *28*, 496.
- (442) Wang, L.; Ma, S.; Wang, X.; Liu, D.; Liu, S.; Han, X. *J. Mater. Chem. B* **2013**, *1*, 5021.
- (443) Song, Y.; Zhuang, Q.; Li, C.; Liu, H.; Cao, J.; Gao, Z. *Electrochem. Commun.* **2012**, *16*, 44.
- (444) Li, J.; Yang, L.; Luo, S.; Chen, B.; Li, J.; Lin, H.; Cai, Q.; Yao, S. *Anal. Chem.* **2010**, *82*, 7357.
- (445) Xu, Z.; Yu, J. *Nanotechnology* **2010**, *21*, 245501.
- (446) Mao, L.; Yuan, R.; Chai, Y.; Zhuo, Y.; Yang, X. *Sens. Actuators, B* **2010**, *149*, 226.
- (447) Li, Y.; Yang, F.; Yang, X. *Analyst* **2009**, *134*, 2100.
- (448) Lin, Z.; Liu, Y.; Chen, G. *Electrochem. Commun.* **2008**, *10*, 1629.
- (449) Song, H.; Zhang, Z.; Wang, F. *Electroanalysis* **2006**, *18*, 1838.

- (450) Sheng, P.; Wu, S.; Bao, L.; Wang, X.; Chen, Z.; Cai, Q. *New J. Chem.* **2012**, 36, 2501.
- (451) Sun, H.; Choy, T. S.; Zhu, D. R.; Yam, W. C.; Fung, Y. S. *Biosens. Bioelectron.* **2009**, 24, 1405.
- (452) He, F.; Liu, S. *Talanta* **2004**, 62, 271.
- (453) Zayats, M.; Lahav, M.; Kharitonov, A. B.; Willner, I. *Tetrahedron* **2002**, 58, 815.
- (454) Yu, Z.-M.; Wei, X.-H.; Yan, J.-L.; Tu, Y.-F. *Analyst* **2012**, 137, 1922.
- (455) Bell, S. E. J.; Sirimuthu, N. M. S. *Chem. Soc. Rev.* **2008**, 37, 1012.
- (456) Park, J.; Bauer, S.; Schiegel, K. A.; Neukan, F. W.; Mark, K. V.; Schmuki, P. *Small* **2009**, 5, 666.
- (457) Zhang, N. G.; Deng, Y. L.; Tai, Q. D.; Cheng, B.; Zhao, L. B.; Shen, Q. L.; He, R. X.; Hong, L. Y.; Liu, W.; Guo, S. S.; Liu, K.; Tseng, H. R.; Xiong, B.; Zhao, X. Z. *Adv. Mater.* **2012**, 24, 2756.